SLAC-PUB-2275
March 1979
(T/E)

A STUDY OF CHARGED PSEUDOSCALAR MESON PHOTOPRODUCTION FROM HYDROGEN AND DEUTERIUM WITH 16 GEV LINEARLY POLARIZED PHOTONS*

D. J. Quinn,[(a)] J. P. Rutherfoord[(b)] and M. A. Shupe[(c)]
Tufts University, Medford, Mass. 02155

and

D. J. Sherden, R. H. Siemann[(d)] and C. K. Sinclair
Stanford Linear Accelerator Center
Stanford University, Stanford, California 94305

Abstract

The asymmetries in forward $\pi - N$, $\pi - \Delta$, and $K^+ - (\Lambda+\Sigma)$ photoproduction have been measured with a 16 GeV linearly polarized beam. The experimental method and the procedures for extracting cross sections and asymmetries from the data are discussed in detail. Information on the energy and momentum transfer dependence of cross sections for natural and unnatural parity exchange, interference between exchanges of opposite G - parity, and Vector Meson Dominance is obtained and discussed.

Submitted to Physical Review D

---

* Work supported by the Department of Energy under contract number EY-76-C-03-0515.

(a) Present address: SRI International, Menlo Park, Calif. 94025.
(b) Present address: University of Washington, Seattle, Wash. 98195.
(c) Present address: University of Illinois, Urbana, Ill. 61801.
(d) Present address: Cornell University, Ithaca, N.Y. 14853.

I. Introduction

The study of pseudoscalar meson photoproduction, although often included as a branch of lepton and photon physics, shares many concepts with purely hadronic interaction studies. Through connections such as Vector Dominance the photon can be thought of as a strongly interacting particle. It is therefore not surprising to find similar theoretical interpretations for photoproduction and strong interaction experiments.

There are, however, important differences which distinguish pseudoscalar meson photoproduction from other strong interaction processes. Since the photon has two possible spin states and does not have a unique isospin, more amplitudes are necessary to describe photoproduction, as opposed to production by pseudoscalar mesons, of any particular final state. This complication is compensated for by several advantages of photoproduction studies. For example, it is possible to study the photoproduction of all members of the pseudoscalar nonet, free of any diffractive channels, with a single beam. Furthermore, many reactions can be measured with a single experimental setup, providing a relatively systematic-free view of a large body of data.

A significant advantage of photoproduction is that with a linearly polarized photon beam one can obtain information on the naturality of t-channel exchanges. The asymmetry in pseudoscalar meson photoproduction with linearly polarized photons is defined as

$$\Sigma(t) \equiv \frac{\frac{d\sigma_\perp}{dt} - \frac{d\sigma_\parallel}{dt}}{\frac{d\sigma_\perp}{dt} + \frac{d\sigma_\parallel}{dt}} \qquad (1)$$

where $d\sigma_\perp/dt$ ($d\sigma_\parallel/dt$) is the cross section for photons polariz perpendicular (parallel) to the production plane defined by the photon and

detected pseudoscalar meson. Using crossing symmetry arguments Stichel[1] showed that to leading order in t/s, $d\sigma_\perp/dt$ ($d\sigma_\parallel/dt$) can receive contributions from only natural (unnatural) parity exchange in the t-channel. Stichel obtained this result for single pion photoproduction from nucleons; other authors[2] have extended this result to the general case of any allowed pseudoscalar meson plus baryon final state.

In 1962 Cabbibo et al.[3] proposed using coherent pair production in crystalline material to polarize high energy photon beams, and in 1970 Berger et al.[4] verified this polarization technique using compression annealed pyrolytic graphite. Based on this work, we constructed a polarized photon beam which allowed significant new measurements of the asymmetry for many pseudoscalar photoproduction reactions. In this paper we present a detailed description of the experiment as well as the final results. These results are for three separate classes of reactions: single pion photoproduction ($\gamma p \to \pi^+ n$ and $\gamma n \to \pi^- p$), $\pi - \Delta$ photoproduction ($\gamma p \to \pi^- \Delta^{++}$, $\gamma p \to \pi^+ \Delta^o$, $\gamma n \to \pi^- \Delta^+$ and $\gamma n \to \pi^+ \Delta^-$), and K^+ photoproduction ($\gamma p \to K^+ \Lambda$, $\gamma p \to K^+ \Sigma$ and $\gamma n \to K^+ \Sigma^-$). Brief summaries of our results, some of which have been published in previous papers,[5,6] and their relationship to previous experiments follow.

(i) Single pion photoproduction. Before this experiment, the asymmetry for single π^+ photoproduction has been measured up to 12 GeV incident energy.[7,8,9,10] These measurements showed that the asymmetry is essentially energy independent, and that this reaction is dominated by natural parity exchange for $|t| > m_\pi^2$. Our results are in agreement with these earlier measurements.

The π^- asymmetry had been measured up to only 3.4 GeV incident energy.[11,12] At that energy there are significant contributions from unnatural parity exchange. Combining these lower energy measurements with our data shows that the unnatural parity exchange cross section is energy dependent; this dependence is consistent with that expected from a simple pion Regge trajectory.

Our data and the lower energy data for both π^+ and π^- photoproduction have several features in common. There is evidence for significant interference between natural parity exchanges of opposite G-parity, and no evidence for such interference between unnatural parity exchanges. The Vector Dominance comparison between our measured asymmetries and the density matrix elements for $\pi^- p \to \rho^o n$ shows poor agreement.

(ii) $\pi - \Delta$ photoproduction. Previous measurements of the asymmetries for these processes are limited,[10,13,14] and our measurements are the first with statistical significance. All four processes are dominated by natural parity exchange at large $|t|$ and unnatural parity exchange at small $|t|$.

Charge ratios for both perpendicular and parallel photons show significant interference between exchanges of opposite G-parity. For perpendicular photons this interference is almost completely destructive at $t \simeq -.15$ GeV^2 leading to a dip in the natural parity exchange cross section for $\gamma p \to \pi^- \Delta^{++}$ and for the sum $\gamma p \to \pi^+ \Delta^o$ plus $\gamma n \to \pi^+ \Delta^-$ (measured from a deuterium target).

A Vector Dominance comparison between our data and data from $\pi^+ p \to \rho^o \Delta^{++}$ shows good agreement for the asymmetries and a similar t-dependence for the cross sections.

(iii) K^+ photoproduction. These are the first measurements of the K^+ polarized photon asymmetry. Because of the small difference between the Λ and Σ masses, the asymmetries for individual processes are difficult to determine. Much greater confidence can be placed in the asymmetry for the sum of processes (e.g., for the sum $\gamma p \to K^+\Lambda$, $\gamma p \to K^+\Sigma^0$ and $\gamma n \to K^+\Sigma^-$ from a deuterium target). This combined asymmetry has been measured from both hydrogen and deuterium targets, and for each target it rises from 0 at t_{min} to 1.0 for $|t| > .05$ GeV^2. Therefore, K^+ photoproduction is dominated by natural parity exchange.

We also present asymmetry results for individual processes, and make some qualitative arguments about the nature of the s-channel helicity amplitudes for K^+ photoproduction.

II. Experimental Details

A plan view of the experimental arrangement is shown in Fig. 1. A 16.05 GeV linearly polarized bremsstrahlung beam was incident on either a liquid hydrogen or liquid deuterium target. Photoproduced mesons were identified and momentum analyzed with the SLAC 20 GeV/c spectrometer. Analysis of the pion or kaon momentum spectra permitted a separation of the various two body reactions contributing to the total yield of these particles.

In the following sections, we describe the components of the experiment in some detail, indicate the sources of various uncertainties and corrections, and describe our data taking procedures.

A. Polarized Photon Beam

A thorough description of the photon beam developed for this experiment has been published.[15] Only a summary of the beam production and its characteristics is presented here.

A 16.05 GeV electron beam from the Stanford Linear Accelerator passed through a beam transport system containing ±0.25% energy defining slits, struck a 0.0285 radiation length aluminum radiator, and was then deflected into a beam dump. The unpolarized bremsstrahlung from the radiator passed through 61 cm of compression annealed pyrolytic graphite, in which it was partially linearly polarized and unavoidably attenuated. The polarization mechanism was the preferential absorption, through coherent pair production, of one linear polarization state from the unpolarized incident bremsstrahlung. The polarization plane was rotated by rotating the graphite about an axis along the beam.

The beam was collimated immediately before and after the polarizing graphite crystals, and at two other locations further downstream, before reaching the experimental target. Sweeping magnets were located after each of the latter two collimators, and the polarizing crystals were located in the field of a third sweeping magnet. With the collimation normally employed, the beam spot size at the target was approximately 2 cm by 2 cm. The photon beam position at the target was controlled by two small steering magnets upstream of the aluminum radiator. The electron beam position at the radiator was monitored by a remotely viewed helium Cerenkov position monitor immediately downstream of the radiator, while the photon beam position at the target could be observed remotely on removeable zinc sulphide screens upstream of the target. These screens

were removed during data taking. The photon beam was dumped into a secondary emission quantameter[16] located beyond the target.

The intensity of the initial bremsstrahlung beam was attenuated by a factor of about twenty in the polarizing crystal. The energy spectrum of the attenuated and polarized beam near the endpoint energy was similar to that of ordinary bremsstrahlung. Thus we chose to relate the number of quanta of energy k to k+dk in the final beam, $Cn(k)dk$, to the number in the initial bremsstrahlung beam, $C_o n_o(k)dk$, by an attenuation function A(k), such that:

$$n(k) = A(k)\, n_o(k) \quad .$$

Both n(k) and $n_o(k)$ are normalized such that:

$$\int_0^{E_o} kn(k)\, dk = \int_0^{E_o} kn_o(k)\, dk = E_o \quad ,$$

where E_o is the bremsstrahlung endpoint energy. C_o and C thus represent the number of equivalent quanta in the initial and final beams. Typical values in the present experiment were $C_o = 4 \times 10^9$ and $C = 2 \times 10^8$ equivalent quanta per SLAC beam pulse.

The incident spectrum $n_o(k)$ was calculated to an accuracy of ±3% near E_o.[17] A(k) was determined by comparing the incident and attenuated bremsstrahlung spectra, which were measured with the SLAC pair spectrometer.[18] The measurements of A(k) in the region near E_o are shown in Fig. 2(a). We have parametrized A(k) as a linear function of k, as expected from the calculated properties of the crystal polarizer. The uncertainty in our one parameter fit to A(k) is estimated to be ±0.8%. In Fig. 2(b) we show n(k).

While uncertainties in A(k) and $n_o(k)$ affect the normalization of measured cross sections they do not influence asymmetry measurements. Asymmetry measurements are affected only by differences in A(k) between the two beam polarizations. We have determined A(k) for both beam polarizations, and the results are consistent with A(k) being polarization independent. We estimate the systematic uncertainty in our quoted asymmetries due to any polarization dependence of A(k) to be less than ±0.025.

The polarization of the beam was measured to be 0.255 ± 0.020 for photon energies between 13.5 and 16 GeV by using a second graphite crystal assembly 30.5 cm long to analyze the polarization produced by the first crystal. The uncertainty in the measured polarization introduces a systematic uncertainty into each asymmetry of ±8% of itself. Measurements of the asymmetry in $\gamma p \to \pi^+ n$ at $t = 0.15$ $(GeV/c)^2$, made several times during the course of the experiment, demonstrated that the beam polarization remained constant to within ±0.008.

B. Beam Flux Measurement

For all data but that obtained at the smallest angle, the secondary emission quantameter (SEQ) served as our primary photon beam monitor. The beam was also monitored by a thin ion chamber and a helium filled Cerenkov monitor,[16] both located upstream of the target. The electron beam incident on the radiator was monitored by a precision toroid.[19] Yields from these various monitors were intercompared at the end of each run to check for beam steering drifts, incorrect collimator settings, etc.

The measurements of A(k) were done at very low beam intensities to obtain reasonable counting rates in the pair spectrometer. A gas filled quantameter[20] was used to monitor the beam for these measurements. This

point is important, since the quantameter responds to the total beam energy as does the SEQ used as the beam monitor for the asymmetry measurements.

The SEQ response was compared to that of a precision silver calorimeter[16] using the Cerenkov monitor as an intermediary. The SEQ response varied by less than 1% with respect to that of the silver calorimeter during the experiment, and was independent of beam polarization to less than 0.3%.

Both the ion chamber and the Cerenkov monitor were found to have polarization dependent responses when compared to the SEQ. For the Cerenkov monitor, this difference is typically less than 0.6% between the two polarizations. As the beam spectrum was found to be polarization independent when monitored with a total absorption device, we attribute the polarization dependence observed in the thin monitors to slight differences in the beam halo, rather than to the SEQ. Both the ion chamber and the Cerenkov monitor are much more sensitive to beam halo than the SEQ.

For the data obtained at the smallest angle, 0.3^{o}, the SEQ could not remain in the beam as it would have blocked the spectrometer aperture. For these data, the Cerenkov monitor was used to measure the beam flux. The polarization dependence of the Cerenkov monitor was removed by performing frequent SEQ - Cerenkov monitor intercomparisons for both polarizations. This procedure introduces an additional ±0.5% uncertainty in both the cross section and asymmetry measurements at this angle.

For data taken at 0.7^{o}, it was necessary to move the SEQ partially out of the beam. This resulted in a different SEQ calibration and an

additional ±0.6% uncertainty in the 0.7^{o} cross sections. We do not believe this procedure introduced additional error into the asymmetry measurements at this angle.

In determining the photon beam flux, a correction was made for pair production in the material in the beam after the last sweeping magnet. There were 0.011 radiation lengths of material in addition to the target; half the target length was used in calculating its contribution to the correction. The uncertainty in this correction adds an uncertainty of ±0.5% to all cross sections and does not affect the uncertainties in the asymmetry measurements.

C. Hydrogen and Deuterium Targets

One meter long condensation type[21] liquid hydrogen and deuterium targets were used. These targets and a third identical dummy cell were arranged in a remotely driven vertical array. The downstream end of the targets was horizontally wider than the upstream end to insure that all detected particles left the target through the 0.10 mm stainless steel end windows.

The target cell lengths were measured warm and a correction for the decrease in length with temperature was calculated. The uncertainty in the target length at liquid hydrogen temperatures was ±0.1%. The target liquid was circulated with pumps to insure there were no gas bubbles in the target. The target temperature was monitored with hydrogen vapor pressure thermometers, and was observed to be constant to $\pm 0.5^{o}K$, corresponding to density fluctuations of ±1%.

D. The SLAC 20 GeV/c Spectrometer

The SLAC 20 GeV/c spectrometer,[22] shown in Fig. 3, was used to detect particles photoproduced in the target. The spectrometer contains four

dipoles, four quadrupoles, and three sextupoles, mounted in a frame which can be remotely rotated about the target center. The detectors are mounted in a mechanically separate concrete shielding hut which moves with the magnet frame.

(i) Spectrometer optics. The first order optical properties of the spectrometer are illustrated in Fig. 4. Information on the measured optical properties is available in the SLAC User's Handbook.[23] All trajectory measurements for the present experiment were made with scintillation counter hodoscopes in the detector hut.

In the horizontal plane, the spectrometer is parallel-to-point focussing, causing particles of the same horizontal production angle to be focussed along a line in the theta focal plane with a dispersion of 1.622 cm/mrad. The position of a particle in this focal plane was measured by the θ hodoscope. A second point on the horizontal plane trajectory was measured by the X hodoscope, located 4.44 m upstream of the θ hodoscope. In addition to determining the horizontal production angle, information from these two hodoscopes was combined to determine the horizontal angle of the ray through the detection system, the target coordinate perpendicular to the beam in the horizontal plane, and the horizontal coordinate of the ray at the end of the last bending magnet. Cuts were made on these quantities to remove spurious events. Typically, about 5% of the triggers were removed by these cuts.

In the vertical, momentum dispersing, plane the spectrometer is point-to-point focussing. An "S" - shaped double bend with a momentum cross-over midway along the spectrometer is used so the central ray leaving the last bending magnet is horizontal. Particles leaving the

target with a given momentum are focussed along a line in the momentum focal plane with a dispersion of 3.259 cm/%. The δ hodoscope measures the position in this plane.

There is an approximate vertical production angle focus 5.5 m upstream of the momentum focus, where the ϕ hodoscope is located. In addition to determining the particle momentum, information from the ϕ and δ hodoscopes was combined to determine the vertical production angle and the vertical angle of the ray through the detection system. Satisfactory separation between pions and kaons in the differential Cerenkov counter required rejection of events with a vertical angle in the counter greater than 16 mrad. Typically, fewer than 1% of the triggers were eliminated by this requirement.

The photon beam spon at the target is imaged onto the momentum focus with a magnification of 1.35. Thus, to improve the momentum resolution, the vertical size of the beam should be kept small. Some of the data presented here were taken with a reduced beam height to aid in separating the reactions $\gamma p \to K^+ \Lambda$ and $\gamma p \to K^+ \Sigma^o$.

(ii) Magnet control and momentum scanning. To set the spectrometer to a given central momentum, the proper current in each magnet was calculated, set, and the measured value checked, by an online XDS 9300 computer. Current measurement was done with both precision shunts and transductors. The current values were calculated under the assumption that the magnets had a specified recent history, a requirement we did not in general satisfly. This led to a slight disagreement between the momentum calibration of the spectrometer and the electron beam transport system. The fitting programs, discussed below, employed one parameter to accommodate this small difference.

The momentum acceptance of the spectrometer was not large enough to cover, with a single setting of the central momentum, the entire missing-mass region we wished to study. Since adding data taken with different central momenta can be a source of systematic error, due to the imperfect knowledge of the spectrometer acceptance, we adopted the technique of momentum scanning, developed by Boyarski[24] to minimize such errors.

In this method, the spectrometer acceptance was divided into bins of constant missing-mass-squared, as discussed in Appendix A. Short runs were taken with the spectrometer central momentum centered in each missing-mass-squared bin, over the entire missing-mass region to be covered. In this way, the cross section at a given missing-mass-squared was measured with each part of the spectrometer acceptance.

The procedure followed during a momentum scan was:

(1) Data were accumulated for unit of beam flux at a particular spectrometer central momentum. Typically, such a "mini-run" lasted one minute, and fifty to sixty mini-runs were necessary to cover the desired range in missing-mass-squared.

(2) Upon completion of a mini-run the detectors and beam monitors were gated off and commands were issued to the magnet power supplies to lower the spectrometer central momentum by the width of one missing-mass-squared bin. While the magnets were being set, beam monitors and scalers were read by the computer. Typically, two seconds were required to set the new momentum value.

(3) The detectors and beam monitors were gated on, and data were accumulated for another mini-run. During the data accumulation, the computer read the shunts and transductors to insure that the momentum had been correctly set.

(iii) Event trigger and particle identification. Figure 5 shows a schematic representation of the particle detection system used in this experiment. For most of the experiment, the event trigger was a triple coincidence between the three trigger counters. For data taken at the smallest angle, a shower counter veto requirement was added to the trigger.

Muons were identified by their penetration of a $\bar{1}4$ collision length iron range telescope, and electrons by their large pulse height in a 17.4 radiation length lead-lucite shower counter. Hadrons were defined as those events which did not penetrate the range telescope and which did not produce a large pulse height in the shower counter. The range requirement introduced a negligible inefficiency for hadrons, while the shower counter pulse height requirement eliminated 5% of the hadrons.

The threshold Cerenkov counter, which served as the sole identifier of pions among the hadrons, was filled with nitrogen of sufficient pressure for pions to produce Cerenkov light at 28 mrad. The efficiency was 98.2% for negative pions and 98.8% for positive pions. This difference was due to stray magnetic field at the phototube. We estimate that fewer than 3% of the particles identified as pions by the threshold counter were kaons or protons.

The differential Cerenkov counter was used to identify kaons. Light produced in this counter was focussed into two annular regions which accepted light between 40 and 60, and 60 and 95 mrad to the central axis, respectively. The inner region was separated into two optically isolated halves, and the outer region into four optically isolated quadrants. Each of these areas was viewed with a separate photomultiplier which was independently pulse height analyzed. The counter was filled with Freon 13 of sufficient pressure to place the light from pions in the outer

ring and that from kaons in the inner region. Protons were below threshold for Cerenkov light production.

Hadrons not identified as pions by the threshold counter were grouped into three classes by the differential counter: kaons, protons, and pions misidentified by the threshold counter. Even though the number of pions in this latter category was small, the larger pion production cross sections and smaller decay losses could make this a serious background in the kaon yields. By placing conservative cuts on the pulse height distributions we have eliminated this problem at the expense of kaon identification efficiency. A negligible fraction of our kaon yields were due to misidentified pions, and our overall kaon detection efficiency was 0.937 ± 0.010.

Two small aperture counters were used to study the rate dependence of the trigger. It is particularly important to understand this rate dependence, as it could affect the asymmetry measurements. Since the aperture counters covered only a small fraction of the full acceptance, their counting rate was correspondingly lower than the trigger counters. By measuring the efficiency of the trigger counters for detecting particles which went through the small counters, the normal deadtime monitors (circuits with fixed deadtimes) were calibrated. The deadtime corrections, made on a mini-run by mini-run basis were typically less than 2%, and were very nearly identical for data taken with the two beam polarizations.

E. The On-Line Computer

An XDS 9300 computer, used on-line, provided a number of monitor, control, and analysis services. For each event, the computer read and logged on magnetic tape the data from the counters described above. It

was possible to read only one event per SLAC beam pulse. A correction for events lost due to this restriction was made by scaling the number of events read by the computer to the number of triggers.

Other tasks performed by the computer included magnet control, polarizer control, monitoring of target temperatures and slit settings, and on-line analysis of the data. Typically, over 80% of all events were analyzed on-line, making cross section and asymmetry results available as data accumulated.

F. Data Taking Procedures

Data were taken in sets of four runs, each run consisting of approximately 55 mini-runs. The beam polarization was fixed during a run, and each four run set had two runs of each polarization. The polarization pattern for these four run sets was either $\parallel-\perp-\perp-\parallel$ or $\perp-\parallel-\parallel-\perp$ to cancel any linear drifts in the experimental equipment. Between runs, the beam steering was checked, and the polarization changed, if required.

Since the cross sections we measure are momentum dependent, an error in the asymmetry is possible if the central momentum of the momentum bins differed between runs of different polarization. Hysteresis in the spectrometer magnets could be the source of such an error, since in setting the central momentum, the current, rather than the field, was set. Schwitters[25] determined that the magnetic field differed by 0.1% when the spectrometer momentum was cycled up versus cycled down over 10% of the central value. A shift of this magnitude, corresponding to about half a missing-mass-squared bin, could cause a significant error in the measured asymmetries.

For most of the experiment, such hysteresis effects were eliminated by running the spectrometer momentum scans in one direction only. However, the serious nature of this problem was not recognized until some data had been accumulated with the momentum scans done in both directions. The errors on these data have been enlarged to include our estimate of these effects.

Most data were obtained under identical beam, beam monitor, and spectrometer conditions. Deviations from standard beam monitor conditions at 0.3^{o} and 0.7^{o} have already been noted. For the 0.3^{o} running, the trigger was modified by adding a shower counter veto, and a lead jaw on the small angle side of the spectrometer, midway through the magnetic system, was moved into the horizontal aperture to reduce the rate from electron pair production.

III. Data Reduction

A. Cross Section Determination

For a given mini-run, the counts in any momentum bin may be due to more than one reaction, and the photons which produced these counts can be from any kinematically accessible portion of the spectrum. The experimentally measured result is the cross section per equivalent quantum differential in the solid angle and momentum acceptance of the bin.

$$\text{COUNTS} = \frac{d^2\sigma}{Q\, d\Omega \frac{dp}{p}} \left(\Delta\Omega \frac{\Delta p}{p}\right) N_A N_{EQ} \varepsilon$$

where Q indicates the cross section is per equivalent quantum, $\Delta\Omega$ and Δp are the solid angle and momentum acceptance of the bin, N_A the number of

target nucleons/$(cm)^2$, N_{EQ} the number of equivalent quanta, and ε the detection efficiency. This efficiency refers to particle type only, and does not include any bin-to-bin efficiency variations because these are included in the acceptance.

It is convenient to relate the above cross section to one differential only in solid angle by:

$$\frac{d\sigma}{d\Omega} = \frac{d^2\sigma}{Q\, d\Omega \frac{dp}{p}} \left[p \frac{dk}{dp} n(K) \right]^{-1} \qquad (2)$$

where dk/dp is the Jacobian relating detected particle momentum and incident photon energy and n(K) is the photon flux (see section II-A) evaluated at $K = E_o - 0.05$ GeV.[26] We use this definition of cross section and the convention of evaluating quantities at K when presenting our results. Our measurements of N_A and N_{EQ} were discussed in Section II, where many of the necessary corrections to the detection efficiency were also covered. Details on various other corrections necessary in determining the cross sections have been discussed in Ref. 22, and are summarized in Table I for each particle type and target combination.

The acceptance of each of the twenty missing-mass-squared bins were determined by obtaining the relative acceptances of these bins and the acceptance of the full aperture. A technique adapted from that of Schwitters[25] was used to determine the relative acceptances. The cross section for a given detected particle momentum, p_o, was measured by each of the twenty bins as a consequence of the momentum scanning. The number of counts when this cross section was measured by bin i is directly proportional to the cross section (which is independent of i), the acceptance of the bin (which is independent of p_o), and the measured

flux factors for the particular mini-run. Assuming for convenience of discussion that these flux factors were equal for all mini-runs, and denoting them as FLUX, one has for the mean number of counts expected

$$\mu(i,p_o) = \frac{d^2\sigma(p_o)}{Q\, d\Omega \frac{dp}{p}} \left(\Delta\Omega \frac{\Delta p}{p}\right)_i \text{FLUX} \quad .$$

The unknowns in the problem are the cross sections and bin acceptances. The likelihood for observing these data is

$$\mathscr{L} = \prod_i \prod_{p_o} \mu(i,p_o)^{c(i,p_o)} \frac{\exp(-\mu(i,p_o))}{c(i,p_o)!}$$

where $c(i,p_o)$ is the number of counts observed. By constraining the total acceptance to be a constant, the maximum likelihood problem can be solved by use of Lagrange Multipliers. The relative acceptances determined in this way for all runs at one spectrometer angle were averaged to give the relative bin acceptance for each angle setting.

The acceptance of the full aperture was determined by a combination of experimental and Monte Carlo techniques. This is necessary because of the physical complexity of the spectrometer. There are a number of apertures throughout the spectrometer magnetic system, some of the magnetic elements differ noticeably from ideal behavior, and the spectrometer frame is not perfectly rigid, allowing the relative positions of the magnets to vary somewhat with spectrometer angle.

Our procedure was to use the hodoscopes to define a small stringent acceptance, unrestricted by any apertures. The acceptance of this stringent region was obtained by calculation, using the measured transport matrix elements of the spectrometer. The full acceptance was then measured

relative to the calculated stringent acceptance by lowering the spectrometer momentum to a value where the particle yield did not depend strongly upon momentum or angle, and comparing the number of counts in the full and stringent acceptances.

The acceptance of the stringent region was calculated by tracing randomly generated rays through the spectrometer elements. The ray tracing program[27] used the best available model of the spectrometer elements, and included all physical apertures. This calculation verified that the stringent acceptance was not limited by any aperture and was independent of the central angle of the spectrometer to within ±2%. The calculation further predicted the ratio of the full to stringent acceptances should be of the form $a + b \sin^2\theta_o$, where θ_o is the central angle of the spectrometer. Our measurements of this ratio are consistent with this behavior.

The value we obtain for the stringent acceptance is 3.6% smaller than that obtained by Boyarski et al.,[28] who followed a similar procedure, and remains an unresolved normalization difference between these experiments. We estimate the overall uncertainty in our determination of the full acceptance to be ±4%.

B. Asymmetry Determination

In an experiment such as ours, in which the detector was fixed and the photon polarization vector was rotated, the azimuthal acceptance of the detector must be included in determining the asymmetry. If β is the angle between the photon polarization vector and the production plane, the cross section is given by

$$\frac{d\sigma}{d\Omega}(\beta) = \frac{d\sigma}{d\Omega}[1 - \Sigma(t)\cos 2\beta]$$

where

$$\frac{d\sigma}{d\Omega} = \frac{1}{2}\left[\frac{d\sigma_{\perp}}{d\Omega} + \frac{d\sigma_{\parallel}}{d\Omega}\right]$$

is the unpolarized photon cross section, and $\Sigma(t)$ is the asymmetry defined in Eq. (1). The situation is illustrated in Fig. 6.

If Φ is the azimuthal angle between the production plane of a particular event and the central production plane (defined by the incident beam direction and the central ray to the spectrometer aperture), then the cross sections measured with parallel and perpendicularly polarized photons are:

$$\left\langle \frac{d\sigma}{d\Omega} \right\rangle_{\parallel} = \frac{d\sigma}{d\Omega}\left[1 - \Sigma(t)\frac{\int A(\Phi)\cos 2\Phi \; d\Phi}{\int A(\Phi)\; d\Phi}\right]$$

$$= \frac{d\sigma}{d\Omega}\left[1 - \Sigma(t)\langle\cos 2\Phi\rangle\right]$$

and

$$\left\langle \frac{d\sigma}{d\Omega} \right\rangle_{\perp} = \frac{d\sigma}{d\Omega}\left[1 + \Sigma(t)\langle\cos 2\Phi\rangle\right]$$

where $A(\Phi)$ is the azimuthal acceptance of the spectrometer. The best measurement of $\langle\cos 2\Phi\rangle$, defined above, is the weighted mean of the values obtained with parallel and perpendicular photons. Denoting these quantities by $\langle\cos 2\Phi\rangle_{\parallel}$ and $\langle\cos 2\Phi\rangle_{\perp}$,

$$\langle\cos 2\Phi\rangle = \frac{\left\langle \frac{d\sigma}{d\Omega} \right\rangle_{\perp}\langle\cos 2\Phi\rangle_{\perp} + \left\langle \frac{d\sigma}{d\Omega} \right\rangle_{\parallel}\langle\cos 2\Phi\rangle_{\parallel}}{\left\langle \frac{d\sigma}{d\Omega} \right\rangle_{\perp} + \left\langle \frac{d\sigma}{d\Omega} \right\rangle_{\parallel}}$$

and, therefore,

$$\Sigma(t) = \frac{\langle \frac{d\sigma}{d\Omega} \rangle_{\perp} - \langle \frac{d\sigma}{d\Omega} \rangle_{\parallel}}{\langle \frac{d\sigma}{d\Omega} \rangle_{\perp} \langle \cos 2\Phi \rangle_{\perp} + \langle \frac{d\sigma}{d\Omega} \rangle_{\parallel} \langle \cos 2\Phi \rangle_{\parallel}} \quad . \qquad (3)$$

Equation (3) gives the asymmetry in terms of the measured cross sections and values for $\langle \cos 2\Phi \rangle$. The unpolarized cross section in terms of the measured cross section is

$$\frac{d\sigma}{d\Omega} = \frac{1}{2} \left[\langle \frac{d\sigma}{d\Omega} \rangle_{\perp} + \langle \frac{d\sigma}{d\Omega} \rangle_{\parallel} \right] \quad . \qquad (4)$$

Knowledge of the vertical and horizontal production angles from the hodoscopes was used to determine the azimuthal angle for each event, and from these measurements, $\langle \cos 2\Phi \rangle$ was determined. Typical values for $\langle \cos 2\Phi \rangle$ ranged from 0.67 at a spectrometer angle of 0.7° to 0.99 at a spectrometer angle of 4.5°. The error in $\langle \cos 2\Phi \rangle$ was a negligible contribution to the error in the asymmetry.

C. 0.3 Degree Analysis

At the 0.3° point, the full spectrometer acceptance extended very nearly to 0° in the polar angle and included a very large region in azimuthal angle. Since both the cross section and asymmetry for photo-produced pions varies dramatically over this region, it was necessary to subdivide the acceptance to extract meaningful results. To this end, the full acceptance was separated into three polar angle (θ_s) and nine azimuthal angle (ϕ_s) regions. The 0.3° acceptance, as subdivided, is shown in Fig. 7. Data from the nine azimuthal angle regions were added symmetrically about the horizontal midplane of the spectrometer to form five 15° wide azimuthal bins. The kaon data from the three polar angle

bins was averaged, since the kaon yields do not vary strongly over the acceptance at this point.

In principle, the relative acceptances of the twenty missing-mass-squared bins may differ in each (θ_s,ϕ_s) bin. However, the data available for determining these relative acceptances could not be divided this finely and still give reasonable error bars. Therefore, in the analysis of the 0.3^o data, we have assumed that all relative acceptances were equal. The data were consistent with this assumption. Given equal incident beam fluxes for each mini-run, the effect of differing relative acceptances is apparent only near the ends of a momentum scan, where all missing-mass-squared bins do not contribute to the data. The quoted uncertainty on the 0.3^o results includes a contribution to the error to account for possible differences in the relative acceptances.

For each (θ_s,ϕ_s) bin, an experimental asymmetry was obtained as a function of missing-mass-squared. These asymmetries were divided by $\langle\cos 2\Phi\rangle$ for the particular bin, and a weighted average for the five experimental asymmetries thus obtained at each polar angle was used for the final fitting. An unpolarized cross section was obtained by summing the counts in the five azimuthal angle bins and averaging over the incident beam polarization. Given the cross section and asymmetry as a function of missing-mass-squared for each of the three polar angle bins, fits for the cross section and asymmetry for specific processes were made as for the rest of the data.

These procedures for the small angle data had the advantages that knowledge of the acceptance of the individual azimuthal angle bins was not necessary, and that the relative acceptance of the three polar angle bins does not enter into the final asymmetries. We report values for the

pion asymmetry at three angles, and an average kaon asymmetry from our analysis of the 0.3^{o} data.

IV. Analysis of the Momentum Distributions

For each combination of target, spectrometer angle, and spectrometer polarity, the cross section and $\langle \cos 2\Phi \rangle$ were measured as a function of momentum. These measurements were made for both photon polarizations and for pions and kaons. The asymmetries and unpolarized cross sections were then obtained from relations (3) and (4). Typical results for pions are shown in Fig. 8 along with fits to these data.

The dependence of the particle yields on the spectrometer momentum is predominantly a consequence of the beam energy spectrum and two-body kinematics. If the beam were monochromatic and the detected particle was recoiling against a fixed missing-mass, the yield would have a sharp spike at a momentum given by two-body kinematics. For a fixed momentum transfer, this momentum depends on the particle masses and the beam energy. On the other hand, a continuous beam spectrum produces a continuous detected particle momentum spectrum. A rapid variation in the beam spectrum has some of the features of the monochromatic beam. For example, the "step" which occurs at the end point of the attenuated bremsstrahlung spectrum (see Fig. 2(b)) produces similar steps in the particle yield for each possible two-body process. The step in the pion yield from the process $\gamma p \rightarrow \pi^{+} n$ is clearly visible in Fig. 8. The rate of rise of a particular step is determined by

(i) the rate of rise of the photon beam at the endpoint,

(ii) the spectrometer resolution,

(iii) the natural width of the recoil mass, and

(iv) Fermi motion of the target nucleons in the case of a deterium target.

Processes without a fixed recoiling missing-mass also contribute to the yield. These contributions, however, do not reflect the step in the beam spectrum, but rather rise smoothly from their kinematic thresholds as the available phase space increases.

The asymmetry measured at any particular momentum is that of the total yield, and thus contains contributions from all allowed processes. At a given momentum, the contribution of a process to the asymmetry depends on its contribution to the yield. Therefore, to determine the asymmetry of any process, it was necessary to simultaneously fit the average cross section and asymmetry distributions. The free parameters for these fits were the asymmetry and unpolarized cross sections for each process, the experimental resolution and an overall energy shift (see Section II.D.ii).

A. Fitting the Pion Data

A χ^2 minimization program[29] was used to simultaneously determine the cross sections and asymmetries for $\pi - N$, $\pi - \Delta$, $\pi - N(1520)$ and elastic ρ production. The $\pi - N(1520)$ process was included only where allowed by isospin conservation. Details of the parametrizations used for the photon beam spectrum, the nucleon resonance shapes, the shape of the steps in the case of a sharp recoil mass, and the rho production background are given in Appendix B.

Pions of the highest momentum arise from the reaction $\gamma N \rightarrow \pi N$. The spectrometer resolution and the sharpness of the step at the endpoint of the beam spectrum are such that the yield from this process is nearly at its full value before any other process contributes significantly. Thus,

results for this reaction are relatively easily extracted. The only difficulty occurs in the case of large momentum transfer and a deuterium target, where the Fermi motion effectively broadens the momentum resolution. The errors shown include the uncertainties introduced by this effect.

Pions from the decay of diffractively photoproduced ρ's and from non-resonant double pion production can contribute to the yield in the region where we extract our $\pi - \Delta$ results. Pions from ρ decay are not a serious background, however, because at the photon energies of this experiment the ρ and Δ bands in the Dalitz plot do not overlap, as shown in Fig. 9. Only ρ's with a mass much greater than the central ρ mass can contribute pions in our region of interest. As noted in Appendix B, we have included a parametrized ρ decay background in our fits to the pion yield.

The contribution from non-resonant double pion production is small, and consequently poorly determined by our measurements. The uncertainties on the cross section and asymmetry for this process, as determined by the fitting procedure, are much larger than one would estimate from the data of other experiments. Including such a background in our fits thus increases the uncertainties on the $\pi - \Delta$ results unreasonably. We have therefore not included any non-resonant double pion production in our fits, but rather have made a liberal estimate of the possible contribution of this process to our pion yields, assigned a 100% error and an asymmetry of 0.0 ± 0.6 to this estimate, and included these effects in our overall error bar. The small size of the estimated effects, discussed below, make this a reasonable procedure.

We have used the SBT bubble chamber results[30] for the total $\gamma p \to \pi^+\pi^- p$ cross section, subtracted their $\gamma p \to \pi\Delta$ and "parametrization" $\gamma p \to \rho p$ total cross sections, and taken the remainder as the non-resonant double pion total cross section. These results, shown in Fig. 10, are reasonably represented as $\sigma_{\text{non-resonant}} = 24k^{-1.4}\mu b$ with k in GeV, and we use this expression to estimate the total cross section at 16 GeV. Similar data for the other double pion channels are not available; we estimate these cross sections to be equal to the $\gamma p \to \pi^+\pi^- p$ cross section.

At 16 GeV, we estimate the non-resonant cross section for $\gamma p \to \pi^+\pi^- p$ as approximately four times that for $\gamma p \to \pi^-\Delta^{++}$. However, these cross sections have very different distributions in the available phase space. We have used two different distributions for the non-resonant process to estimate the contribution to our yields. The first is the assumption that the non-resonant events are distributed in mass and four-momentum transfer uniformly in phase space. This assumption leads to larger backgrounds at large $|t|$. The second was the measured distributions in x (the Feynman scaling variable) and transverse momentum.[31] This procedure leads to larger backgrounds at small $|t|$. In Fig. 11, the ratio of the non-resonant double pion contribution to our $\pi - \Delta$ cross section is plotted. In calculating the contribution of this non-resonant production to the error in the $\pi - \Delta$ cross sections and asymmetries, we have used the larger of the two estimates.

The magnitude we find for the ratio of non-resonant two pion production to $\pi - \Delta$ production is consistent with what one would expect from the Drell model.[32] In this model, the cross section for $\gamma N \to \pi\Delta$ is proportional to the $\pi - N$ total cross section at the energy of the exchanged pion. In

the region of the Δ, the $\pi - N$ total cross section is dominated by the Δ, and the non-resonant cross section is much smaller than the Δ cross section.

An alternative way to view photoproduction for the purpose of considering backgrounds is related to the ρ exchange diagram of Fig. 12(a). Neglecting off-mass-shell effects and the contribution of longitudinal ρ's, equating charged ρ and neutral ρ exchange, and using Vector Dominance, one has a cross section for ρ exchange which is proportional to the total photoproduction cross section (at an energy equal to the energy of the exchanged ρ). The tenuous nature of the theoretical argument negates the value of a detailed calculation, but the argument does suggest that the missing mass distribution in high energy photoproduction may be related to the total photoproduction cross section at low energies.

These cross sections are presented in Fig. 12(b);[33] one sees that the π^+ cross section has a structure other than the Δ at low energy. Both the energy dependence and the angular distribution indicate that this structure is a non-resonant S-wave contribution to the cross section.[34] Such a structure in our measured missing mass distributions would affect some of our results.

We have studied the shape and other features of our measured momentum distributions, but our resolution in missing-mass is inadequate to give a conclusive answer concerning the existence of any such background. The tests we performed indicate that enhancements at low missing-mass are not present, however, and thus in our analysis we have assumed the effect is absent. The measurements of cross sections and small magnitude asymmetries for $\gamma p \to \pi^+ \Delta^o$ and $\gamma n \to \pi^- \Delta^+$ are most sensitive to this assumption.

B. Fitting the Kaon Data

Just as the pion data can be characterized by $\pi - N$, $\pi - \Delta$, and multi-pion production, the kaon data is described by $K - \Lambda$, $K - \Sigma$, and a background without a fixed recoiling missing-mass. This background rises smoothly from the $K - \pi^o - \Lambda$ threshold. A K^+ yield curve, together with the π^+ yield measured at the same time, is shown in Fig. 13. The cross section above the $K - \Lambda$ threshold is negligible indicating that pions are not a serious background to the kaon data.

The $K - \Lambda$ and $K - \Sigma$ reactions are not observed as separate steps; the resolution smears these steps together. Comparison of the rates of rise of the π^+ step and the K^+ step clearly indicates the presence of more than one contribution to the K^+ step. Since the pion and kaon yields were measured at the same time, the contributions of beam-steering, beam size, and magnet hysteresis to the momentum resolution and offset were the same for both sets of data. Without the information about the resolution and offset from the pion data, it would be impossible to separate the $K - \Lambda$ and $K - \Sigma$ reactions. In fitting the kaon data, the pion data were used to determine these two quantities. Even with this additional information, the separation of $K - \Lambda$ from $K - \Sigma$ cross sections is tenuous, and the resultant separation has large correlated errors, since the sum of the two cross sections is well determined. The errors in the individual asymmetries are further magnified by the small beam polarization. We have carefully checked our procedures for handling the correlated errors, and have included the effects of uncertainties in the momentum resolution and offset in our results for the separated reactions.

The sum of the $K - \Lambda$ plus $K - \Sigma$ cross sections is not affected by the percentage of the step attributed to the individual reactions. The most

significant uncertainty in the determination of the cross section and asymmetry of this sum is the character of the lower momentum background. Fortunately, no backgrounds are kinematically possible over most of the region where the step rises; the sum of the two cross sections is rather well determined and is not sensitive to the background parametrization chosen.

V. Results and Discussion

A. Single Pion Photoproduction

Our results for single pion photoproduction from hydrogen and deuterium targets are presented in Tables II, III, and IV. Some of these results have been published previously.[5]

The ratio of our measured cross sections for $\gamma p \to \pi^+ n$ to those of Boyarski et al.[35] is 1.19 ± 0.03. This ratio shows no t dependence within the quoted error. Known t-independent differences in the analysis of the two experiments account for 0.08 of this ratio, leaving an unaccounted normalization difference of 1.11 ± 0.03. We estimate our overall normalization uncertainty to be 0.07, while that of Boyarski et al.[35] was given as 0.06. In Fig. 14, we compare our measurements for the ratio R between the cross sections for $\gamma D \to \pi^- p p_s$ and $\gamma D \to \pi^+ n n_s$ with those of Boyarski et al.[36] (p_s and n_s denote a spectator proton and neutron respectively). The agreement between the two experiments is excellent over the entire t range. We conclude that any differences between our results and earlier experiments are t independent. We furthermore believe that the small normalization differences between these measurements do not affect our asymmetry measurements in any significant way.

Figure 15(a) shows the ratio of our single π^+ photoproduction cross sections from hydrogen and deuterium. Since single positive pions can be photoproduced only from the proton of the deuterium nucleus, the value of this ratio tests the adequacy of approximating the deuterium cross sections as the sum of free proton and free neutron cross sections. As expected, this ratio falls below unity at small momentum transfers, due to the exclusion principle, and is consistent with one at higher momentum transfers. This comparison indicates that there are no significant systematic errors in isolating single pion production from deuterium, and that any Glauber scattering or Fermi motion effects are small.

Figure 15(b) compares our measurements of the asymmetries in $\gamma p \to \pi^+ n$ and $\gamma D \to \pi^+ n n_s$. The good agreement obtained indicates we can interpret the asymmetry in $\gamma D \to \pi^- p p_s$ as that from the reaction $\gamma n \to \pi^- p$. Calculations by Julius[37] show that any difficulties with such an interpretation should be small compared with the accuracy of our measurements. These calculations are only weakly dependent upon the photoproduction amplitudes used. Julius has used the amplitudes of Kellet[38] which do not describe our results particularly well.

The asymmetry for $\gamma p \to \pi^+ n$, presented with other data in Fig. 16, is seen to have little or no energy dependence over the range of incident photon energies from 3 to 16 GeV. However, the asymmetry in $\gamma D \to \pi^- p p_s$, shown in Fig. 17, shows significant energy dependence.

By parametrizing the differential cross sections for perpendicular and parallel polarized photons in a Regge form:

$$\frac{d\sigma_{\perp,\parallel}}{dt} = f(t)\, s^{2\alpha_{\perp,\parallel}(t) - 2}$$

we can calculate the effective Regge trajectories for natural and unnatural parity exchanges, respectively. These are given by

$$\alpha^{+}_{\perp,\parallel}(t) = \alpha^{+}_{o}(t) + \frac{\ln\left[\dfrac{1 \pm \Sigma^{+}(s_2,t)}{1 \pm \Sigma^{+}(s_1,t)}\right]}{2 \ln\left(\dfrac{s_2}{s_1}\right)} ,$$

$$\alpha^{-}_{\perp,\parallel}(t) = \alpha^{+}_{o}(t) + \frac{\ln\left[\dfrac{R(s_2,t)}{R(s_1,t)}\right] + \ln\left[\dfrac{1 \pm \Sigma^{-}(s_2,t)}{1 \pm \Sigma^{-}(s_1,t)}\right]}{2 \ln\left(\dfrac{s_2}{s_1}\right)} , \qquad (5)$$

and

$$\alpha^{I}_{\perp,\parallel}(t) = \alpha^{+}_{o}(t) + \frac{\ln\left[\dfrac{1 \pm \Sigma^{+}(s_2,t) + R(s_2,t)(1 \pm \Sigma^{-}(s_2,t))}{1 \pm \Sigma^{+}(s_1,t) + R(s_1,t)(1 \pm \Sigma^{-}(s_1,t))}\right]}{2 \ln\left(\dfrac{s_2}{s_1}\right)}$$

where the superscripts +, -, and I refer to the reactions $\gamma p \to \pi^{+} n$, $\gamma n \to \pi^{-} p$, and their sum, which is the isovector photon cross section; the subscripts $\perp$, $\parallel$, and o refer to perpendicular, parallel, and unpolarized photons, the + (-) sign in the $1 \pm \Sigma$ terms is used with perpendicular (parallel) photons, R is the ratio of the differential cross sections for π^{-} to π^{+} photoproduction from deuterium, and s_1 and s_2 refer to the two different CM energies used. For these calculations, we have used our data at 16 GeV, the R measurements of Bar-Yam et al.[39]

at 3 GeV and Heide et al.[40] at 3.4 GeV, and the asymmetry measurements of Bar Yam et al.[11] at 3 GeV. The low energy data was linearly interpolated in t where necessary.

Uncertainties in the beam polarization were included in these calculations. Ordinary error propagation was used in the calculations for perpendicular photons. For the case of parallel photons, where $1 - \Sigma$ may be within an error bar of zero, a Monte Carlo technique was necessary. A value for each of the measured quantities on the right hand side of relations (5) was randomly generated. The distribution of each of the generated quantities was Gaussian, with a mean and standard deviation given by the measurements. The effective trajectory was calculated for each resulting set of values for the quantities. The procedure was repeated 20,000 times. The median of the resulting values for the effective trajectory is given in Fig. 18. The error bars indicate the range containing 68.3% of the values.

The effective trajectory of photoproduction of single pions with perpendicular photons is close to zero, as is the case with unpolarized photons. With parallel photons, the effective trajectory is consistent with that expected of a conventional pion Regge trajectory of either unit slope, or a slope determined by the pion and A_3[41] masses. Both π and B exchange can contribute to π^- photoproduction with parallel photons. The effect of any energy dependence of $\pi - B$ interference can be eliminated by calculating the effective trajectory for the sum of π^+ and π^- production. The result, labelled isovector photons in Fig. 18, is similar, consistent with weak $\pi - B$ exchange degeneracy.

In general, Regge cuts introduced to explain the non-zero forward cross section for single pion photoproduction would be expected to dominate the energy dependence of the cross section for parallel photons, giving results similar to those with perpendicular photons. This does not appear to be the case. Photoproduction models involving pion conspiracy can explain both the non-zero forward cross section, and the energy dependence of the parallel photon cross section.

Lower energy data have shown that the decrease in R for $|t| \geq 0.1$ $(GeV/c)^2$ is associated with perpendicularly polarized photons.[39,40] Interference between t-channel exchanges of natural parity and opposite G-parity produce this effect. Our data, shown in Fig. 19, indicate that this is the case at 16 GeV also. We see no statistically significant evidence for interference between unnatural parity exchanges of opposite G-parity.

The ratio $R_\perp$ for perpendicular photons has significant energy dependence over the entire t range for which it has been measured. At small $|t|$, this dependence is clear even in the unpolarized photon data (Fig. 19), while at large $|t|$ the energy dependence of $R_\perp$ is a reflection of that of the π^- asymmetry.

As the reactions $\gamma p \to \pi^+ n$ and $\gamma n \to \pi^- p$ are related by line reversal, their cross sections are expected to become equal asymptotically.[42] Deviation of R from unity is thus an indication that the photoproduction amplitudes have not reached asymptotic behavior. At large $|t|$, R is at least moving toward unity with increasing energy, while at small $|t|$, this ratio is decreasing with increasing energy. It is clear that the natural parity photoproduction amplitudes in the forward direction are very far from asymptotic behavior at the energy of the present measure-

ments. There is no statistically significant evidence that $R_{\|}$ is different than one at both 3.4 and 16 GeV, and thus one cannot conclude that the photoproduction amplitudes with parallel photons are not asymptotic.

B. $\pi - \Delta(1236)$ Photoproduction

Our cross section and asymmetry results for the reactions $\gamma p \to \pi^- \Delta^{++}$, $\gamma p \to \pi^+ \Delta^o$, $\gamma D \to \pi^- \Delta N_S$, and $\gamma D \to \pi^+ \Delta N_S$, where N_S indicates a spectator nucleon, are given in Tables V and VI. The deuterium reactions represent the sums of the reactions $\gamma D \to \pi^- \Delta^{++} n_s$ plus $\gamma D \to \pi^- \Delta^+ p_s$, and $\gamma D \to \pi^+ \Delta^o n_s$ plus $\gamma D \to \pi^+ \Delta^- p_s$ respectively.

The ratio between our measured cross sections and those of Boyarski et al.[43] is $1.28 \pm .07$, independent of both reaction and momentum transfer within the stated error. Based on the ratio of measured cross sections for $\gamma p \to \pi^+ n$ and different procedures for normalizing the Breit-Wigner for the Δ (see Appendix B), we expect a ratio of $1.34 \pm .04$. As before, we do not believe that small normalization uncertainties influence our asymmetry results in a meaningful way.

The asymmetry results, plotted in Fig. 20, show that all four reactions are dominated by unnatural parity exchange at small $|t|$ and natural parity exchange at large $|t|$. In Fig. 21 we have combined our cross section and asymmetry measurements to obtain the cross sections for perpendicular and parallel photons.

The unnatural parity exchange cross sections of all four reactions vary approximately as $e^{11.5t}$ for $m_\pi^2 \leq -t \leq .2$ GeV^2. Since unnatural parity exchange is dominant in this t region, the unpolarized photon cross section displays similar t dependence. At large $|t|$ the unnatural

parity exchange cross sections fall as e^{6t} to e^{8t} depending on the particular reaction.

The natural parity exchange cross sections have considerable reaction dependent structure in the small $|t|$ region. Both $\gamma p \to \pi^- \Delta^{++}$ and $\gamma D \to \pi^- \Delta N_S$ have large dips in the cross section for perpendicular photons at $t \simeq -0.15$ GeV/c^2. The presence of a dip at this t value is suggestive of a cross section dominated by net s-channel helicity flip = 0. However, when the polarized photon asymmetry is different from zero, as is the case, there must be more than one s-channel amplitude present. This can be seen by writing the polarized photon asymmetry in terms of the s-channel amplitudes

$$\Sigma = \frac{2\,\mathrm{Re}\,(H_1 H_6^* + H_2 H_7^* + H_3 H_4^* + H_5 H_8^*)}{\sum_{i=1}^{8} |H_i|^2}$$

where H_1 and H_2 are the helicity flip zero amplitudes, H_3, H_4 and H_5 are the helicity flip one amplitudes, H_6 and H_7 are the helicity flip two amplitudes, and H_8 is the helicity flip three amplitude. The asymmetry arises from an interference between different s-channel amplitudes.

Therefore, the cross section for perpendicularly polarized photons

$$\frac{d\sigma_\perp}{dt} \propto \sum_{i=1}^{8} |H_i|^2 + 2\mathrm{Re}(H_1 H_6^* + H_2 H_7^* + H_3 H_4^* + H_5 H_8^*) \quad ,$$

can be dominated by a single s-channel amplitude only through a fortuitous cancellation of many terms. A similar dip at about the same t value has been seen in the closely related reaction $\pi^+ p \to \Delta^{++} \rho^o$.[44] This paper shows that a rapid decrease in the absorption corrected One Pion Exchange

combined with an increase in the A_2 exchange contribution can explain this observation.

The cross sections for $\pi\Delta$ production in terms of amplitudes with fixed t-channel quantum numbers are:[43]

$$\frac{d\sigma}{dt}\begin{pmatrix}\gamma p \to \pi^- \Delta^{++} \\ \gamma n \to \pi^+ \Delta^-\end{pmatrix} = 3\sum_{i=1}^{8}\left|A^i_{1-} \mp A^i_{1+} - \frac{1}{3}A^i_{2-}\right|^2 - \tag{6}$$

and

$$\frac{d\sigma}{dt}\begin{pmatrix}\gamma n \to \pi^- \Delta^{+} \\ \gamma p \to \pi^+ \Delta^{o}\end{pmatrix} = \sum_{i=1}^{8}\left|A^i_{1-} \mp A^i_{1+} + A^i_{2-}\right|^2$$

where the summation is over the eight helicity amplitudes, the subscripts 1 and 2 refer to the t-channel isotopic spin, and the + and - subscripts denote the G-parity of the t-channel. Positive G-parity exchanges correspond to isoscalar photons and negative G-parity to isovector photons. In the approximation that any I = 2 amplitudes are small, the ratio of $\pi^-\Delta$ to $\pi^+\Delta$ production from deuterium depends on the interference of I = 1 exchanges of different G-parity:

$$R = \frac{\frac{d\sigma}{dt}(\gamma D \to \pi^- \Delta N_S)}{\frac{d\sigma}{dt}(\gamma D \to \pi^+ \Delta N_S)} \simeq \frac{\sum_{i=1}^{8}\left|A^i_{1-} - A^i_{1+}\right|^2}{\sum_{i=1}^{8}\left|A^i_{1-} + A^i_{1+}\right|^2} .$$

In Fig. 22(a) we compare our measurement of R for unpolarized photons with that of Boyarski et al.[43] The agreement is excellent. In Fig. 22(b) we present our measurements for polarized photons. For parallel photons R is slightly greater than one for $\sqrt{-t} < .4$ GeV^2 and falls below one at larger $|t|$. This is an indication of interference between unnatural parity exchanges of opposite G-parity.

The ratio R for perpendicular photons shows that there is significant interference between natural parity exchanges of opposite G-parity over the entire t region of this experiment. This interference is comparable to that seen in single pion photoproduction (see Fig. 19) except around $t = -0.15\ GeV^2$.

Mesons with two units of isospin are exotic, and no such particle has been discovered. However, there is evidence of $I = 2$ t-channel exchanges. Boyarski et al.[43] measured the ratios of cross sections for $\pi^-\Delta$ and $\pi^+\Delta$ from deuterium and hydrogen. These ratios should be 4/3 and 4 respectively in the absence of $I = 2$ exchanges (see Eqs. 6). Our results are compared with theirs in Fig. 23; we agree with their measurements. The π^- data are consistent with the predicted ratio, and the π^+ data are clearly inconsistent.

In Fig. 24 we present these cross section ratios for perpendicular and parallel photons. Both ratios for $\pi^+\Delta$ production disagree with the expected value of 4. The average ratios are 2.94 ± 0.21 and 2.97 ± 0.34 for perpendicular and parallel photons respectively. The $I = 2$ exchange does not have a definite parity; this makes Regge cuts the probable explanation.

As discussed in Section IV.A, we assume that the Δ is the only contribution to the momentum distribution which is rapidly varying near the Δ threshold. If the ρ exchange model discussed in that section were correct, this would not be the case. In particular, the cross section for $\gamma p \to \pi^+\Delta^0$ would be most strongly affected thereby raising the π^+ deuterium-to-hydrogen ratio closer to the value expected in the absence of $I = 2$ exchanges. Data with better missing-mass resolution

are required to rule out backgrounds of this type, and therefore, one must be cautious about conclusions related to I = 2 exchanges.

Several theoretical models have been developed for $\pi - \Delta$ photoproduction using these polarization data. Goldstein and Owens[45] use Regge poles, absorption corrections and Regge-Regge cuts. Clark[46] uses a phenomenological extension of amplitudes which are constrained by gauge invariance at low $|t|$.

C. Photoproduction at Small $|t|$

The extreme small-angle region in single pion photoproduction has played a crucial role in the development of theories for this process at high energies. The first measurements[35,40] discovered that the cross section rises by a factor of two in the region between $t \approx -m_\pi^2$ and $t = t_{min}$, in contrast to the expected dip. The experimenters[35] noted that the cross section in this region agreed approximately in magnitude as well as in t- and s-dependence with the results of the gauge-invariant electric Born approximation.

In 1964, Stichel and Scholz[47] calculated the minimal gauge invariant contribution of one pion exchange to $\gamma N \to \pi^{\pm}\Delta$. Their calculation is in good agreement with the cross section data[43,48] for $|t| \leq m_\pi^2$. Campbell, Clark, and Horn,[49] applying "low t theorems" to $\gamma N \to \pi^{\pm}\Delta$, as well as to $\gamma N \to \pi^{\pm}N$, set limits on the t-dependence of the cross sections based on constraints that must be satisfied at the pion pole, $t = +m_\pi^2$. Given the zero degree cross section, they were able to determine the t-dependence of both the cross section and asymmetry for $\gamma N \to \pi\Delta$ and $|t| \leq m_\pi^2$. Their result is similar to that obtained by Stichel and Scholz.

Polarized photon asymmetries for these processes can be simply related to differential cross sections in the small t region through an argument given by Harari.[50] Based on angular momentum considerations, at zero degrees $d\sigma_\perp/dt$ must equal $d\sigma_\parallel/dt$; hence either Σ or $d\sigma/dt$ must go to zero as $\theta \to 0^o$. Since only pion exchange is expected to produce a strong variation in the cross section in the region $|t| \leq m_\pi^2$, this variation should appear in $d\sigma_\parallel/dt$, with $d\sigma_\perp/dt$ being relatively featureless. Thus, the reaction $\gamma p \to \pi^+ n$, with a factor of two spike in the cross section near 0^o, should have a polarized photon asymmetry near +1 at $t \sim -m_\pi^2$, while $\gamma p \to \pi^- \Delta^{++}$, which dips at 0^o to about half of the value it has at $t \sim -m_\pi^2$, should have an asymmetry near -0.5 at $t \sim -m_\pi^2$. Measurements of the polarized photon asymmetry at small $|t|$ test the simple ideas behind Harari's argument; they do not test specific models.

In Fig. 25 we plot the $\gamma p \to \pi^+ n$ and $\gamma p \to \pi^- \Delta^{++}$ cross sections for perpendicular and parallel photons at small $|t|$. The $\gamma p \to \pi^+ n$ data clearly show that the rapid variation of the cross section at small $|t|$ is due to unnatural parity exchange in agreement with Harari's argument. The $\gamma p \to \pi^- \Delta^{++}$ data are consistent with expectations, but the natural parity exchange cross section does show significant variation for $|t| < m_\pi^2$. This variation is apparently associated with the dip in the cross section at $t = -0.15$ GeV^2. The $\gamma p \to \pi^+ \Delta^o$ data have larger error bars and are not plotted.

In Figs. 16 and 17 we compare our asymmetry results for single pion production with the electric Born approximation. The agreement is good for $|t| \lesssim m_\pi^2$ in the π^+ case. The asymmetries for $\pi\Delta$ photoproduction at low $|t|$ from the minimal gauge-invariant calculation of Campbell, Clark and Horn[49]

are plotted in Fig. 20. Our measurements are in qualitative agreement, but it should be noted that the model has a constant $d\sigma_\perp/dt$, which is not in agreement with the data.

D. Vector Meson Dominance

Many photo- and electroproduction processes have been discussed within the framework of Vector Meson Dominance. More recently these ideas have been extended to give a picture of the hadronic nature of the photon.[51] This hadronic nature plays a significant role in photon interactions, and in many ways the qualitative features of this picture are more satisfactory than the detailed predictions of the conventional Vector Dominance Model.

One such straightforward detailed prediction is the comparison of the cross section and density matrix elements for $\pi^- p \to \rho^o n$ with the cross section and asymmetry for single pion photoproduction. For purposes of comparison, the photoproduction cross section used is

$$\frac{1}{2}\left(\frac{d\sigma}{dt}(\gamma p \to \pi^+ n) + \frac{d\sigma}{dt}(\gamma n \to \pi^- p)\right) \quad ,$$

which eliminates the interference between isoscalar and isovector photons. Bulos et al.[52] have compared their measurements of $\pi^- p \to \rho^o n$ at 15 GeV with the asymmetry data of Burfeindt et al.[9] and Geweniger et al.[8] They conclude that the unnatural parity exchange cross sections are in good agreement as is the asymmetry for $|t| \leq 2m_\pi^2$. At almost all values of $|t|$, the natural parity exchange cross section for photoproduction is significantly larger than that for ρ production by pions.

In Figs. 26 and 27 we compare our measurements with those of Bulos et al.[52] Our conclusions are the same, thereby removing whatever uncer-

tainties may have been present due to the different energies of the ρ production and photoproduction data. Although the amount and quality of the data have improved with time, this particular failure of the Vector Dominance Model is essentially unchanged since the first experimental results and the early discussions by Diebold and Poirier.[53]

A comparison of the reaction $\pi^+ p \to \rho^o \Delta^{++}$ with $\pi - \bar{\Delta}$ photoproduction is also possible. However, this comparison involves line reversal (not merely time reversal as does the comparison for single pion production) as well as Vector Dominance. Any interference terms between Regge exchanges of opposite signature change sign under line reversal.[54,55] Taking the sum of the cross sections for the reactions $\gamma p \to \pi^- \Delta^{++}$ and $\gamma n \to \pi^+ \Delta^-$ eliminates isoscalar-isovector interference and allows comparison to the cross section and helicity frame density matrix elements for $\pi^+ p \to \rho^o \Delta^{++}$. The cross section and asymmetry relationships are

$$\frac{d\sigma}{dt}(\gamma p \to \pi^- \Delta^{++}) + \frac{d\sigma}{dt}(\gamma n \to \pi^+ \Delta^-)$$

$$= \frac{2\pi\alpha}{\gamma_\rho^2} \rho_{11} \frac{d\sigma}{dt}(\pi^+ p \to \rho^o \Delta^{++}) \quad ,$$

and

$$\Sigma = \frac{\rho_{1-1}}{\rho_{11}} \quad .$$

Boyarski et al.[43] have compared their photoproduction measurements with the $\pi^+ p \to \rho^o \Delta^{++}$ measurements of Aderholz et al.,[56] and they find that the photoproduction cross section is larger by about a factor of five. Cross section measurements of the double resonance process are difficult, and factor of two disagreements at the same incident energy are not uncommon (see Fig. 1 of Ref. 57). This can explain some, but not all, of

the discrepancy found by Boyarski et al.[43]

In Fig. 28, we compare our data with the 13.2 GeV cross section measurements of Gaidos et al.,[58] measurements which these authors consider to be upper limits. In making this comparison we have multiplied both our cross sections and those of Gaidos et al.[58] by $(s-m^2)^2$. This is equivalent to scaling our 16 GeV measurements down to the 13.2 GeV incident energy of Gaidos et al.[58] The scaled cross sections have the same t dependence, but differ by a factor of approximately 1.75. A substantial part of the change from earlier results comes from using different data for the $\pi^+ p \to \rho^o \Delta^{++}$ cross section, the different Δ normalizations, and the different energy dependences of the two processes.[48,57,59] This latter dependence is, of course, inconsistent with Vector Dominance.

The asymmetries for the two processes are in good agreement (Fig. 29). This test should be free of the systematic uncertainties in determining the cross sections. The good agreements between the t dependences of both cross sections and the asymmetries indicate that much of the previous trouble with the Vector Dominance comparison for $\pi\Delta$ photoproduction may be associated with the absolute normalization of the cross sections.

E. Single K^+ Photoproduction

The cross sections and asymmetries for $\gamma p \to K^+(\Lambda,\Sigma^o)$ and $\gamma D \to K^+(\Lambda,\Sigma^o,\Sigma^-)N_S$ are given in Table VII. The measurements from a hydrogen target agree with both the t dependence and the absolute normalization of Boyarski et al.[60] This normalization agreement is in contrast to the disagreement found in pion photoproduction. Many of the uncertainties in the absolute cross sections are shared by both pions and kaons, and we have not been able to understand why our kaon cross sections agree with

the earlier measurements while the pion ones do not. We believe that this normalization uncertainty does not affect our asymmetry measurements.

The asymmetries are shown in Figure 30. These measurements are consistent with one over most of the t range of the experiment; the only structure we observe is the rise of the asymmetry from zero as $|t|$ increases. At large $|t|$ the cross sections for all measured pseudoscalar photoproduction processes are dominated by perpendicularly polarized photons. This includes the measurements presented in this paper and both π^o and η photoproduction.[61,62] This common feature, together with the similar t dependences and comparable magnitudes of cross sections, gives a strong hint that similar mechanisms must be important for all these reactions.

Since the asymmetries for the sum of the kaon photoproduction reactions are close to one, and since the individual reactions have comparable cross sections, the asymmetries of the individual reactions must be close to one. In Table VIII we present the cross sections and asymmetries for the individual processes. The difficulty in determining the contribution of individual processes to the total yield (section IV.B) is reflected in the large error bars. The ratios of cross sections do not compare well with those of Boyarski et al.[60,63] This comparison is discussed in Appendix C. The asymmetry results for $\gamma p \to K^+\Lambda$ are the least uncertain; they are shown in Figure 31. The asymmetry, which is consistent with one for $-t \geq .13$ $(GeV/c)^2$, agrees with several photoproduction models.[64,65]

Our measurements can be combined with recoil Λ polarization measurements at 5 GeV by Vogel et al[66] (see Figure 31) to give a qualitative

picture of the s-channel amplitudes for K-Λ photoproduction. In terms of the s-channel amplitudes the polarized photon asymmetry is[67]

$$\Sigma = \frac{2\,\mathrm{Re}\,(g_1 g_4^* + g_2 g_3^*)}{\sum |g_i|^2}$$

where g_1 is the helicity non-flip amplitude, g_2 and g_3 are single flip amplitudes and g_4 is the double flip amplitude. For Σ close to one, it is necessary to have $g_1 \approx g_4^*$ and $g_2 \approx g_3^*$, but nothing can be said about the relative size of the pairs of amplitudes. The recoil Λ polarization is given by[67]

$$P = \frac{2\mathrm{Im}\,(g_1 g_3^* - g_2 g_4^*)}{\sum |g_i|^2}$$

With the recoil Λ polarization close to -1, $g_3 \approx g_1^* e^{-i\pi/2}$ and $g_2 \approx g_4^* e^{i\pi/2}$, but we can tell nothing about the relative sizes of these pairs of amplitudes. Combining these two results we find that all four s-channel amplitudes must be approximately equal in magnitude with the single flip amplitudes being 90° out of phase with the non-flip and double-flip amplitudes.

VI. Conclusions

From our study of the polarized photon asymmetries in pseudoscalar meson photoproduction, we conclude the following:

(1) All the reactions we studied are dominated by natural parity exchange at large $|t|$.

(2) The energy dependence for single pion photoproduction with parallel polarized photons is consistent with that expected from a pion Regge trajectory.

(3) There is significant interference between natural parity exchanges of opposite G-parity in both single pion and π-Δ photoproduction.

(4) There is evidence for some interference between unnatural parity exchanges of opposite G-parity in π-Δ photoproduction, but no evidence exists in single pion photoproduction.

(5) Although we observe a dip in the natural parity exchange cross section for $\gamma p \to \pi^- \Delta^{++}$ at $t = -0.15$ GeV^2, it seems unlikely that this channel is dominated by a single s-channel amplitude.

(6) The asymmetries at small $|t|$ for single pion and π-Δ photoproduction are well described by qualitative arguments relating them to the cross sections.

(7) Simple Vector Meson Dominance describes the unnatural parity single pion photoproduction cross sections, and the asymmetry for this process at low t. It fails completely for the natural parity cross section. It does describe the asymmetry for π-Δ photoproduction, and the shape, but not the magnitude, of the cross section.

(8) For $|t| > m_K^2$ the K^+ asymmetries are consistent with one.

(9) For $K^+\Lambda$ photoproduction the asymmetry is close to +1 and the recoil Λ polarization to -1, which implies all four s-channel amplitudes are of comparable magnitude.

(10) The fact that all pseudoscalar meson photoproduction processes observed to date show dominance of natural parity exchange, similar t dependencies, $1/k^2$ scaling, and cross sections of comparable magnitude, strongly suggests a common underlying mechanism for these reactions.

Acknowledgments

This work was supported by the Department of Energy under contract number EY-76-C-03-0515.

We wish to thank the staff of SLAC for their many contributions. R. Eisele, B. Humphrey and the other members of the Spectrometer Facilities Group helped design, construct and maintain much of the apparatus. J. Mark and his group provided the hydrogen target. The accelerator operating crews were at their usual best; it was a pleasure to work with them. SLAC and Cornell LNS staff have made many contributions to this manuscript.

Adam Boyarski, Stan Ecklund, Dave Coward, Burton Richter and Roy Schwitters have shared their knowledge with us and supported this work. One of us (J.P.R.) acknowledges useful conversations with G. Goldstein and J. Owens.

APPENDIX A

Missing-Mass-Squared in an Experiment with a Focussing Spectrometer and a Bremsstrahlung Beam

The intersection of a particle trajectory with the momentum and theta focal planes of the spectrometer measures both δ, the percentage deviation of the momentum from the central momentum p_o, and $\theta-\theta_o$, the deviation of the horizontal production angle from θ_o, the central angle of the spectrometer. For conceptual purposes, these focal planes can be combined into a single $\delta-\theta$ plane, shown in Fig. 32.

Given the masses of the target and detected particles, m_T and m_D respectively, and assuming a photon energy k, the missing-mass-squared of the undetected particle(s) is given by:

$$MM^2 = m_T^2 + m_D^2 - (2m_T p_o/\beta)(1+\delta/100) + 2k(m_T - p_o(1+\delta/100)(1/\beta - \cos\theta\cos\Phi)) .$$

In this equation β is the normalized velocity of m_D, taken to be a constant over the spectrometer acceptance, and Φ is the vertical production angle. Thus lines of constant missing-mass-squared have a slope in the $\delta-\theta$ plane of

$$\left.\frac{\partial\delta}{\partial\theta}\right|_{MM^2=\text{const}} = \frac{-100k(1+\delta/100)\ \sin\theta\cos\Phi}{m_T/\beta + k(1/\beta - \cos\theta\cos\Phi)} .$$

This slope is independent of p_o, and the dependence on δ, θ, and Φ is sufficiently weak that within the spectrometer acceptance the slope may be considered independent of these variables.

In the present experiment the spectrometer accepted only particles produced by photons of energies very near the bremsstrahlung end point. Thus one can divide the $\delta-\theta$ plane into bins of constant missing-mass-squared which are essentially independent of k. At a fixed photon

energy, the principal variation in the cross section at fixed p_o is due to the change in missing-mass with angle. By using bins of constant missing-mass-squared rather than bins of constant momentum, this variation of cross section within a bin is avoided. In labelling a bin, we have used the convention $K = E_o - 0.05$ GeV, where E_o is the end point energy.

APPENDIX B

Parametrizations Used in Fitting the Momentum Distributions

i. Photon Spectrum

The photon beam spectrum employed in the fits was determined by multiplying the calculated bremsstrahlung spectrum[17] from an amorphous radiator by the experimentally determined attenuation function.[15] This attenuation function, which accounted for the spectrum degradation by the graphite absorber, is discussed in Section II.A. In fitting data from the deuterium target, the photon beam spectrum was "smeared" to account for the Fermi motion of the target nucleons. The Hulthén[68] wavefunction for the deuteron was used for this modification. In the remainder of this appendix, we denote the photon beam spectrum by n(k). The normalization is such that the number of photons per equivalent quantum between k and k + dk is n(k)dk.

ii. The Reactions $\gamma N \to \pi N$, $\gamma N \to K\Lambda$, and $\gamma N \to K\Sigma$

As these reactions all have stable undetected recoil baryons, for any given detected particle momentum p, and production angle θ, only photons of a particular energy, k_o, can produce a yield. k_0 is given by:

$$k_o = \frac{m_R^2 - m_T^2 - m_D^2 + 2m_T E}{2(m_T - E + p \cos\theta)}$$

where m_R, m_T, and m_D are the masses of recoil, target, and detected particles, respectively, and E is the laboratory energy of the detected particle. The number of photons per equivalent quantum which can contribute to the yield is

$$n(k_o)dk = n(k_o) \frac{\partial k}{\partial p} dp$$

We evaluate the derivative $\partial k/\partial p$ at the nominal photon energy K (= 16 GeV). The cross section per equivalent quantum is given by

$$\frac{1}{Q}\frac{d^2\sigma}{d\Omega\,\frac{dp}{p}} = p\,\frac{\partial k}{\partial p}\,n(k_o)\,\frac{d\sigma(p)}{d\Omega} \quad .$$

At high energy, the cross sections for pseudoscalar meson photoproduction reactions differential in the laboratory solid angle are, to an excellent approximation, independent of the photon energy at a fixed t. Thus, at a fixed laboratory angle, the cross section depends on momentum only through the momentum dependence of t. We therefore use the approximation

$$\frac{d\sigma}{d\Omega}\,(p) = \frac{d\sigma}{d\Omega}\,(p_o)\,\exp\left(\left.\frac{dt}{dp}\right|_{p_o}(p-p_o)A\right)$$

where p_o is the detected particle momentum produced by a 16-GeV photon. The parameter A, the t dependent logarithmic slope of the π-N, K-Λ or K-Σ cross section, is taken from the results of Boyarski et al.[35,60] $\frac{d\sigma}{d\Omega}\,(p_o)$, the single unknown, is the cross section for photoproduction by 16-GeV photons. Combining these relations, we obtain:

$$\frac{1}{Q}\frac{d^2\sigma}{d\Omega\,\frac{dp}{p}} = p\,\frac{\partial k}{\partial p}\,n(k_o)\,\exp\left(\left.\frac{dt}{dp}\right|_{p_o}(p-p_o)A\right)\frac{d\sigma}{d\Omega}\,(p_o) \quad .$$

iii. The Reactions $\gamma N \rightarrow \pi\Delta(1236)$

For this case, where the recoil mass is not sharp but has a broad resonance shape, the differential cross section for a photon of energy k to produce a $\pi\Delta$ final state with a Δ of mass m is:

$$\frac{d\sigma}{d\Omega}(k,m) = \frac{d\sigma_o}{d\Omega}(k,m)\ BW(m)\, d\,m^2$$

$$= \frac{d\sigma_o}{d\Omega}(k,m)\left[\frac{1}{\pi}\frac{m_o\,\Gamma(m)}{\left(m_o^2 - m^2\right)^2 + m_o^2\,\Gamma^2(m)}\right] d\,m^2 \quad .$$

where m_o is the central mass of the $\Delta(= 1.236\ \mathrm{GeV}/c^2)$, $\Gamma(m)$ is the mass dependent width, and $d\sigma_o/d\Omega\ (k,m)$ is the "stable particle" production cross section. We use the CERN 3-3 phase shifts[69] to calculate this width:[70]

$$\Gamma(m) = \tan\delta_{33}\left(m_o^2 - m^2\right)/m_o \quad .$$

We assume the only mass and energy dependence of $d\sigma_o/d\Omega$ is due to the dependence of the π-Δ two-body phase space on mass and energy and to the variation of t with these quantities. Thus, we have

$$\frac{d\sigma_o}{d\Omega}(k,m) = \frac{d\sigma_o}{d\Omega}(K,m_o)\,\frac{\text{phase space }(k,m)}{\text{phase space }(K,m_o)}$$

$$\times \exp\left(A_{\pi\Delta}\left(t(k,m) - t(K,m_o)\right)\right)$$

where $A_{\pi\Delta}$ is the t dependent logarithmic slope of the $\pi\Delta$ cross section and K is the nominal photon energy, 16 GeV. We take $A_{\pi\Delta}$ from the results of Boyarski et al.[43] Denoting the phase space ratio as PS(m,k), we obtain:

$$\frac{d^2\sigma}{Qd\Omega\,\frac{dp}{p}} = p\frac{d\sigma_o}{d\Omega}(K,m_o)\int_{k_{min}}^{E_o}\left[n(k)\,PS(m,k)\exp\left(A_{\pi\Delta}\left(t(k,m)-t(K,m_o)\right)\right)BW(m)\left|\frac{dm^2}{dp}\right|\right]dk$$

where k_{min} is the lowest photon energy which can contribute to the yield. Again, the single unknown is the cross section for π-Δ production with a Δ mass m_o by photons of energy K.

Note that our definition of the cross section is analogous to that suggested by Spital and Yennie[71] for ρ meson production. The cross sections we quote are larger than those of Boyarski et al.[43,48] and Bingham et al.[72] by constant factors of 1.13 and 1.22 respectively. These differences arise because these authors have chosen to normalize the Breit-Wigner forms they use, something we have not done.

iv. The Reactions $\gamma N \rightarrow \pi N^*(1520)$

To obtain acceptable fits to our pion momentum spectra, it was found necessary to include π-N*(1520) production in those channels where it is allowed by isospin conservation. We have parametrized the cross section for this reaction in the same way as for π-Δ production, using the general form for the mass dependent width for baryon resonances.[70] The uncertainties are sufficiently great that we quote no results for this reaction.

v. Pions from ρ Decay

The complete ρ decay distribution is given in Refs. 13 and 14. We have approximated the helicity frame density matrix elements as:

$$\rho^0_{00} = \mathrm{Re}\rho^0_{10} = \rho^0_{1-1} = \rho^1_{11} = \rho^1_{00} = \mathrm{Re}\rho^1_{10} = \mathrm{Im}\rho^2_{10} = 0$$

and

$$\rho^1_{1-1} = -\mathrm{Im}\rho^2_{1-1} = 0.5 \quad .$$

The resulting decay distribution is:

$$W(\cos\theta,\phi,\Phi_\gamma) = \frac{3}{8\pi}\sin^2\theta\,(1 - P\cos 2(\phi-\Phi_\gamma)) \quad ,$$

where the angles are defined in Fig. 33 and P is the degree of linear polarization.

The only variable fixed by the experiment is one pion momentum. The distributions of photon energy and ρ meson mass are also known. We express other quantities in terms of these three variables and, for convenience, work in the γ-p center of mass. Variables in this frame are denoted with an asterisk. The relation between the ρ mass, $m_{\pi\pi}$; ρ momentum, p^*_ρ; and photon energy k* is:

$$k^* = \left(2p^{*2}_\rho + m^2_{\pi\pi} + 2\sqrt{\left(p^{*2}_\rho + m^2_{\pi\pi}\right)\left(p^{*2}_\rho + m^2_p\right)}\right)/2\left(\sqrt{p^{*2}_\rho + m^2_{\pi\pi}} + \sqrt{p^{*2}_\rho + m^2_p}\right)$$

where m_p is the proton mass. For a given ρ momentum and mass, the pion momentum determines the decay angle θ^*_d by

$$\cos\theta^*_d = \left[2E^*_\rho E^*_\pi - m^2_{\pi\pi}\right]/2p^*_\rho p^*_\pi \quad .$$

ρ mesons with momentum vectors lying on the surface of a cone of half angle θ^*_d with an axis along the pion momentum can decay into pions of momentum p^*_π. The angular range of the detected pions is determined by the pion momentum bite by

$$d(\cos\theta^*_d) = dp^*_\pi \frac{d(\cos\theta^*_d)}{dp^*_\pi} \quad .$$

The ππ production cross section is

$$\frac{d^2\sigma}{dt\,dm^2_{\pi\pi}} = \frac{d\sigma_o\left(m^2_{\pi\pi}\right)}{dt}\,(BW)$$

where σ_o is the stable particle production cross section and BW is the Breit-Wigner for the ρ:

$$BW = \frac{1}{\pi} \frac{m_\rho \Gamma(m_{\pi\pi})}{\left(m_{\pi\pi}^2 - m_\rho^2\right)^2 + m_\rho^2 \Gamma^2(m_{\pi\pi})} \quad .$$

The mass dependent width is taken from Jackson[70]

$$\Gamma(m_{\pi\pi}) = \Gamma_\rho \left(\frac{Q(m_{\pi\pi})}{Q(m_\rho)}\right)^3 \left(\frac{2Q^2(m_\rho)}{Q^2(m_\rho) + Q^2(m_{\pi\pi})}\right)$$

where

$$Q(m) = \frac{\sqrt{m^2 - 4m_\pi^2}}{2}$$

is the π momentum in the ρ rest frame. We have used $\Gamma_\rho = 0.125$ GeV/c^2 and $m_\rho = 0.765$ GeV/c^2.

We assume that the stable particle cross section depends on the photon energy and ρ mass through the dependence of t and the two body phase space (for $\gamma p \to p(\pi\pi)$) on these factors, and on the ρ mass through a Ross-Stodolsky factor:[73]

$$\frac{d\sigma_o\left(m_{\pi\pi}^2\right)}{dt} = Ae^{bt}(PS)\left(\frac{m_\rho}{m_{\pi\pi}}\right)^{n(t)}$$

where A is for 16 GeV photons, b and $n(t) = \alpha + \beta t$ are given in Refs. 13 and 14, and PS is the phase space ratio

$$PS = \sqrt{\frac{\lambda\left(s, m_{\pi\pi}^2, m_\rho^2\right)}{\lambda\left(s_o, m_\rho^2, m_p^2\right)}} \quad \frac{s_o}{s} \quad .$$

In this equation s_o is the square of the center of mass energy for the reaction when a photon energy of 16 GeV is assumed. Also,

$$\lambda(a,b,c) = a^2 + b^2 + c^2 - 2ab - 2ac - 2bc \quad .$$

The integration over the azimuthal angle of the cone can be done analytically, and the resulting center of mass cross section is transformed into the laboratory to be integrated over the photon spectrum and the ρ mass shape. The only free parameter is A. Despite the extensive ρ photoproduction data available, we have allowed A to be a free parameter, as the background to the $\pi\Delta$ reaction is from a ρ mass region where data is unavailable.

APPENDIX C

K^+ Photoproduction. Cross Section Ratios and Exotic Exchanges.

In Table VIII we present the cross section and asymmetry results for the processes $\gamma p \to K^+\Lambda$, $\gamma p \to K^+\Sigma^o$ and $\gamma D \to K^+(\Sigma^o,\Sigma^-)$. To determine these results it is necessary to determine the contribution of each process to the step in the yield. A look at Fig. 13 should convince the reader of the difficulty of the procedure. The resultant errors are large and highly correlated, and the possibility of additional errors in the data and fitting procedures cannot be eliminated. The determination of the results for each of the three processes has different problems.

For $\gamma p \to K^+\Lambda$ the asymmetry is determined reasonably well. With our known momentum resolution the highest momentum portion of the K^+ yield must be due to $K^+\Lambda$ production. The $K^+\Lambda$ asymmetry is determined by this portion of the yield. The $K^+\Lambda$ cross section is more difficult to determine because one in effect uses the momentum resolution and the initial rate of rise of the yield to measure the cross section. Small effects such as magnet hysteresis or non-Gaussian resolutions could significantly affect the results.

Both the cross section and asymmetry for $\gamma p \to K^+\Sigma^o$ are affected by any error in the $K^+\Lambda$ quantities. The reason is that $K^+\Lambda$ is contributing to the yield at all momenta which are being used to measure the $K^+\Sigma^o$ cross section and asymmetry. The ratio of $K^+\Sigma^o$ to $K^+\Lambda$ cross sections is shown in Fig. 34. We find a generally lower result than Boyarski et al.[60]

The results for $\gamma D \to K^+(\Sigma^o,\Sigma^-)$ suffer from the same problem; they are very sensitive to any error in the $\gamma p \to K^+\Lambda$ measurements. In Fig. 34 we

compare our results for the ratio R_Σ of $\gamma D \to K^+(\Sigma^o,\Sigma^-)$ to $\gamma p \to K^+\Sigma^o$ with measurements at 11 GeV.[63] At 11 GeV where the Λ-Σ separation is easier, this ratio averaged over all data points is 2.37 ± 0.11. This is not consistent with the value of three expected for pure isotopic spin 1/2 in the t-channel.

Our ratio has an average value of 2.73 ± 0.18 which is consistent with three. We see no evidence for exotic exchanges in K^+ photoproduction. However, we do not feel this result is in disagreement with the result at 11 GeV because of the difficulty in measuring this ratio from our data.

References and Footnotes

1. P. Stichel, Z. Phys. 180, 170 (1964).

2. J. P. Ader, M. Capdeville, G. Cohen-Tannoudji, and Ph. Salin, Nuovo Cimento 56A, 952 (1968). F. Ravndal, Phys. Rev. D2, 1278 (1970).

3. N. Cabibbo, G. Da Prato, G. De Franceschi and U. Mosco, Phys. Rev. Lett. 9, 270 (1962); N. Cabibbo et al., Nuovo Cimento 27, 979 (1963).

4. C. Berger, G. McClellan, N. Mistry, H. Ogren, B. Sandler, J. Swartz, P. Walstrom, R. L. Anderson, D. Gustavson, J. Johnson, I. Overman, R. Talman, B. H. Wiik, D. Worcester and A. Moore, Phys. Rev. Lett. 25, 1366 (1970).

5. D. J. Sherden, R. H. Siemann, C. K. Sinclair, D. J. Quinn, J. P. Rutherfoord and M. A. Shupe, Phys. Rev. Lett. 30, 1230 (1973); Erratum Phys. Rev. Lett. 31, 667 (1973).

6. D. J. Quinn, J. P. Rutherfoord, M. A. Shupe, D. J. Sherden, R. H. Siemann and C. K. Sinclair, Phys. Rev. Lett. 34, 543 (1975).

7. Z. Bar-Yam, J. De Pagter, J. Dowd, W. Kern, D. Luckey and L. S. Osborne, Phys. Rev. Lett. 25, 1053 (1970).

8. Chr. Geweniger, P. Heide, U. Kötz, R. A. Lewis, P. Schmüser, H. J. Skronn, H. Wahl and K. Wegener, Phys. Lett. 29B, 41 (1969).

9. H. Burfeindt, G. Buschhorn, C. Geweniger, P. Heide, R. Kotthaus, H. Wahl and K. Wegener, Phys. Lett. 33B, 509 (1970).

10. R. F. Schwitters, J. Leong, D. Luckey, L. S. Osborne, A. M. Boyarski S. D. Ecklund, R. Siemann and B. Richter, Phys. Rev. Lett. 27, 120 (1971).

11. Z. Bar-Yam, J. De Pagter, J. Dowd and W. Kern, Phys. Rev. Lett. 24, 1078 (1970).

12. H. Burfeindt, G. Buschhorn, C. Geweniger, R. Kotthaus, H. J. Skronn, H. Wahl and K. Wegener, Nucl. Phys. B59, 87 (1973).

13. J. Ballam, G. B. Chadwick, R. Gearhart, Z.G.T. Guiragossian, J. J. Murray, P. Seyboth, C. K. Sinclair, I. O. Skillicorn, H. Spitzer, G. Wolf, H. H. Bingham, W. B. Fretter, K. C. Moffeit, W. J. Podolsky, M. S. Rabin, A. H. Rosenfeld, R. Windmolders and R. H. Milburn, Phys. Rev. D5, 545 (1972).

14. J. Ballam, G. B. Chadwick, Y. Eisenberg, E. Kogan, K. C. Moffeit, P. Seyboth, I. O. Skillicorn, H. Spitzer, G. Wolf, H. H. Bingham, W. B. Fretter, W. J. Podolsky, M. S. Rabin, A. H. Rosenfeld and G. Smadja, Phys. Rev. D7, 3150 (1973).

15. R. L. Eisele, D. J. Sherden, R. H. Siemann, C. K. Sinclair, D. J. Quinn, J. P. Rutherfoord and M. A. Shupe, Nucl. Instrum. Methods 113, 489 (1973).

16. G. E. Fischer and Y. Murata, Nucl. Instrum. Methods 78, 25 (1970).

17. R. A. Early, SLAC-TN-66-15 (1966) unpublished.

18. SLAC Users Handbook (1971) p. D. 3-7, unpublished; A. M. Boyarski, D. H. Coward, S. Ecklund, B. Richter, D. Sherden, R. Siemann and C. Sinclair, Phys. Rev. Lett. 26, 1600 (1971).

19. R. S. Larsen and D. Horelick, SLAC Report No. SLAC-PUB-559, (1969) unpublished; or in the Proceedings of the Symposium on Beam Intensity Measurement, Daresbury, 1968, unpublished, pp. 260-279.

20. D. Yount, Nucl. Instrum. Methods 52, 1 (1967).

21. R. L. Anderson, Nucl. Instrum. Methods 70, 87 (1969)

22. A. M. Boyarski, D. H. Coward, S. D. Ecklund, B. Richter, D. J. Sherden, R. H. Siemann and C. K. Sinclair, Phys. Rev. D14, 1733 (1976).

23. SLAC Users Handbook (1971) p. D.3-5, unpublished.

24. A. M. Boyarski, private communication.

25. R. F. Schwitters, Ph. D. Thesis, MIT, 1971, unpublished.

26. The Jacobians for single pion or single K^+ photoproduction are evaluated at 16.00 GeV incident energy. Treating these as constants is a good approximation in the momentum range we cover. In this paper, k refers to a general photon energy, and K to the specific energy E_0 -0.05 GeV.

27. E. Taylor, private communication.

28. We use the same stringent region as Boyarski et al. Their calculation of the acceptance of this region was used in references 35, 36, 43, 48, 60 and 63.

29. We have used the program SOLVE written by C. Moore.

30. References 13, 14 and K. Moffeit, private communication.

31. K. C. Moffeit, J. Ballam, G. B. Chadwick, M. Della-Negra, R. Gearhart, J. J. Murray, P. Seyboth, C. K. Sinclair, I. O. Skillicorn, H. Spitzer, G. Wolf, H. H. Bingham, W. B. Fretter, W. J. Podolsky, M. S. Rabin, A. H. Rosenfeld,

R. Windmolders, G. P. Yost and R. H. Milburn, Phys. Rev. D5, 1603 (1972).

32. S. D. Drell, Phys. Rev. Lett. 5, 278 (1960).

33. F. von Holtey, Proceedings of the Symposium on Meson Photo- and Electro-Production at Low and Intermediate Energies, Bonn (1970); published by Springer-Verlag, New York.

34. W.S.C. Williams, An Introduction to Elementary Particles, 2nd ed., New York, Academic Press, 1971; p. 444.

35. A. M. Boyarski, F. Bulos, W. Busza, R. Diebold, S. D. Ecklund, G. E. Fischer, J. R. Rees and B. Richter, Phys. Rev. Lett. 20, 300 (1968).

36. A. M. Boyarski, R. Diebold, S. D. Ecklund, G. E. Fischer, Y. Murata, B. Richter and W.S.C. Williams, Phys. Rev. Lett. 21, 1767 (1968).

37. D. I. Julius, Nucl. Phys. B40, 409 (1972).

38. B. H. Kellett, Nucl. Phys. B25, 205 (1970).

39. Z. Bar-Yam, J. de Pagter, M. M. Hoenig, W. Kern, D. Luckey and L. S. Osborne, Phys. Rev. Lett. 19, 40 (1967).

40. P. Heide, U. Kötz, R. A. Lewis, P. Schmüser, H. J. Skronn and H. Wahl, Phys. Rev. Lett. 21, 248 (1968).

41. The identification of the A_3 as $J^P = 2^-$ makes it a strong candidate as the first recurrence of the pion. G. Ascoli, D. V. Brockway, L. Eisenstein, J. D. Hansen, M. L. Ioffredo, U. E. Kruse, T. F. Johnston, A. W. Key, J. D. Prentice,

T. S. Yoon, C. Caso, G. Tomasini, P. von Handel, P. Schilling, G. Costa, S. Ratti, L. Mosca, W. C. Harrison, D. Heyda, W. H. Johnson, Jr., J. K. Kim, M. E. Law, J. E. Mueller, B. M. Salzberg, L. K. Sisterson, H. Grassler, W. D. Nowak, M. Rost, G. T. Jones, W. Kittel, S. Brandt, P. H. Smith, W. D. Shephard, N. N. Biswas, N. M. Casca, V. P. Kenney, W. B. Madden, A. R. Erwin, R. Morse, B. Y. Oh, W. Robertson and W. D. Walker, Phys. Rev. D7, 669 (1973).

42. R.C.E. Devenish, W. J. Leigh and D. H. Lyth, Nuovo Cimento 1A, 475 (1971).

43. A. M. Boyarski, R. Diebold, S. D. Ecklund, G. E. Fischer, Y. Murata, B. Richter and M. Sands, Phys. Rev. Lett. 25, 695 (1970); Erratum, Phys. Rev. Lett. 25, 1148 (1970).

44. Y. Eisenberg, B. Haber, U. Karshon, J. Mikenberg, S. Pitluck, E. E. Ronat, A. Shapira and G. Yekutieli, Phys. Lett. 48B, 354 (1974).

45. G. R. Goldstein and J. F. Owens, Nucl. Phys. B71, 461 (1974).

46. R. B. Clark, Phys. Rev. D18, 1444 (1978).

47. P. Stichel and M. Scholz, Nuovo Cimento 34, 1381 (1964).

48. A. M. Boyarski, R. Diebold, S. D. Ecklund, G. E. Fischer, Y. Murata, B. Richter and W.S.C. Williams, Phys. Rev. Lett. 22, 148 (1969).

49. J. A. Campbell, R. B. Clark and D. Horn, Phys. Rev. D2, 217 (1970).

50. H. Harari, Rapporteur talk published in the Proceedings of the Fourth International Symposium on Electron and Photon Interactions at High Energies, Daresbury, 1969 (edited by D. W. Braben and R. E. Rand).

51. T. H. Bauer, R. D. Spital, D. R. Yennie and F. M. Pipkin, Rev. Mod. Phys. 50, 261 (1978).

52. F. Bulos, R. K. Carnegie, G. E. Fischer, E. E. Kluge, D.W.G.S. Leith, H. L. Lynch, B. Ratcliff, B. Richter, H. H. Williams, S. H. Williams, Phys. Rev. Lett. 26, 1457 (1971).

53. R. Diebold and J. Poirier, Phys. Rev. Lett. 22, 255 (1969).

54. E. Gotsman, Lett. Nuovo Cimento 2, 563 (1969).

55. F. Gilman, Phys. Lett. 29B, 673 (1969).

56. M. Aderholz, M. Deutschmann, E. Keppel, G. Kraus, H. Weber, C. Grote, H. H. Kaufmann, S. Novak, M. Walter, H. Bottcher, T. Byer, V. T. Cocconi, P. F. Dalpiaz, J. D. Hansen, G. Kellner, W. Kittel, M. Markytan, A. Mihul, D.R.O. Morrison and H. T. Tøfte , Nucl. Phys. B8, 45 (1968).

57. R. O. Maddock, G. F. Pinter, D. Evans, C. Caso, F. Conte, D. Teodoro, G. Tomasini, H. Fesefeld, P. von Handel, H. Nagel, P. K. Schilling, G. Cecchet, L. Mandelli, S. Ratti, L. Tallone Lombardi, M. Chaumet, A. Daudin, M. Faccini, M. A. Jabiol, J. F. Lefur, C. Lewin and J. Mallet, Nuovo Cimento 5A, 433 (1971).

58. J. A. Gaidos, A. A. Hirata, R. J. DeBonte, T. A. Mulera, G. Thompson and R. B. Willmann, Nucl. Phys. B72, 253 (1974).

59. N. N. Biswas, N. M. Cason, M. S. Farber, J. A. Helland, M. J. Hones, V. P. Kenney, J. T. McGahan, J. A. Poirier, J. T. Powers, O. R. Sander and W. D. Shephard, Phys. Rev. D2, 2529 (1970).

60. A. M. Boyarski, F. Bulos, W. Busza, R. Diebold, S. D. Ecklund, G. E. Fischer, Y. Murata, J. R. Rees, B. Richter and W.S.C. Williams, Phys. Rev. Lett. 22, 1131 (1969).

61. R. L. Anderson, D. B. Gustavson, J. R. Johnson, I. D. Overman, D. M. Ritson, B. H. Wiik and D. Worcester, Phys. Rev. D4, 1937 (1971).

62. P. J. Bussey, C. Raine, J. G. Rutherglen, P.S.L. Booth, L. J. Carroll, P. R. Daniel, A. W. Edwards, C. J. Hardwick, J. R. Holt, J. N. Jackson, J. Norem, W. H. Range, W. Galbraith, V. H. Rajaratnam, C. Sutton, M. C. Thorne and P. Waller, Phys. Lett. 61B, 479 (1976).

63. A. M. Boyarski, R. Diebold, S. D. Ecklund, G. E. Fischer, Y. Murata, B. Richter and M. Sands, Phys. Lett. 34B, 547 (1971).

64. G. R. Goldstein, J. F. Owens and J. P. Rutherfoord, Nucl. Phys. B53, 197 (1973).

65. N. Levy, W. Majerotto and B. J. Read, Nucl. Phys. B55, 493 (1973).

66. G. Vogel, H. Burfeindt, G. Buschhorn, P. Heide, U. Kötz, K. -H. Mess, R. Schmüser, B. Sonne and B. H. Wiik, Phys. Lett. 40B, 513 (1972).

67. J. D. Jackson and C. Quigg, Nucl. Phys. B22, 301 (1970).

68. L. Hulthén, Phys. Rev. 61, 671 (1942)

69. A. Donnachie, R. G. Kirsopp and C. Lovelace, Phys. Lett. 26B, 161 (1968).

70. J. D. Jackson, Nuovo Cimento 34, 1644 (1964).

71. R. Spital and D. R. Yennie, Phys. Rev. D9, 126 (1974).

72. H. H. Bingham, W. B. Fretter, K. C. Moffeit, W. J. Podolsky, M. S. Rabin, A. H. Rosenfeld, R. Windmolders, J. Ballam, G. B. Chadwick, R. Gearhart, Z.G.T. Guiragossian, M. Menke, J. J. Murray, P. Seyboth, A. Shapira, C. K. Sinclair, I. O. Skillicorn, G. Wolf and R. H. Milburn, Phys. Rev. Lett. 25, 1223 (1970).

73. M. Ross and L. Stodolsky, Phys. Rev. 149, 1172 (1966).

Table I

Corrections for Detection Inefficiencies (not including deadtimes)

Source of Lost Events		Correction
Hodoscope inefficiency (blank hodoscopes, undecodable patterns, extra tracks)		1.081 ± 0.020
Failure to reach first range counter due to interaction in the differential counter		1.026 ± 0.006
Hadron identified as an electron by shower counter		1.055 ± 0.006
Gamma ray loss in target and material	H_2	1.059 ± 0.005
upstream of target	D_2	1.067 ± 0.005
Absorption of hadrons in target	π, H_2	1.050 ± 0.010
	π, D_2	1.117 ± 0.020
	K, H_2	1.036 ± 0.010
	K, D_2	1.082 ± 0.020
Absorption of hadrons in counters		1.073 ± 0.010
Threshold Cerenkov counter inefficiency	π^+	1.012 ± 0.005
or misidentification	π^-	1.018 ± 0.005
	K	1.025 ± 0.005
Differential Cerenkov counter inefficiency	K	1.042 ± 0.010
Decay in flight (p is the momentum in GeV)	π	exp(46.8/55p)
	K	exp(46.8/7.5p)
Typical total corrections	π, H_2	1.50 ± 0.03
	π, D_2	1.60 ± 0.03
	K, H_2	2.20 ± 0.03
	K, D_2	2.30 ± 0.03

Table II

Cross Section and Asymmetry Results for $\gamma p \rightarrow \pi^+ n$ at 16 GeV

$-t$ $(GeV/c)^2$	$d\sigma/dt$ $(\mu b/(GeV/c)^2)$	Σ
0.0055	*	0.27 ± 0.09
0.0122	*	0.55 ± 0.08
0.0173	*	0.78 ± 0.19
0.0337	0.185 ± 0.006	1.01 ± 0.05
0.0530	0.152 ± 0.010	1.02 ± 0.05
0.0826	0.147 ± 0.007	0.89 ± 0.09
0.155	0.136 ± 0.006	0.80 ± 0.04
0.257	0.113 ± 0.003	0.77 ± 0.06
0.418	0.086 ± 0.003	0.74 ± 0.04
0.602	0.0559 ± 0.0023	0.88 ± 0.05
0.826	0.0297 ± 0.0010	0.93 ± 0.04
1.499	0.0028 ± 0.0003	1.13 ± 0.13

*The analysis of these data points did not give absolute cross sections.

Table III

Results for $\gamma D \to \pi^+ nn_s$

$-t$ $(GeV/c)^2$	$\frac{d\sigma/dt\ (\gamma D \to \pi^+ nn_s)}{d\sigma/dt\ (\gamma p \to \pi^+ n)}$	Σ
0.0055	*	0.19 ± 0.12
0.0122	*	0.47 ± 0.13
0.0173	*	0.69 ± 0.17
0.0337	0.93 ± 0.06	1.02 ± 0.13
0.0530	0.86 ± 0.06	0.96 ± 0.12
0.0826	0.99 ± 0.04	1.07 ± 0.12
0.155	1.00 ± 0.06	0.67 ± 0.11
0.257	1.09 ± 0.05	0.82 ± 0.07
0.418	1.08 ± 0.07	0.86 ± 0.06
0.602	1.00 ± 0.09	0.96 ± 0.07
0.826	1.07 ± 0.08	1.11 ± 0.06
1.193	**	1.08 0.10

*The analysis of these data points did not give cross section ratios.

**The cross section for $\gamma p \to \pi^+ n$ was not measured at this t value.

Table IV

Results for $\gamma D \to \pi^- pp_s$

$-t\ (GeV/c)^2$	$R \equiv \frac{d\sigma/dt\ (\gamma D \to \pi^- pp_s)}{d\sigma/dt\ (\gamma D \to \pi^+ nn_s)}$	Σ
0.0055	*	0.04 ± 0.10
0.0122	*	0.38 ± 0.10
0.0173	*	0.59 ± 0.16
0.0337	0.708 ± 0.043	0.98 ± 0.07
0.0530	0.662 ± 0.046	0.91 ± 0.07
0.0826	0.473 ± 0.020	0.57 ± 0.10
0.155	0.318 ± 0.022	0.47 ± 0.07
0.205	**	0.35 ± 0.10
0.257	0.294 ± 0.019	0.55 ± 0.09
0.418	0.357 ± 0.034	0.74 ± 0.07
0.602	0.496 ± 0.058	0.85 ± 0.07
0.826	0.569 ± 0.057	0.94 ± 0.07
1.193	0.55 ± 0.11	1.06 ± 0.11

*The analysis for these data points did not give cross section ratios.

**The cross section for $\gamma D \to \pi^+ nn_s$ was not measured at this t value.

TABLE V

Cross Section and Asymmetry Results for $\pi\Delta$

Photoproduction from Hydrogen

	$\gamma p \to \pi^+ \Delta^o$		$\gamma p \to \pi^- \Delta^{++}$	
$-t(GeV/c)^2$	$d\sigma/dt(\mu b/(GeV/c)^2)$	Σ	$d\sigma/dt(\mu b/(GeV/c)^2)$	Σ
0.0058	*	-0.28 ± 0.21	*	-0.16 ± 0.08
0.0122	*	-0.33 ± 0.20	*	-0.25 ± 0.08
0.0173	*	-0.52 ± 0.25	*	-0.43 ± 0.19
0.0337	0.426 ± 0.053	-0.30 ± 0.19	1.039 ± 0.035	-0.47 ± 0.05
0.0520	0.315 ± 0.045	-0.59 ± 0.21	0.690 ± 0.041	-0.64 ± 0.08
0.0816	0.260 ± 0.040	-0.10 ± 0.21	0.492 ± 0.024	-0.67 ± 0.10
0.152	0.177 ± 0.024	0.03 ± 0.20	0.218 ± 0.013	-0.89 ± 0.14
0.252	0.124 ± 0.013	0.39 ± 0.16	0.1116 ± 0.0064	-0.62 ± 0.10
0.408	0.0774 ± 0.0058	0.89 ± 0.17	0.0732 ± 0.0026	0.23 ± 0.06
0.592	0.0521 ± 0.0031	0.85 ± 0.18	0.0531 ± 0.0013	0.75 ± 0.07
0.806	0.0216 ± 0.0022	0.88 ± 0.21	- - - - - - - -	- - - - - - -

*The analysis of these data points did not give absolute cross sections.

TABLE VI

Cross Section and Asymmetry Results for $\pi\Delta$

Photoproduction from Deuterium

	$\gamma D \to \pi^+ \Delta N_s$		$\gamma D \to \pi^- \Delta N_s$	
$-t(GeV/c)^2$	$d\sigma/dt(\mu b/(GeV/c)^2)$	Σ	$d\sigma/dt(\mu b/(GeV/c)^2)$	Σ
0.0337	1.52 ± 0.11	-0.23 ± 0.11	1.36 ± 0.10	-0.49 ± 0.09
0.0520	1.008 ± 0.098	-0.27 ± 0.10	0.851 ± 0.086	-0.66 ± 0.10
0.0816	0.878 ± 0.062	-0.20 ± 0.11	0.614 ± 0.060	-0.68 ± 0.13
0.152	0.547 ± 0.040	0.19 ± 0.09	0.316 ± 0.038	-0.75 ± 0.16
0.252	0.361 ± 0.021	0.28 ± 0.08	0.141 ± 0.019	-0.41 ± 0.13
0.408	0.244 ± 0.014	0.57 ± 0.09	0.105 ± 0.010	0.21 ± 0.11
0.592	0.150 ± 0.012	0.59 ± 0.11	0.0728 ± 0.0062	0.55 ± 0.10
0.806	0.0836 ± 0.0048	0.79 ± 0.09	0.0452 ± 0.0030	0.78 ± 0.10
1.173	0.0224 ± 0.0033	0.47 ± 0.18	0.0128 ± 0.0021	0.76 ± 0.22

TABLE VII

Cross Section and Asymmetry Results for K^+

Meson Photoproduction from Hydrogen and Deuterium

	$\gamma p \rightarrow K^+(\Lambda, \Sigma^o)$		$\gamma D \rightarrow K^+(\Lambda, \Sigma^o, \Sigma^-)N_s$	
$-t(GeV/c)^2$	$d\sigma/dt(\mu b/(GeV/c)^2)$	Σ	$d\sigma/dt(\mu b/(GeV/c)^2)$	Σ
.015	0.0454 ± 0.0035	0.04 ± 0.11	0.0574 ± 0.0051	0.05 ± 0.28
.037	0.0638 ± 0.0050	0.61 ± 0.12	0.104 ± 0.009	0.97 ± 0.23
.056	0.0701 ± 0.0054	0.73 ± 0.09	0.105 ± 0.009	0.80 ± 0.18
.086	0.0762 ± 0.0059	0.76 ± 0.10	0.127 ± 0.010	1.37 ± 0.15
.16	0.0860 ± 0.0065	0.98 ± 0.06	0.148 ± 0.012	1.20 ± 0.09
.26	0.0801 ± 0.0015	1.02 ± 0.07	0.135 ± 0.004	0.96 ± 0.07
.42	0.0665 ± 0.0011	0.92 ± 0.07	0.101 ± 0.002	0.90 ± 0.09
.60	0.0324 ± 0.0008	0.94 ± 0.09	0.0554 ± 0.0015	0.93 ± 0.11
.83	0.0149 ± 0.0005	0.97 ± 0.08	0.0265 ± 0.0008	0.94 ± 0.12

TABLE VIII

Cross Section and Asymmetry Results for $K^+\Lambda$ and $K^+\Sigma$ Photoproduction from Hydrogen and Deuterium

	$\gamma p \to K^+\Lambda$		$\gamma p \to K^+\Sigma^o$			$\gamma D \to K^+(\Sigma^o,\Sigma^-)\,N_s$		
$-t(GeV/c)^2$	$d\sigma/dt(\mu b/GeV^2)$	Σ	$d\sigma/dt(\mu b/GeV^2)$	Σ	R_p	$d\sigma/dt(\mu b/GeV^2)$	Σ	R_Σ
.015	0.0302 ±0.0033	-0.26 ±0.25	0.0152 ±0.0027	1.00 ±0.75	0.50 ±0.14	0.0322 ±0.0051	0.58 ±1.02	2.12 ±0.50
.037	0.0431 ±0.0053	0.28 ±0.30	0.0208 ±0.0045	1.43 ±0.79	0.48 ±0.16	0.069 ±0.010	1.06 ±0.57	3.31 ±0.86
.056	0.0491 ±0.0054	0.47 ±0.21	0.0210 ±0.0044	1.68 ±0.76	0.42 ±0.13	0.073 ±0.010	1.14 ±0.50	3.47 ±0.87
.086	0.0432 ±0.0055	0.47 ±0.28	0.0330 ±0.0055	1.11 ±0.50	0.76 ±0.22	0.080 ±0.010	0.09 ±0.44	2.41 ±0.50
.16	0.0499 ±0.0043	0.99 ±0.14	0.0362 ±0.0038	0.98 ±0.26	0.72 ±0.14	0.095 ±0.011	1.26 ±0.29	2.63 ±0.40
.26	0.0507 ±0.0035	0.81 ±0.20	0.0294 ±0.0041	1.53 ±0.48	0.58 ±0.12	0.0868 ±0.0055	1.04 ±0.20	2.95 ±0.45
.42	0.0314 ±0.0025	0.76 ±0.21	0.0230 ±0.0030	1.26 ±0.40	0.73 ±0.15	0.0653 ±0.0061	0.88 ±0.27	2.84 ±0.45
.60	0.0194 ±0.0019	1.15 ±0.25	0.0130 ±0.0023	0.45 ±0.51	0.66 ±0.18	0.0373 ±0.0049	1.13 ±0.34	2.88 ±0.63
.83	0.0098 ±0.0008	0.72 ±0.19	0.0051 ±0.0009	1.83 ±0.57	0.52 ±0.13	0.0160 ±0.0032	0.97 ±0.47	3.11 ±0.84

$$R_p \equiv \frac{d\sigma/dt(\gamma p \to K^+\Sigma^o)}{d\sigma/dt(\gamma p \to K^+\Lambda)} \qquad R_\Sigma \equiv \frac{d\sigma/dt(\gamma D \to K^+(\Sigma^o,\Sigma^-)N_s}{d\sigma/dt(\gamma p \to K^+\Sigma^o)}$$

FIGURE CAPTIONS

1. Schematic of the photon beam line and experimental layout. The pair spectrometer was used during studies of the beam spectrum and polarization. The numbered elements in the beam line before the target are:

   1) Toroid,
   2) Radiator,
   3) Cerenkov Position Monitor,
   4) Electron Beam Dump Magnets,
   5) Collimator
   6) Graphite Polarizer,
   7) Sweep Magnet,
   8) Graphite Analyzer
   9) Collimators, and
   10) Sweep Magnet

2. a) Measured attenuation function, A(k), of the beam. The solid curve is a fit to the data. See Ref. 15 for details.
   b) Photon beam energy spectrum obtained by multiplying the bremsstrahlung spectrum for a 16.05 GeV electron beam times the fit to A(k).

3. Plan and elevation views of the SLAC 20-GeV/c spectrometer. The magnet arrangement is shown at the bottom of the figure with the symbols B, Q and S representing dipole, quadrupole, and sextupole magnets, respectively.

4. Calculated trajectories through the spectrometer for selected initial values of horizontal and vertical angles (θ and ϕ), horizontal position (x), and momentum deviation (δ).

5. Detector arrangement in the spectrometer hut.

6. Polar angle plot of the cross section versus β, the angle between the electric vector and the production plane, for a process with $\Sigma=1$. The spectrometer averages over a range in angle Φ.
7. Spectrometer acceptance for the 0.3^{o} point. Counts with a polar angle greater than 9.4 mrad are not used. The azimuthal angle bins, after folding about the horizontal midplane of the spectrometer, are each 15^{o} wide. The horizontal acceptance is flat within the aperture used and the vertical acceptance is bell-shaped with half-maximum points indicated by "H" in the figure.

8. Typical a) cross section and b) asymmetry momentum distributions for pion photoproduction. The lines are fits described in the text. The contributions of single pion and $\pi\Delta$ photoproduction to the cross section are shown (n_s and N_s mean spectator neutron and nucleon respectively).

9. Dalitz plot boundary for $\gamma p \to \pi^+\pi^- p$. The overlap between the ρ and Δ bands occurs outside the boundary.

10. The non-resonant cross section for $\gamma p \to \pi^+\pi^- p$. The line is a parametrization used in estimating background contributions from non-resonant pion production. The data are from Ref. 30.

11. The ratio of the cross sections for non-resonant to $\pi\Delta$ production in the momentum region used to determine the $\pi\Delta$ cross section and asymmetry. This ratio is evaluated two ways; by assuming the events are distributed according to phase space and by assuming they are distributed according to the results of Moffeit et al. (Ref. 31).

12. a) Model for pion photoproduction via ρ exchange. Making the assumptions discussed in the text, the cross section in this model is proportional to the total photoproduction cross section at low energy.

    b) The smoothed data from von Holtey (Ref. 33) shows a low mass enhancement in the π^+ total cross section.

13. Yields for pion and kaon photoproduction. The step for single pion photoproduction is clearly steeper than the combined $K^+\Lambda$, $K^+\Sigma^o$ step. Any momentum shift and the momentum resolution were determined from the pion data. Thresholds for various reactions are indicated by the arrows.

14. Comparison of our measurements of the π^-/π^+ ratio made with unpolarized photons and those of Boyarski et al. (Ref. 36).

15. a) Cross section ratio for single π^+ photoproduction from hydrogen and deuterium.

    b) Comparison of the single π^+ photoproduction asymmetry from hydrogen and deuterium.

16. The polarized photon asymmetry for single π^+ photoproduction. In addition to our measurements we show the results of Refs. 7-10. The curve is the asymmetry in the electric Born model.

17. The polarized photon asymmetry for single π^- photoproduction. Also shown are the lower energy results of Refs. 11 and 12 and the asymmetry in the electric Born model.

18. The effective Regge trajectories for a) perpendicular and b) parallel polarizations. α_{eff} for perpendicular polarization is roughly consistent with zero while for parallel polarization it is consistent with either of the two possible Regge trajectories shown.

19. The π^-/π^+ ratio for single pion photoproduction with polarized and unpolarized photons. Also included in the figure are the lower energy results of Refs. 11 and 12.

20. The polarized photon asymmetries for $\pi\Delta$ photoproduction. The $\pi^+\Delta^o$ data are compared with the lower energy data of Ref. 10 and with the minimal gauge invariant calculation of Ref. 49. This calculation is also compared with the $\pi^-\Delta^{++}$ data.

21. Cross sections for $\pi\Delta$ photoproduction with polarized and unpolarized photons.

22. The π^-/π^+ cross section ratio for $\pi\Delta$ photoproduction with polarized and unpolarized photons.

23. The deuterium-to-hydrogen cross section ratios for unpolarized photons compared with those of Boyarski et al. (Ref. 43). The dashed lines show the values expected in the absence of I=2 exchanges.

24. The deuterium-to-hydrogen cross section ratios for polarized photons.

25. The small $|t|$ cross sections for a) single π^+ and b) $\pi^-\Delta^{++}$ photoproduction from hydrogen.

26. Vector dominance comparison of single π photoproduction and $\pi^-p \to \rho^o n$ (data from Ref. 52) for a) natural parity exchange (perpendicular photons) and b) unnatural parity exchange (parallel photons).

27. The polarized photon asymmetry from single pion photoproduction compared with that for $\pi^-p \to \rho^o n$. The π^- data is from Ref. 52.

28. Comparison of the $\pi\Delta$ photoproduction cross section with that for $\pi^+p \to \rho^o\Delta^{++}$ (Ref. 58).

29. The $\pi^+p \to \rho^o\Delta^{++}$ (Ref. 58) asymmetry compared with the $\pi\Delta$ photoproduction asymmetry.

30. The polarized photon asymmetry for single K^+ photoproduction from a) hydrogen and b) deuterium.

31. The recoil Λ polarization measurements of Vogel et al. (Ref. 66) and the polarized photon asymmetry measurement for $\gamma p \to K^+\Lambda$.

32. The δ-θ plane. Lines of constant missing-mass-squared = m_p^2 are shown for two values of the central spectrometer angle.

33. The angles used in the ρ^o decay parametrization.

34. The Σ^o/Λ ratio for single K^+ photoproduction from hydrogen, compared with the results of Ref. 60, and the deuterium-to-hydrogen ratio for Σ photoproduction compared with the results of Ref. 63.

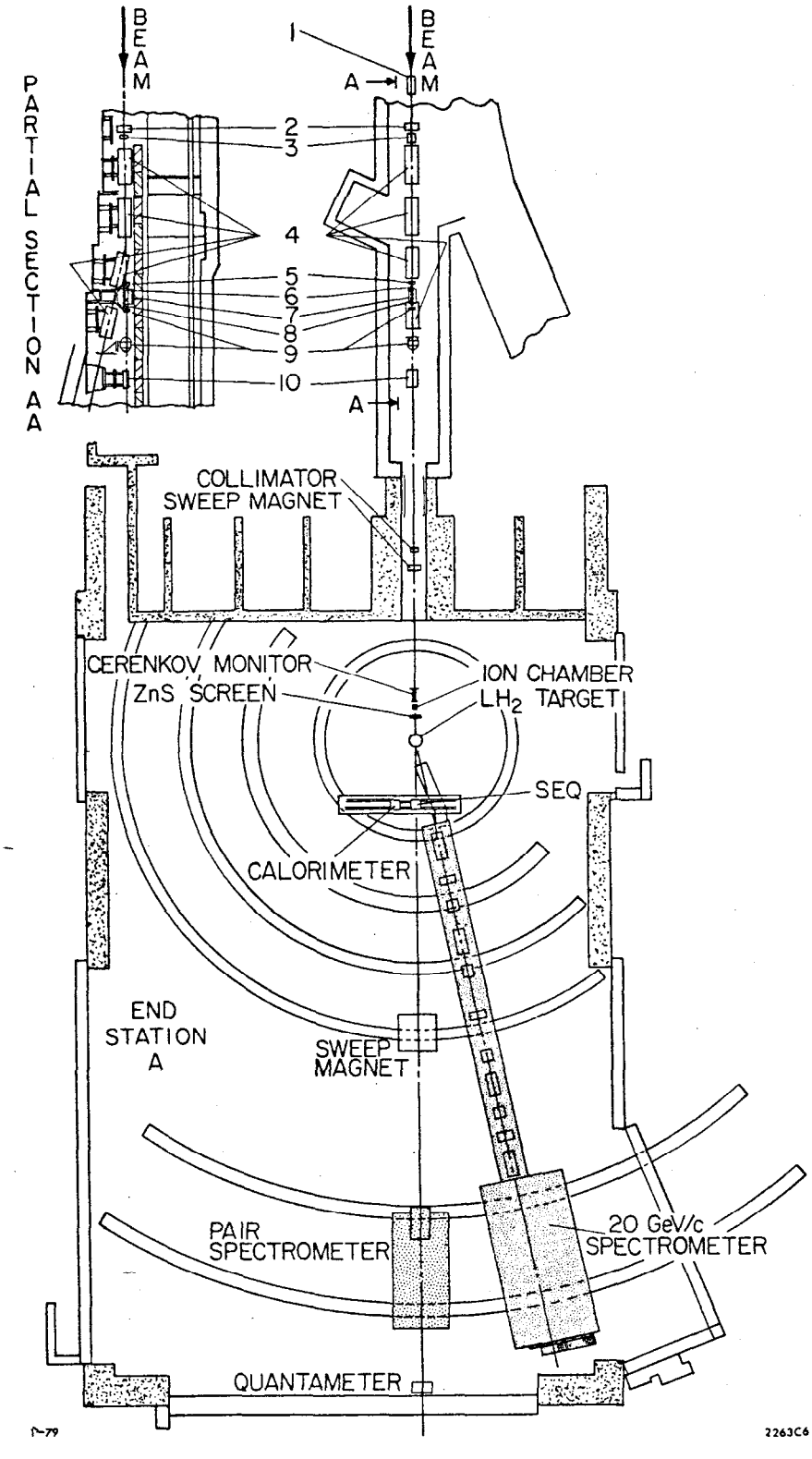
BEAM
BEAM
1
A
A
PARTIAL SECTION AA
2
3
4
5
6
7
8
9
10
COLLIMATOR
SWEEP MAGNET
CERENKOV MONITOR
ZnS SCREEN
ION CHAMBER
LH2 TARGET
SEQ
CALORIMETER
END
STATION
A
SWEEP
MAGNET
PAIR
SPECTROMETER
20 GeV/c
SPECTROMETER
QUANTAMETER
2263C6

Fig. 1

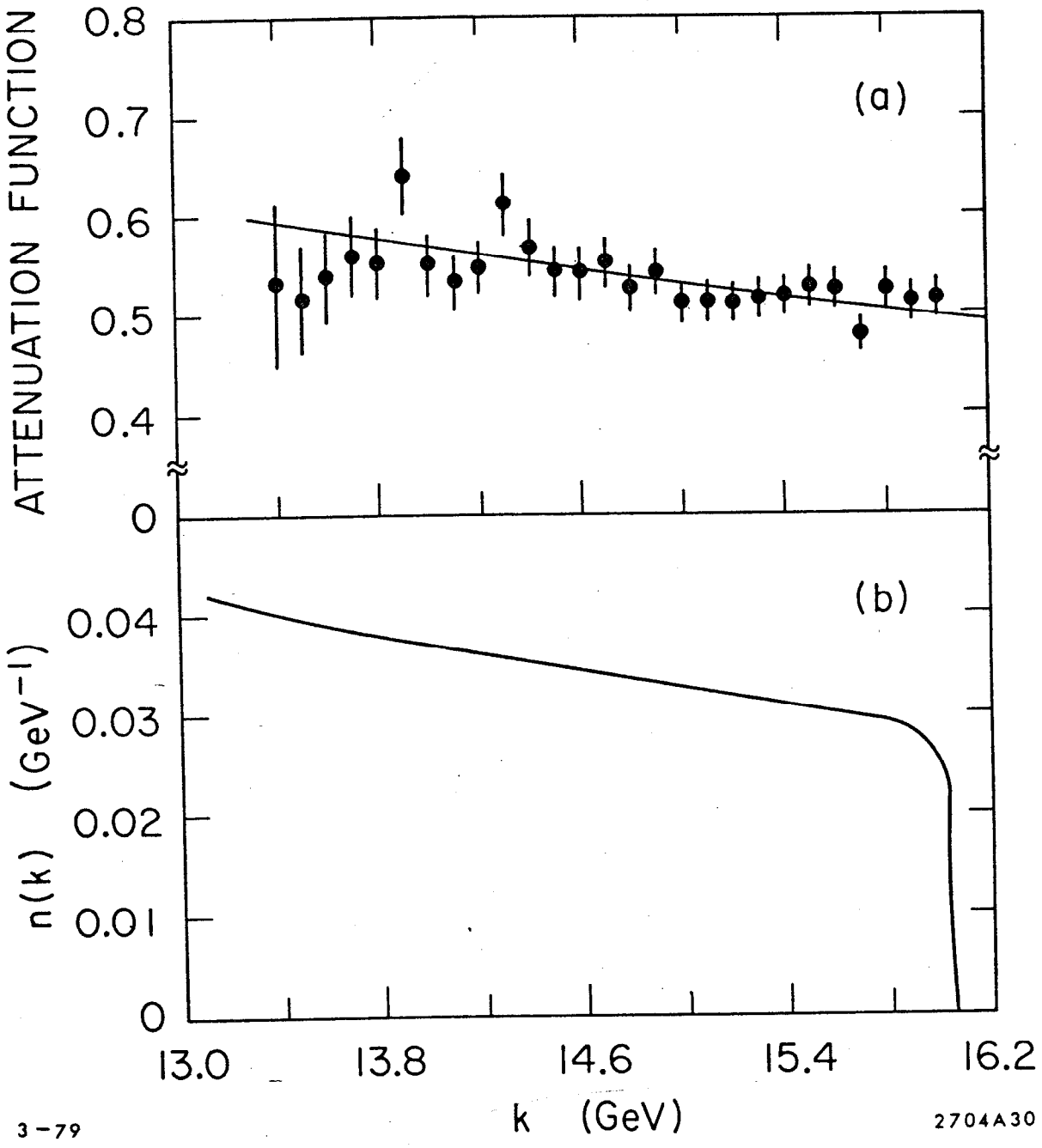
ATTENUATION FUNCTION
0.8
0.7
0.6
0.5
0.4
0
(a)
(b)
n(k) (GeV⁻¹)
0.04
0.03
0.02
0.01
0
13.0
13.8
14.6
15.4
16.2
k (GeV)
3-79
2704A30

Fig. 2

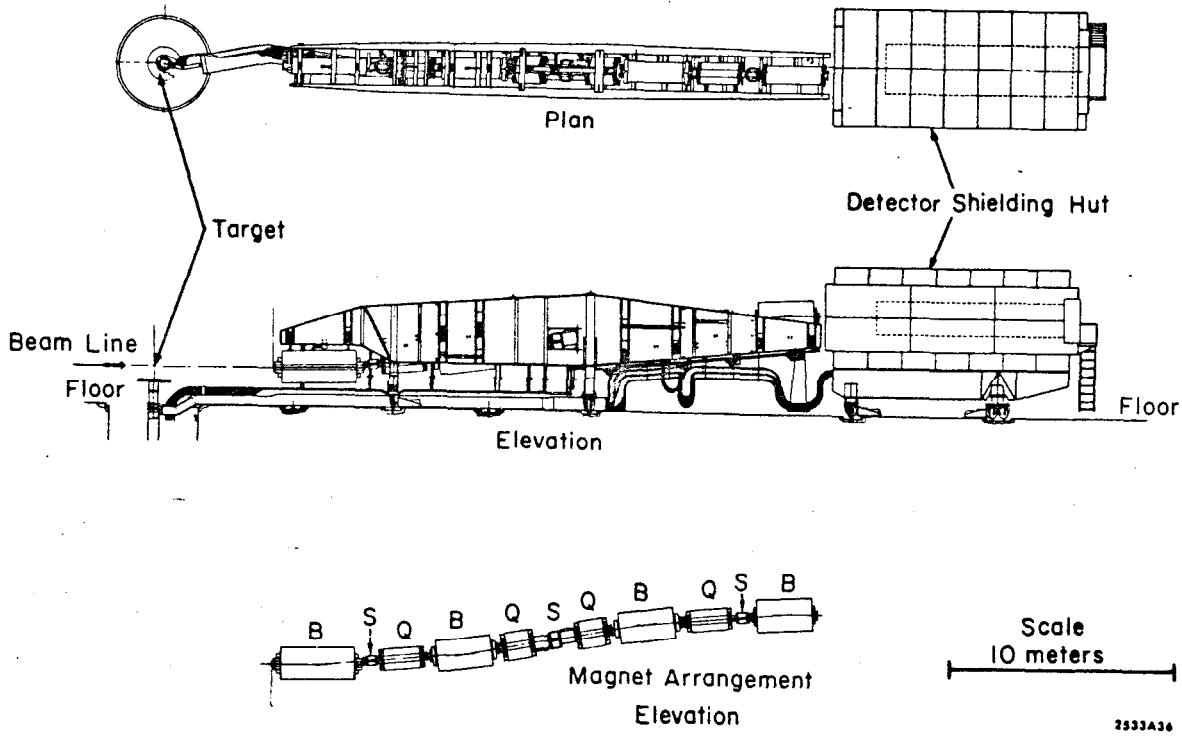
Plan
Target
Detector Shielding Hut
Beam Line
Floor
Floor
Elevation
B S Q B Q S Q B Q S B
Magnet Arrangement
Elevation
Scale
10 meters
2533A36

Fig. 3

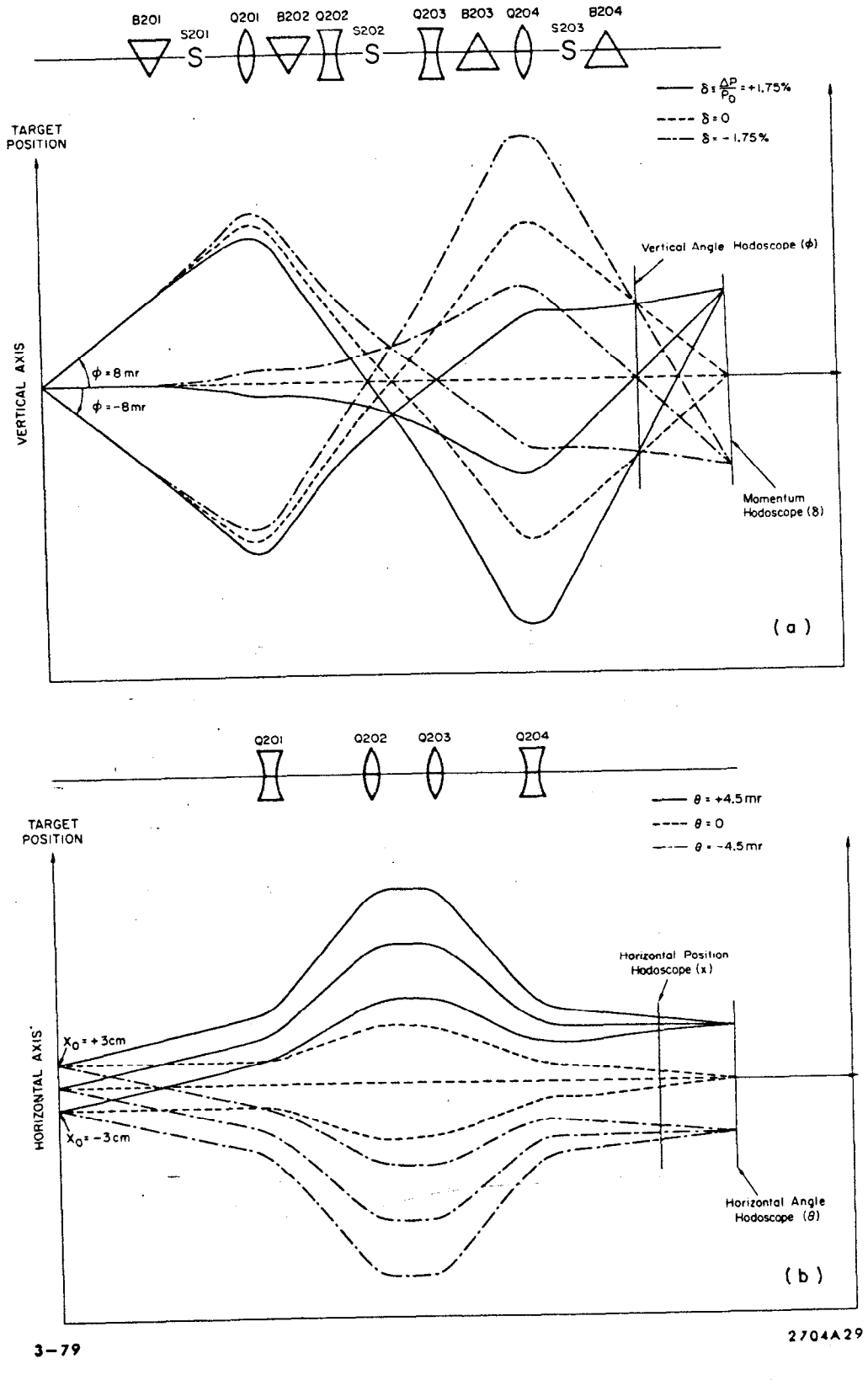
B201
S201
Q201
B202
Q202
S202
Q203
B203
Q204
S203
B204
δ = ΔP/P0 = +1.75%
δ = 0
δ = −1.75%
TARGET POSITION
VERTICAL AXIS
Vertical Angle Hodoscope (φ)
φ = 8 mr
φ = −8 mr
Momentum Hodoscope (δ)
(a)
Q201
Q202
Q203
Q204
θ = +4.5 mr
θ = 0
θ = −4.5 mr
TARGET POSITION
HORIZONTAL AXIS
Horizontal Position Hodoscope (x)
X0 = +3cm
X0 = −3cm
Horizontal Angle Hodoscope (θ)
(b)
3-79
2704A29

Fig. 4

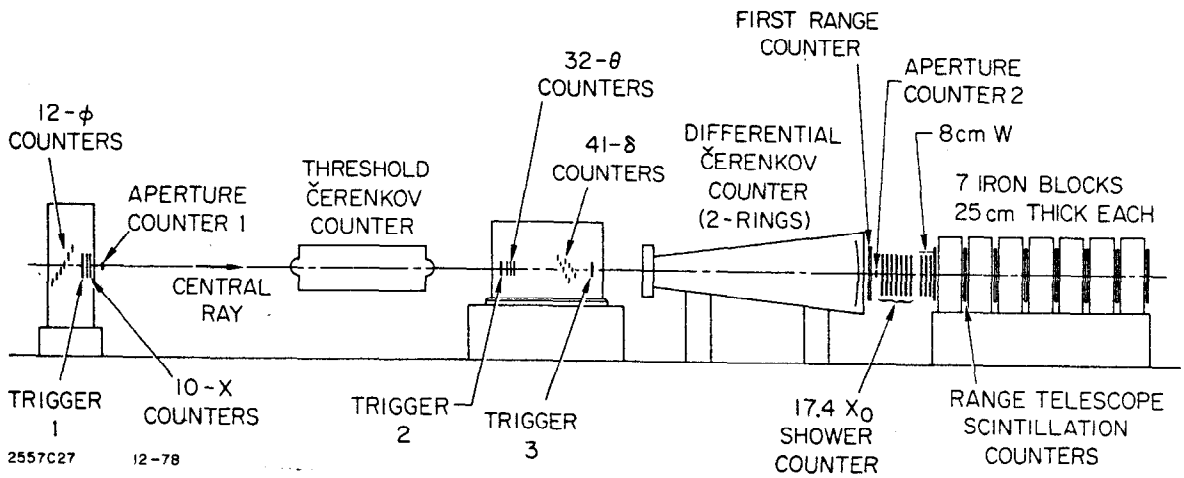
12-φ
COUNTERS
APERTURE
COUNTER 1
THRESHOLD
ČERENKOV
COUNTER
32-θ
COUNTERS
41-δ
COUNTERS
FIRST RANGE
COUNTER
APERTURE
COUNTER 2
DIFFERENTIAL
ČERENKOV
COUNTER
(2-RINGS)
8cm W
7 IRON BLOCKS
25 cm THICK EACH
CENTRAL
RAY
TRIGGER
1
10-X
COUNTERS
TRIGGER
2
TRIGGER
3
17.4 X0
SHOWER
COUNTER
RANGE TELESCOPE
SCINTILLATION
COUNTERS
2557C27
12-78

Fig. 5

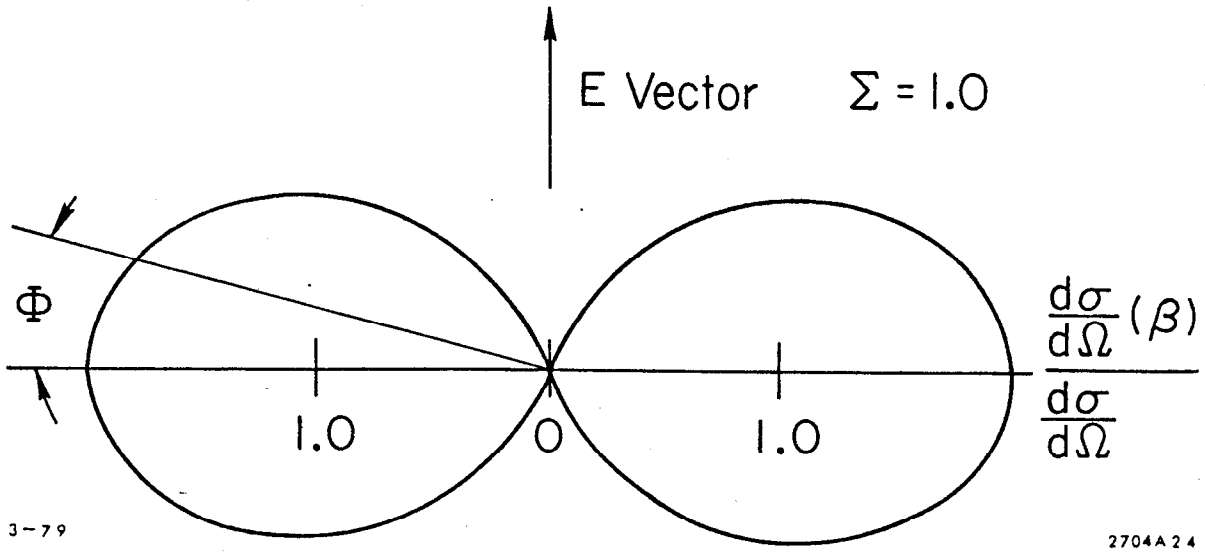

Fig. 6

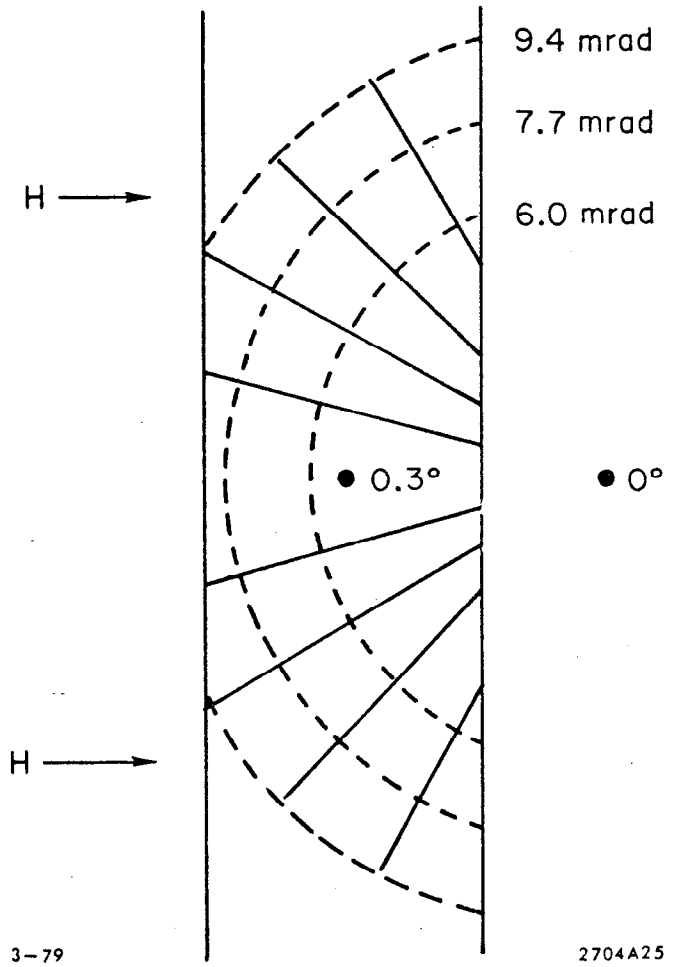

Fig. 7

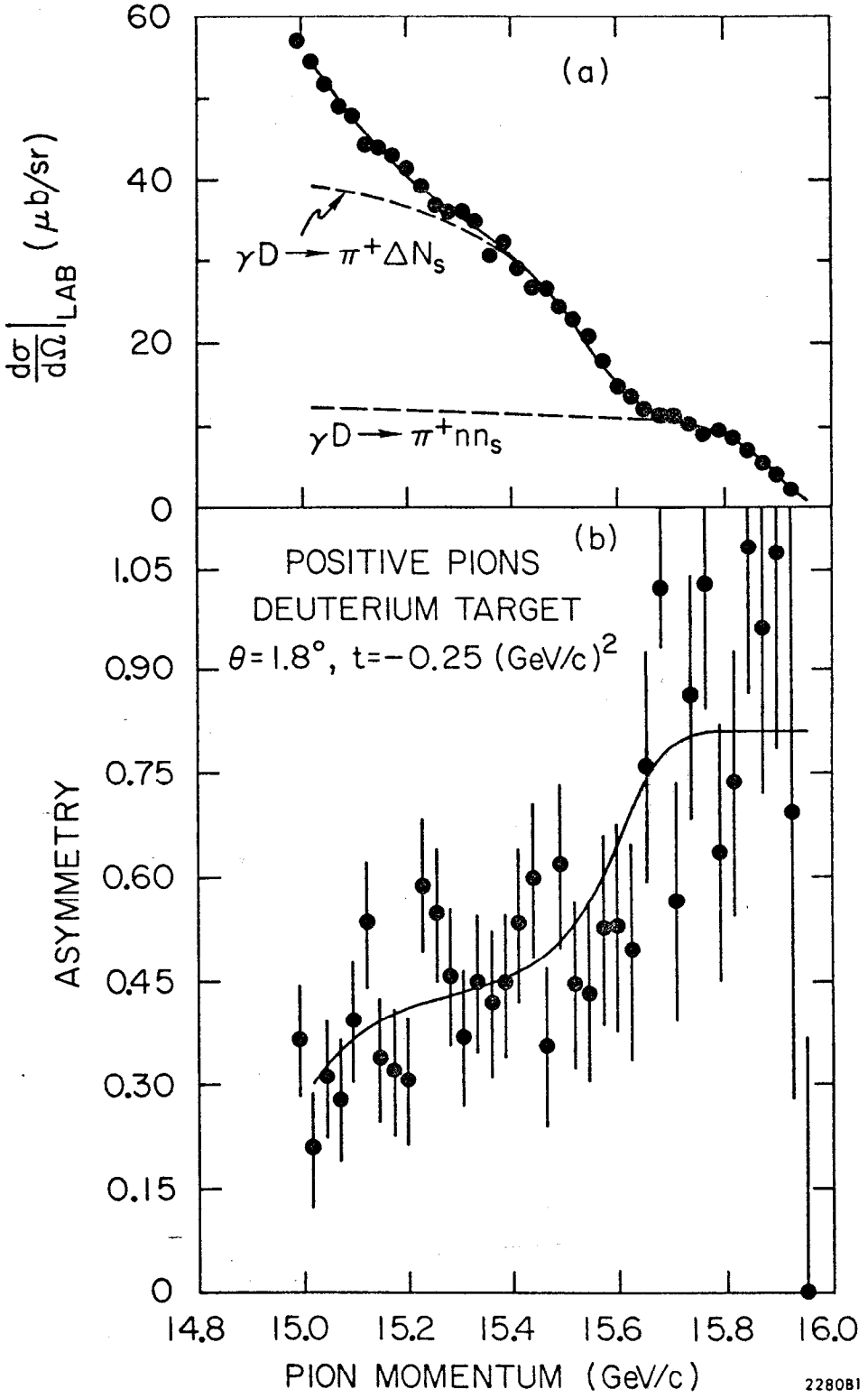
60
40
20
0
(a)
$\frac{d\sigma}{d\Omega}\Big|_{LAB}$ (μb/sr)
$\gamma D \rightarrow \pi^+ \Delta N_s$
$\gamma D \rightarrow \pi^+ nn_s$
(b)
POSITIVE PIONS
DEUTERIUM TARGET
$\theta = 1.8°$, $t = -0.25$ (GeV/c)^2
1.05
0.90
0.75
0.60
0.45
0.30
0.15
0
ASYMMETRY
14.8
15.0
15.2
15.4
15.6
15.8
16.0
PION MOMENTUM (GeV/c)
2280B1

Fig. 8

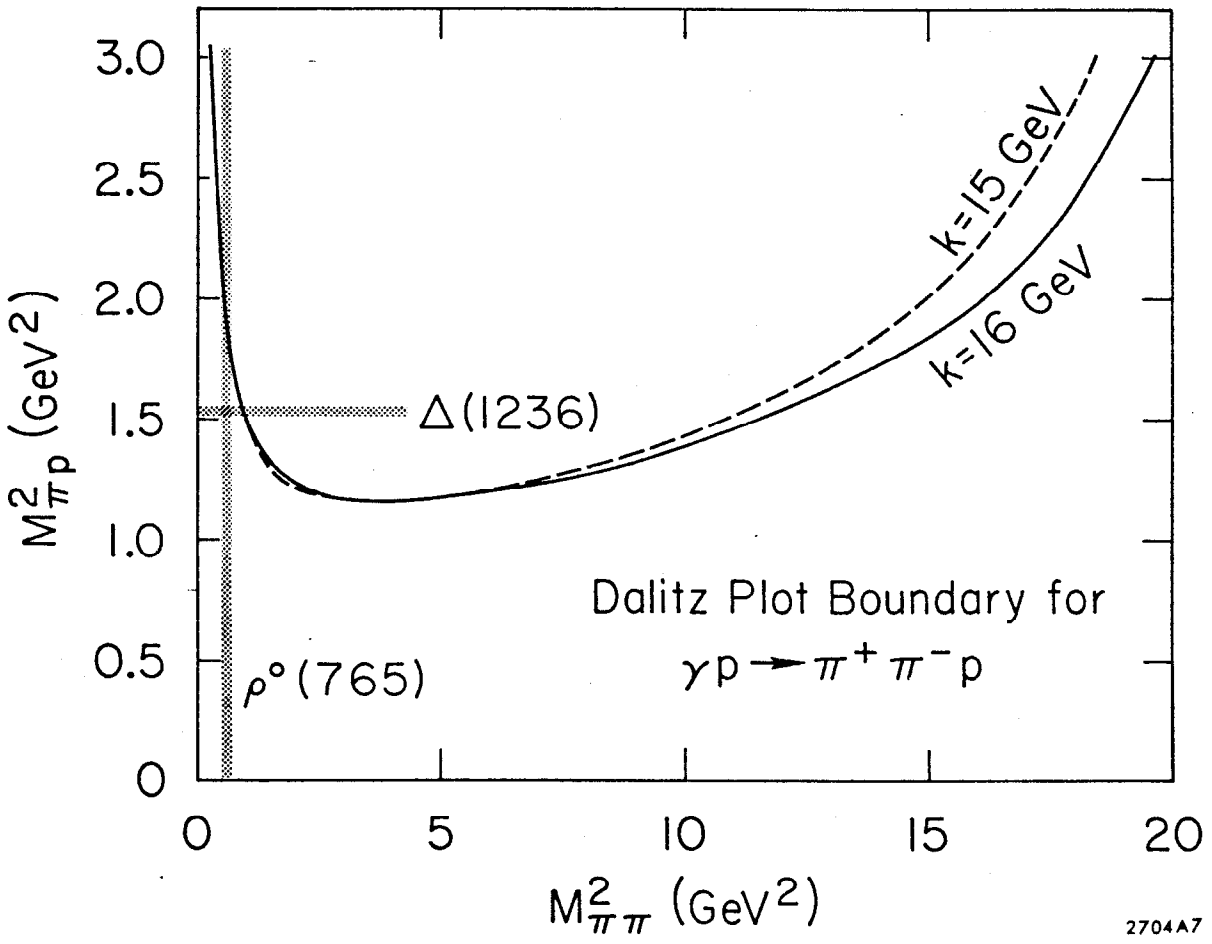
3.0
2.5
2.0
1.5
1.0
0.5
0
0
5
10
15
20
$M^2_{\pi p}$ (GeV^2)
$M^2_{\pi\pi}$ (GeV^2)
k=15 GeV
k=16 GeV
Δ(1236)
ρ°(765)
Dalitz Plot Boundary for
γp → π⁺π⁻p
2704A7

Fig. 9

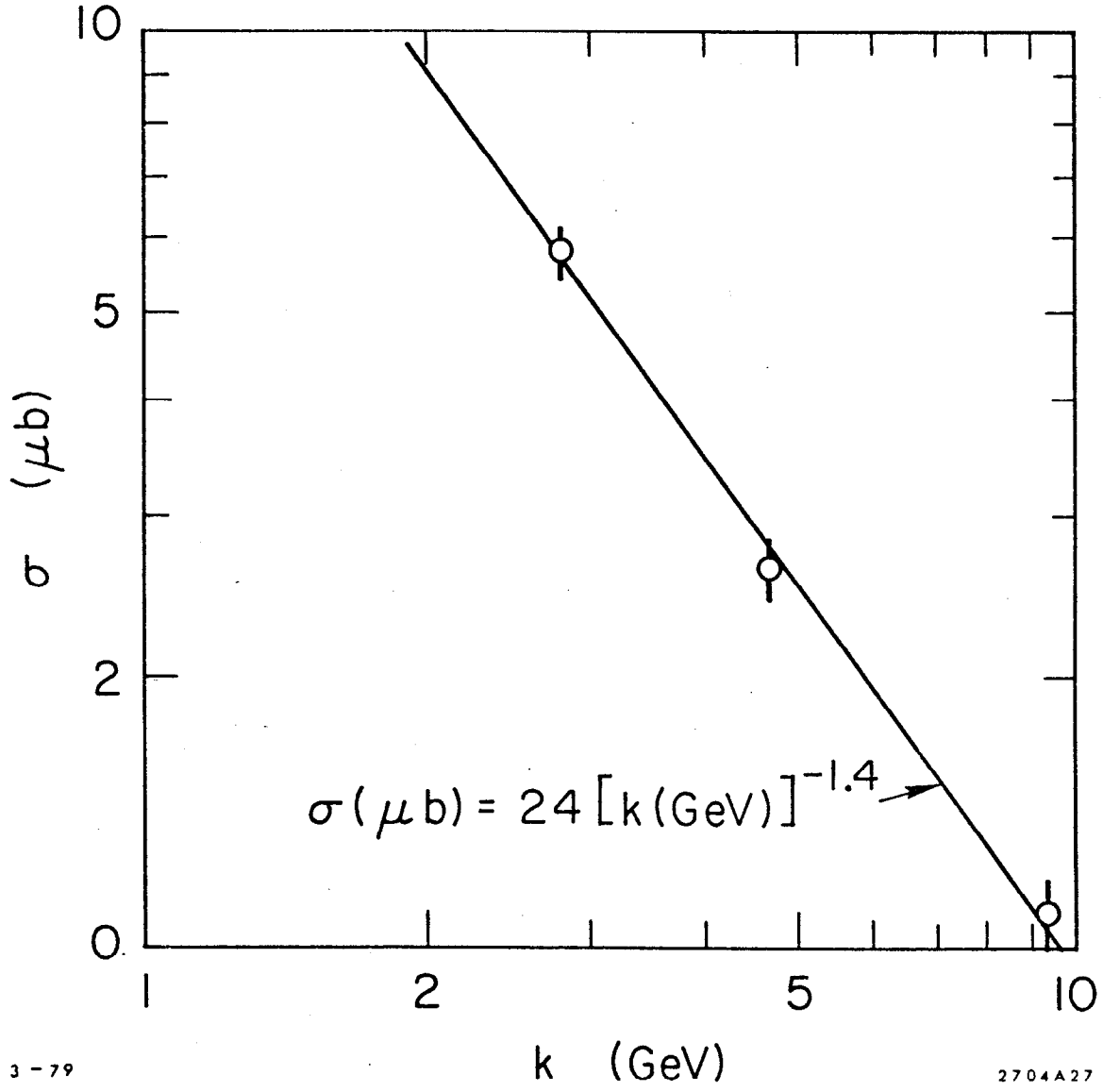

Fig. 10

— Events distributed according to phase space

-- Events distributed according to the data of Moffeit et al., ref 31.

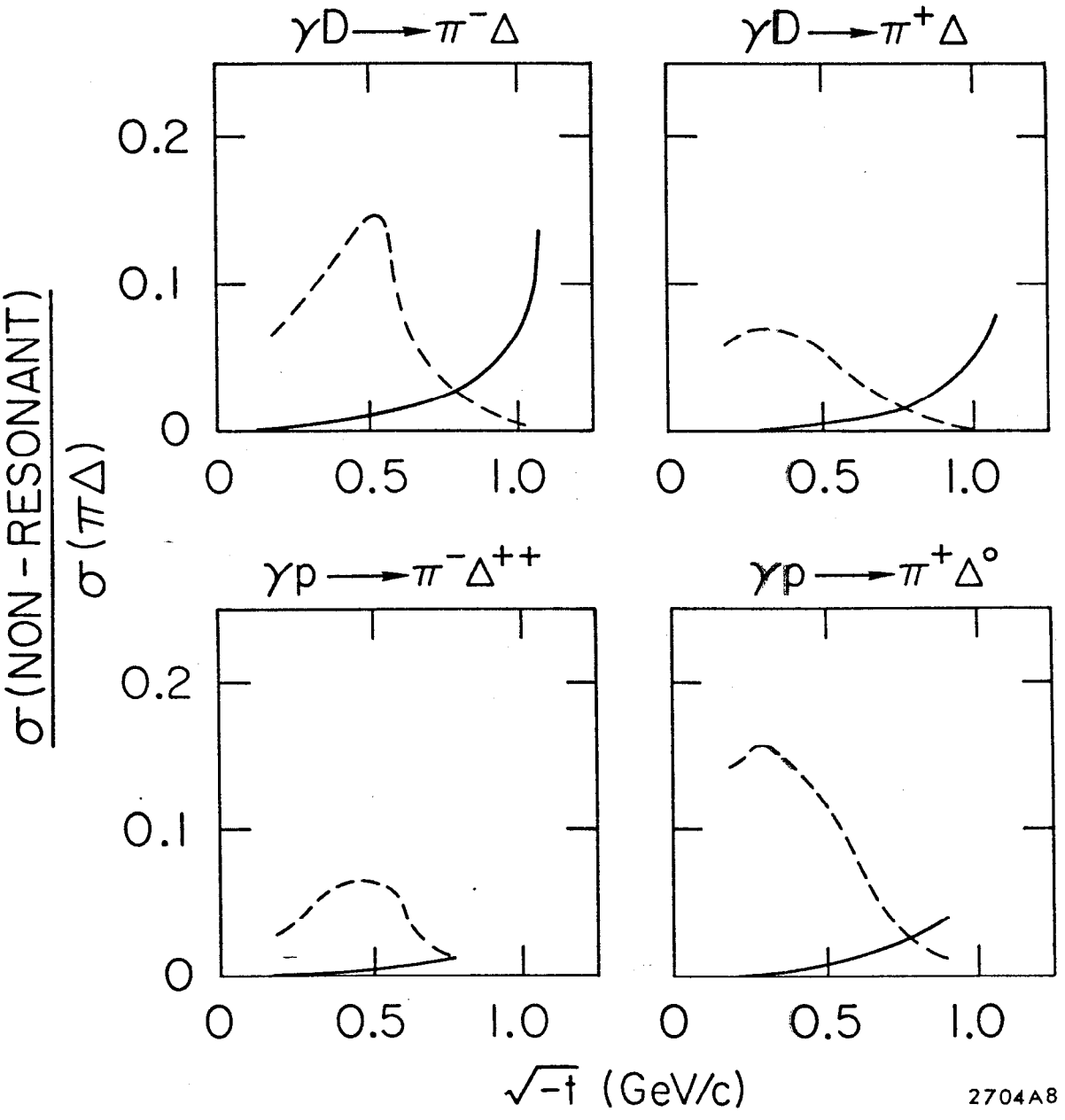

Fig. 11

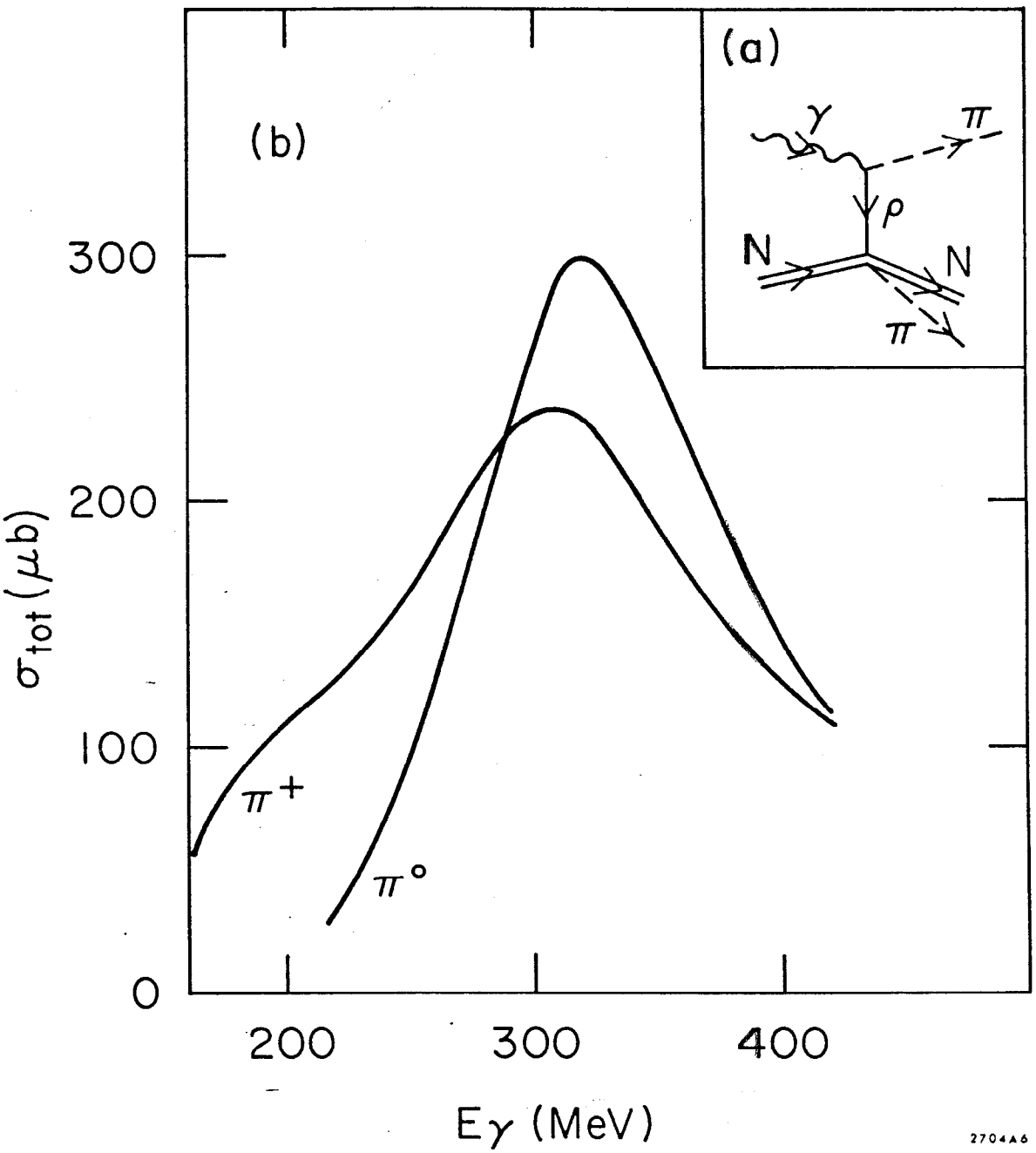

Fig. 12

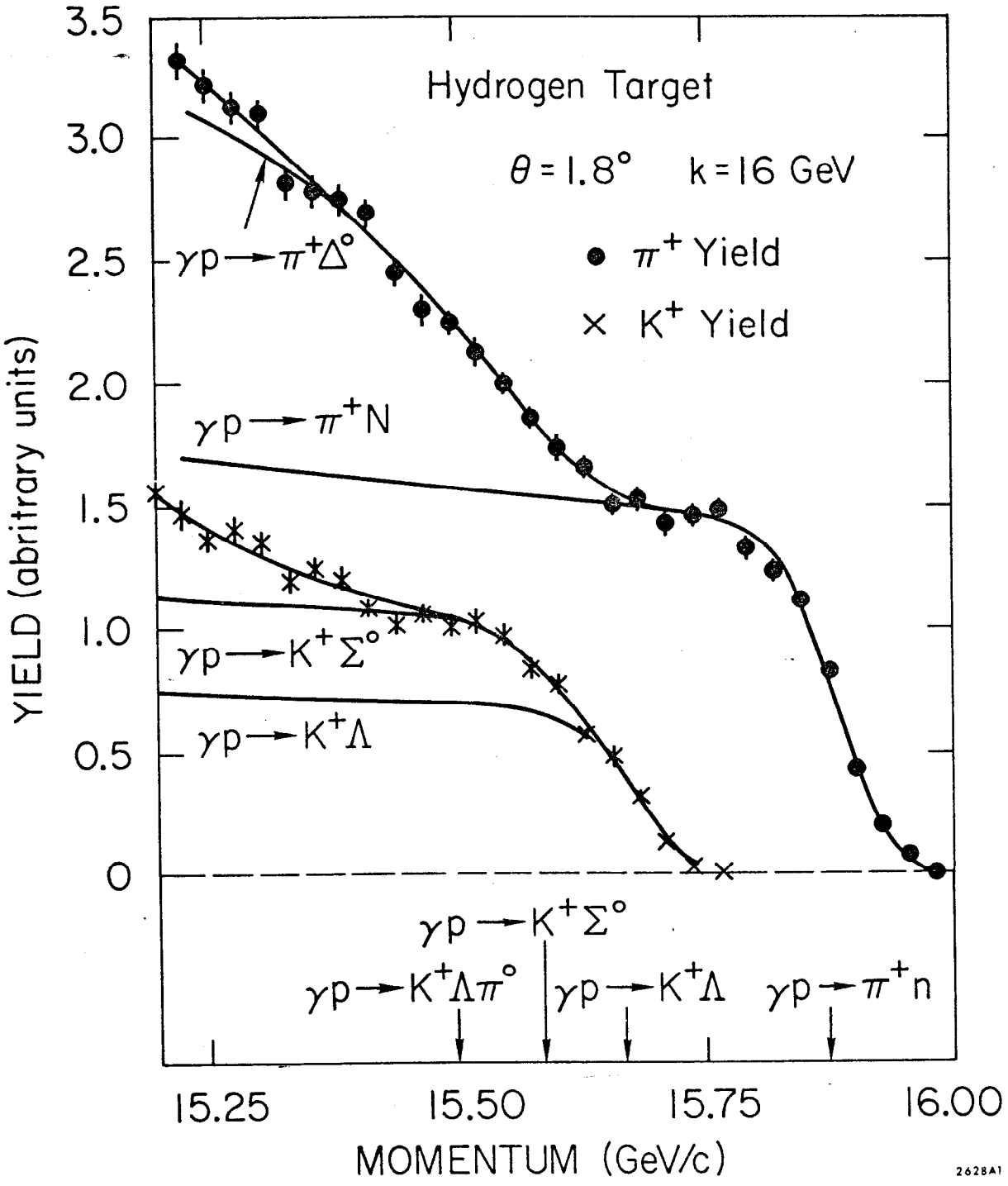
Hydrogen Target
θ = 1.8° k = 16 GeV
π+ Yield
K+ Yield
γp → π+Δ°
γp → π+N
γp → K+Σ°
γp → K+Λ
γp → K+Σ°
γp → K+Λπ°
γp → K+Λ
γp → π+n
YIELD (abritrary units)
MOMENTUM (GeV/c)
3.5
3.0
2.5
2.0
1.5
1.0
0.5
0
15.25
15.50
15.75
16.00
2628A1

Fig. 13

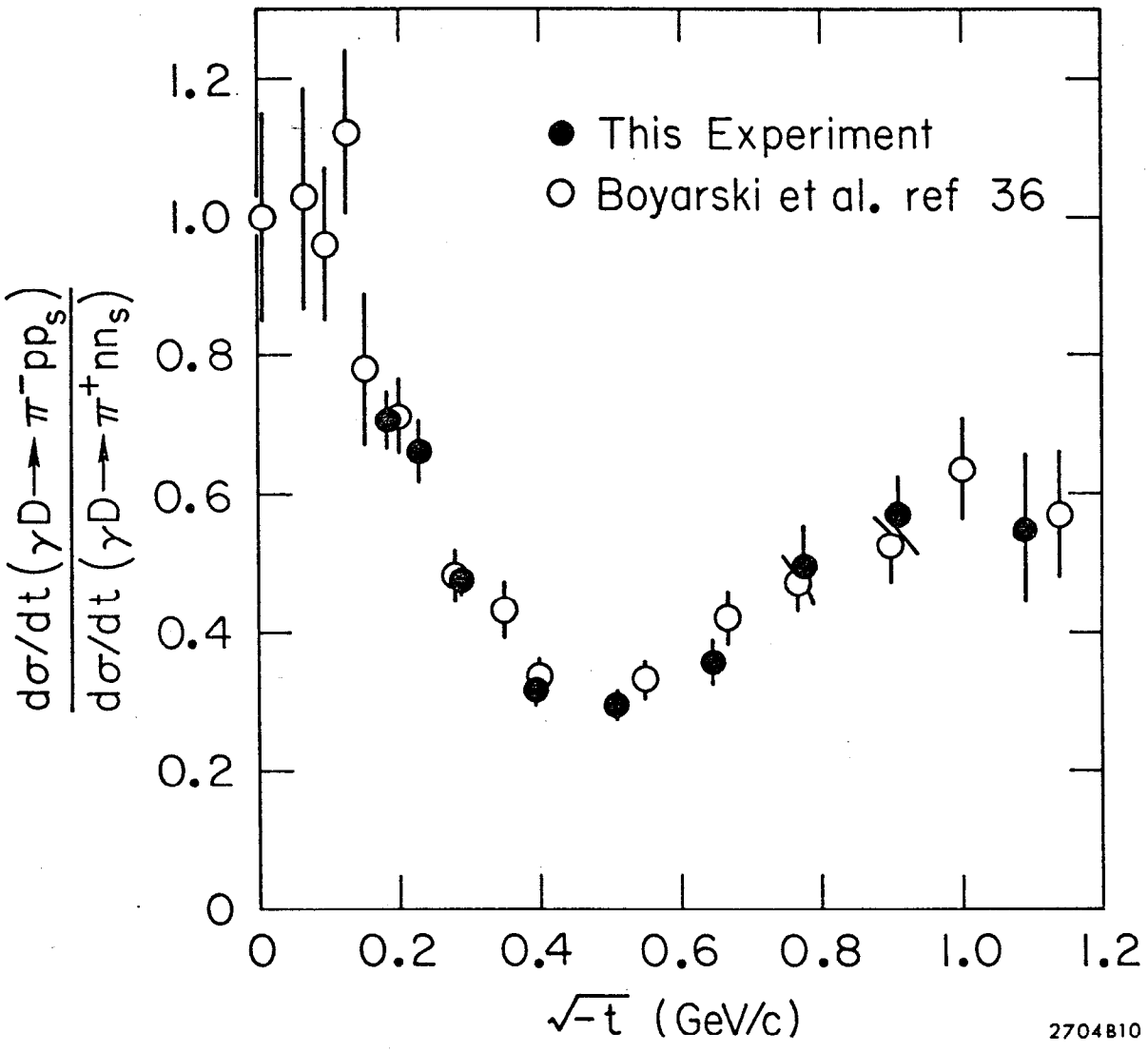
This Experiment
Boyarski et al. ref 36
$\frac{d\sigma/dt(\gamma D \to \pi^- pp_s)}{d\sigma/dt(\gamma D \to \pi^+ nn_s)}$
$\sqrt{-t}$ (GeV/c)
0
0.2
0.4
0.6
0.8
1.0
1.2
2704B10

Fig. 14

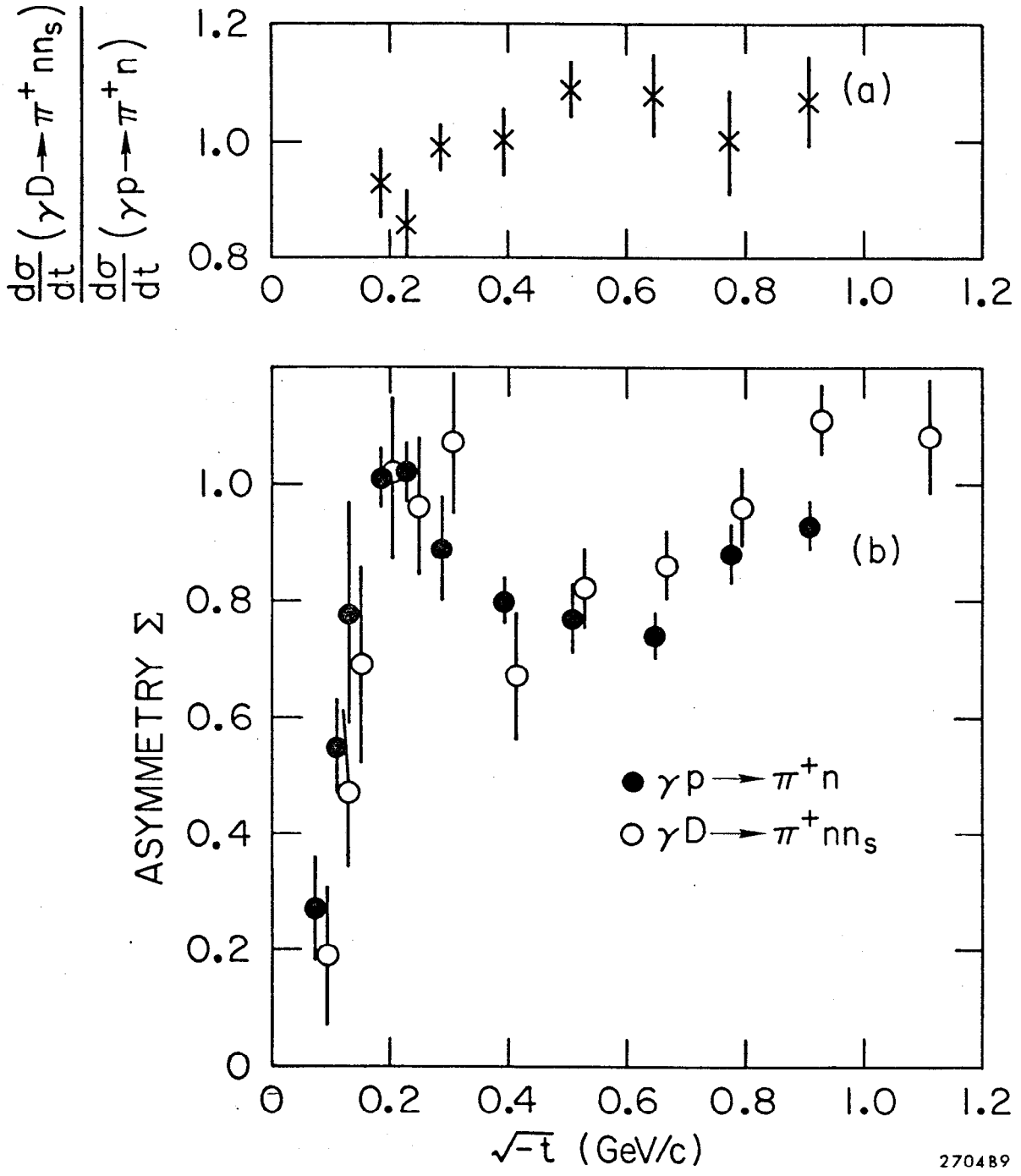
$\frac{d\sigma}{dt}(\gamma D \to \pi^+ nn_s) \Big/ \frac{d\sigma}{dt}(\gamma p \to \pi^+ n)$
1.2
1.0
0.8
0
0.2
0.4
0.6
0.8
1.0
1.2
(a)
ASYMMETRY Σ
(b)
● $\gamma p \to \pi^+ n$
○ $\gamma D \to \pi^+ nn_s$
$\sqrt{-t}$ (GeV/c)
270489

Fig. 15

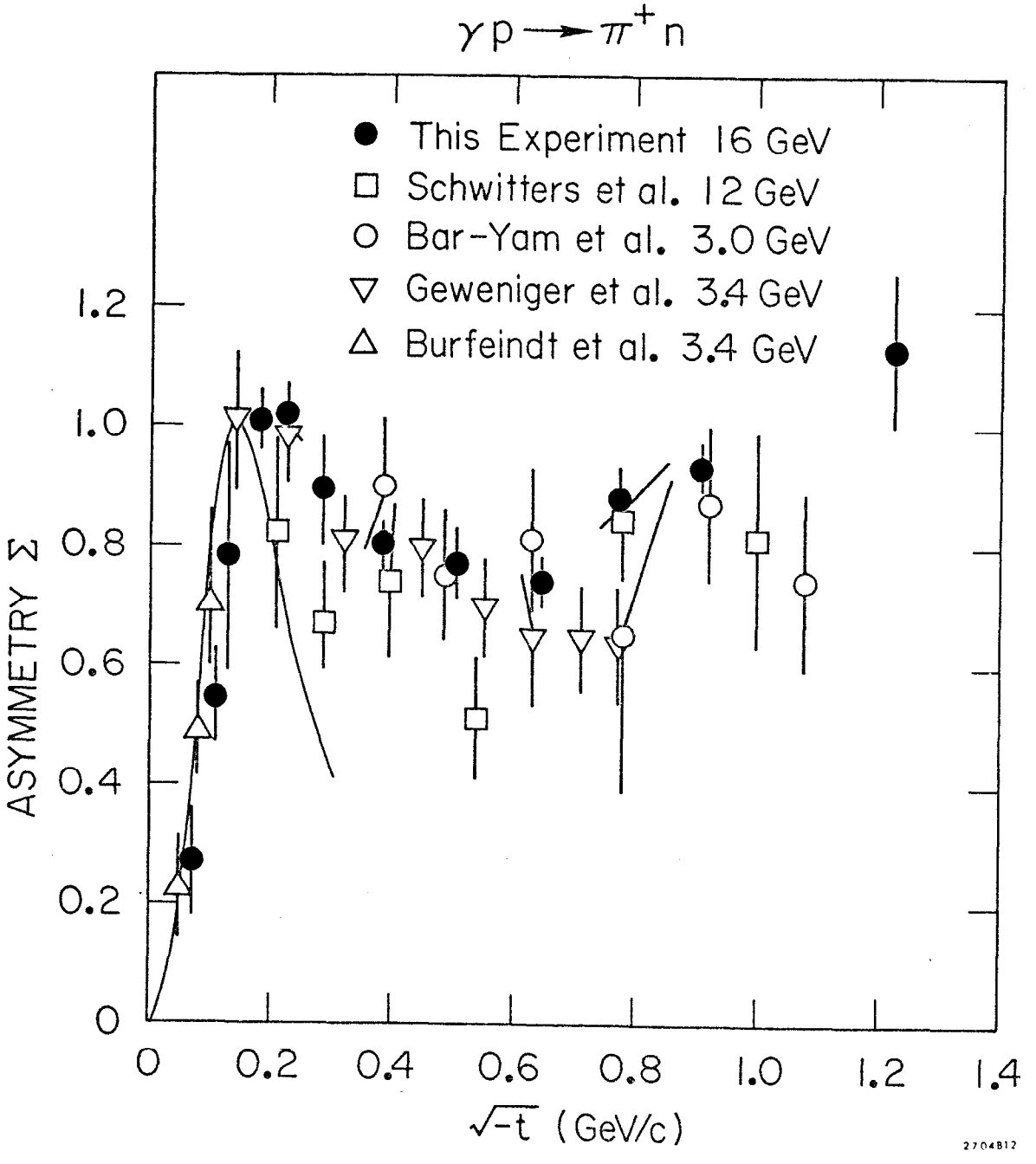
γ p → π+ n
This Experiment 16 GeV
Schwitters et al. 12 GeV
Bar-Yam et al. 3.0 GeV
Geweniger et al. 3.4 GeV
Burfeindt et al. 3.4 GeV
ASYMMETRY Σ
0
0.2
0.4
0.6
0.8
1.0
1.2
1.4
√-t (GeV/c)
2704B12

Fig. 16

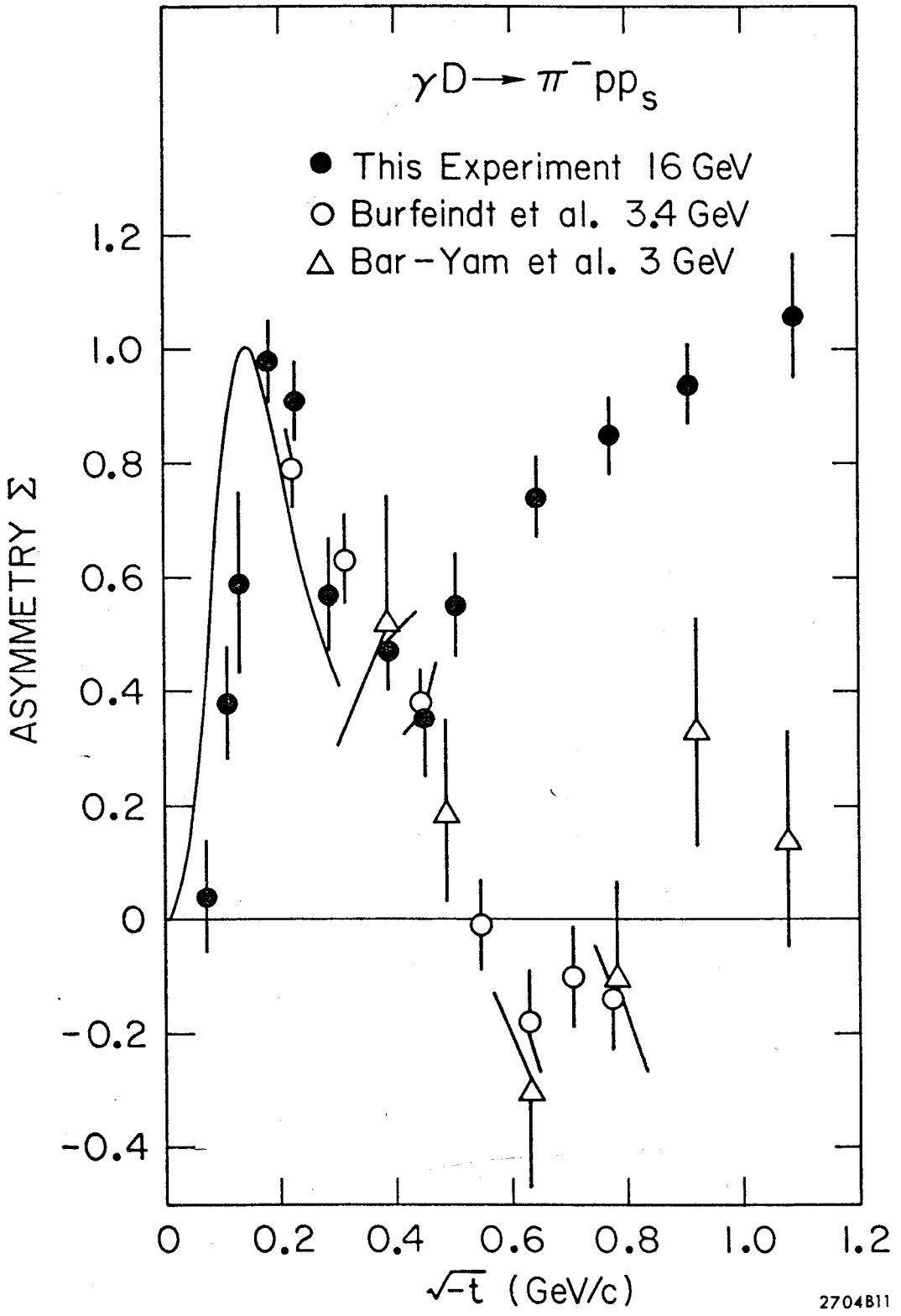
$\gamma D \rightarrow \pi^- pp_s$
This Experiment 16 GeV
Burfeindt et al. 3.4 GeV
Bar-Yam et al. 3 GeV
ASYMMETRY Σ
1.2
1.0
0.8
0.6
0.4
0.2
0
-0.2
-0.4
0
0.2
0.4
0.6
0.8
1.0
1.2
$\sqrt{-t}$ (GeV/c)
2704B11

Fig. 17

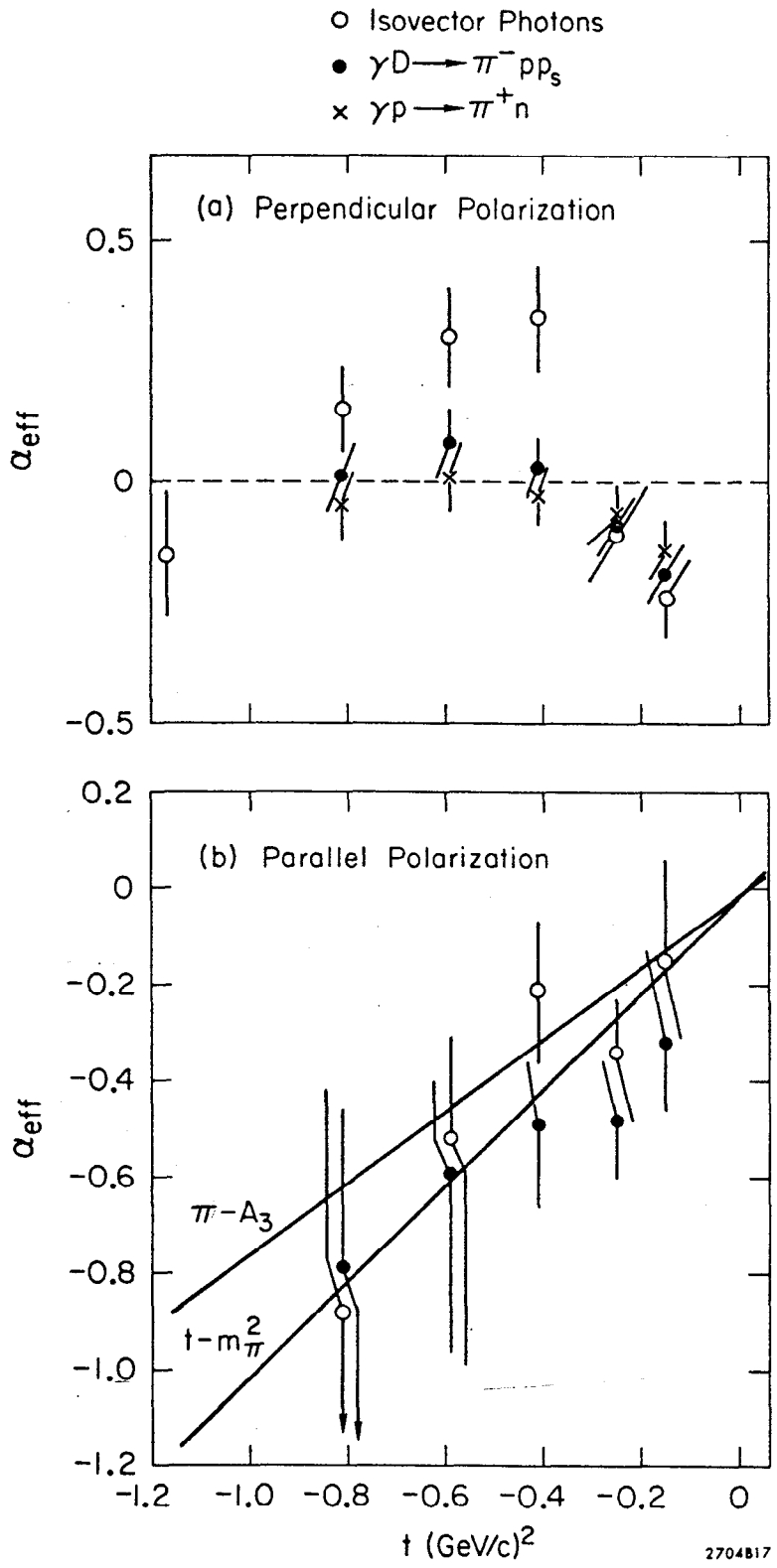
o Isovector Photons
• γD → π⁻pp_s
× γp → π⁺n
(a) Perpendicular Polarization
0.5
0
-0.5
α_eff
0.2
0
-0.2
-0.4
-0.6
-0.8
-1.0
-1.2
(b) Parallel Polarization
π-A3
t-m²π
-1.2 -1.0 -0.8 -0.6 -0.4 -0.2 0
t (GeV/c)²
2704B17

Fig. 18

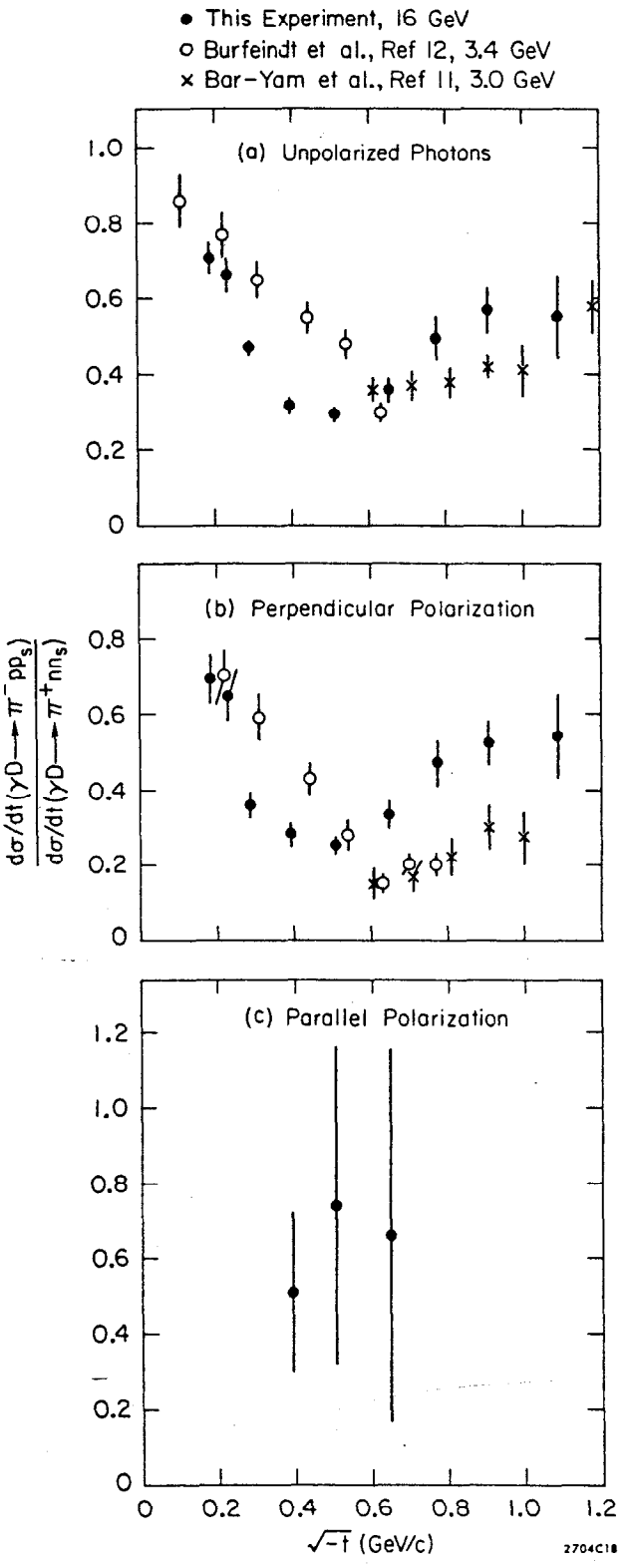
• This Experiment, 16 GeV
o Burfeindt et al., Ref 12, 3.4 GeV
× Bar-Yam et al., Ref 11, 3.0 GeV
(a) Unpolarized Photons
(b) Perpendicular Polarization
(c) Parallel Polarization
dσ/dt(γD→π⁻pp_s) / dσ/dt(γD→π⁺nn_s)
√-t (GeV/c)
2704C18

Fig. 19

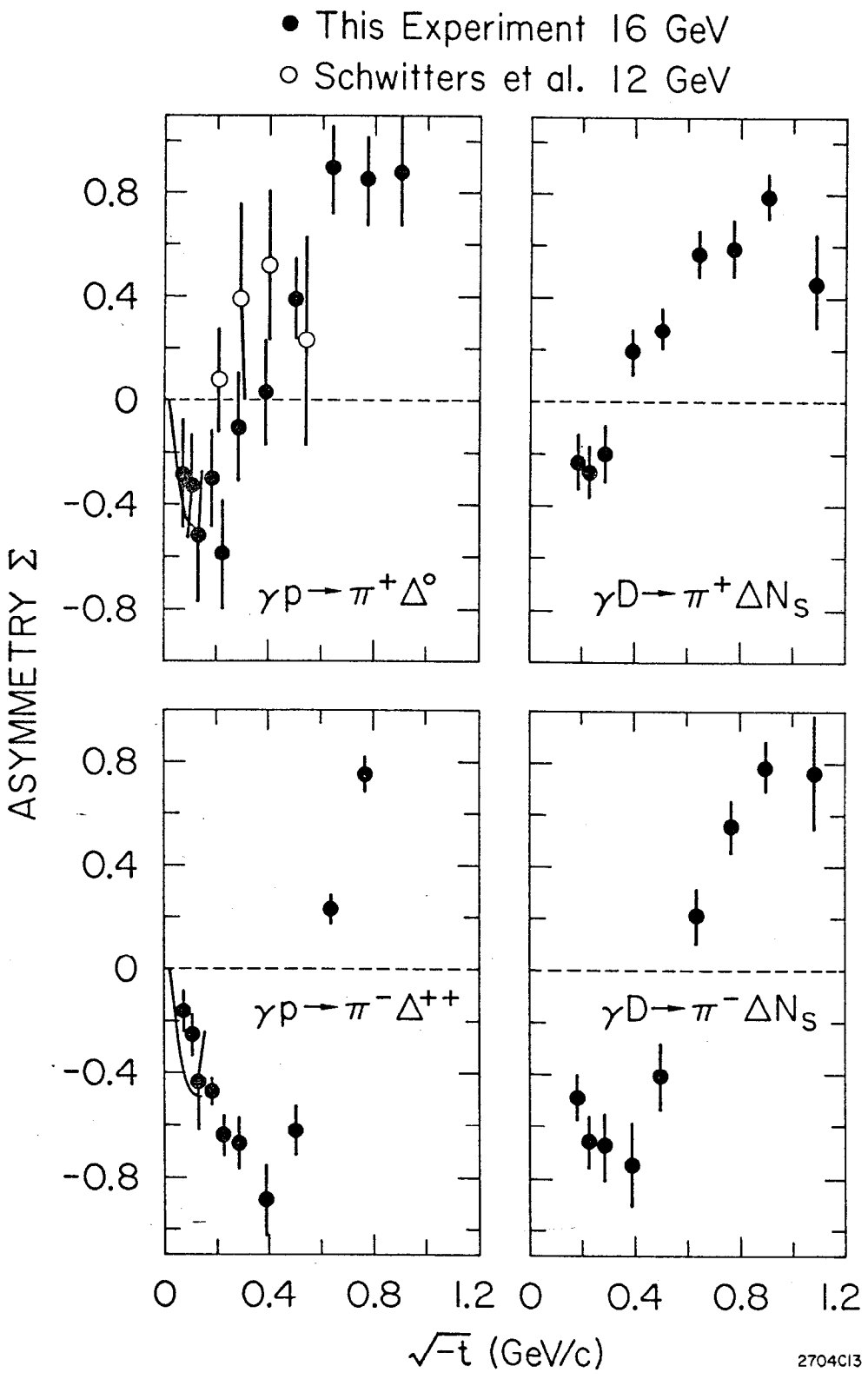
● This Experiment 16 GeV
○ Schwitters et al. 12 GeV
ASYMMETRY Σ
0.8
0.4
0
-0.4
-0.8
γp→π⁺Δ°
γD→π⁺ΔN_S
γp→π⁻Δ⁺⁺
γD→π⁻ΔN_S
0
0.4
0.8
1.2
√-t (GeV/c)
2704C13

Fig. 20

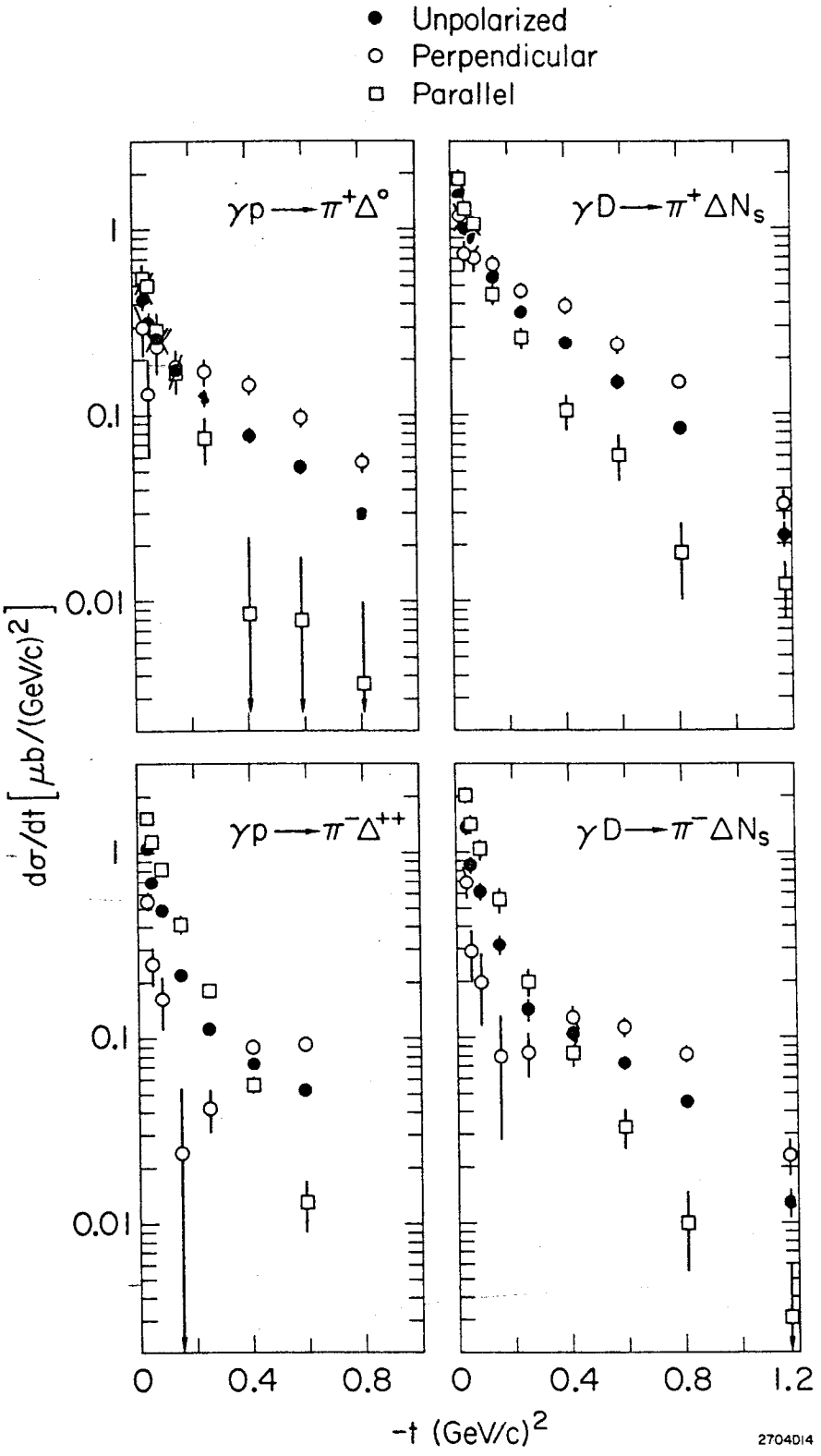
Unpolarized
Perpendicular
Parallel
γp → π⁺Δ°
γD → π⁺ΔN_s
γp → π⁻Δ⁺⁺
γD → π⁻ΔN_s
dσ/dt [μb/(GeV/c)²]
1
0.1
0.01
0
0.4
0.8
1.2
-t (GeV/c)²
2704D14

Fig. 21

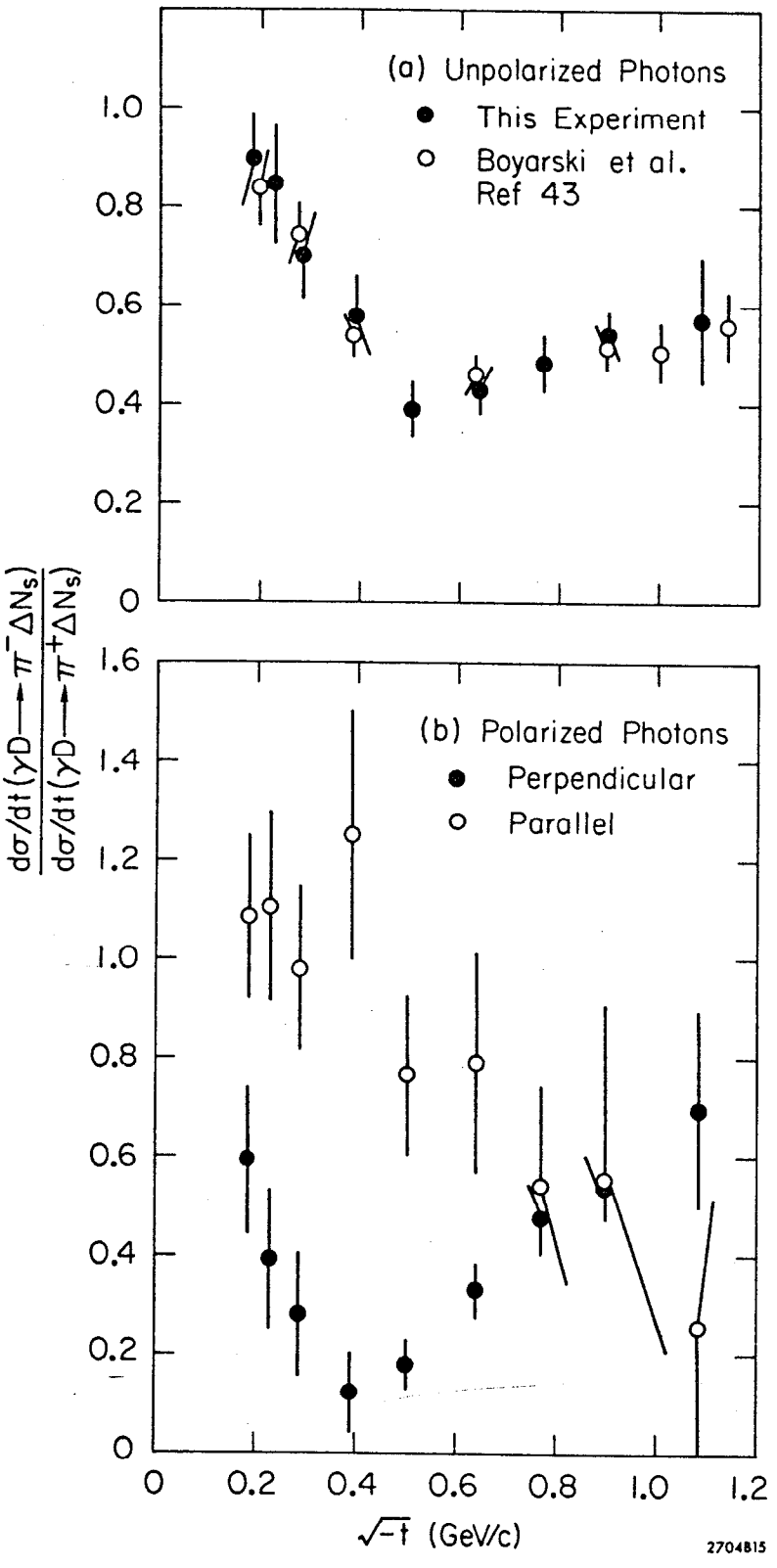
(a) Unpolarized Photons
This Experiment
Boyarski et al.
Ref 43
(b) Polarized Photons
Perpendicular
Parallel
$\frac{d\sigma/dt(\gamma D \to \pi^- \Delta N_s)}{d\sigma/dt(\gamma D \to \pi^+ \Delta N_s)}$
$\sqrt{-t}$ (GeV/c)
2704B15

Fig. 22

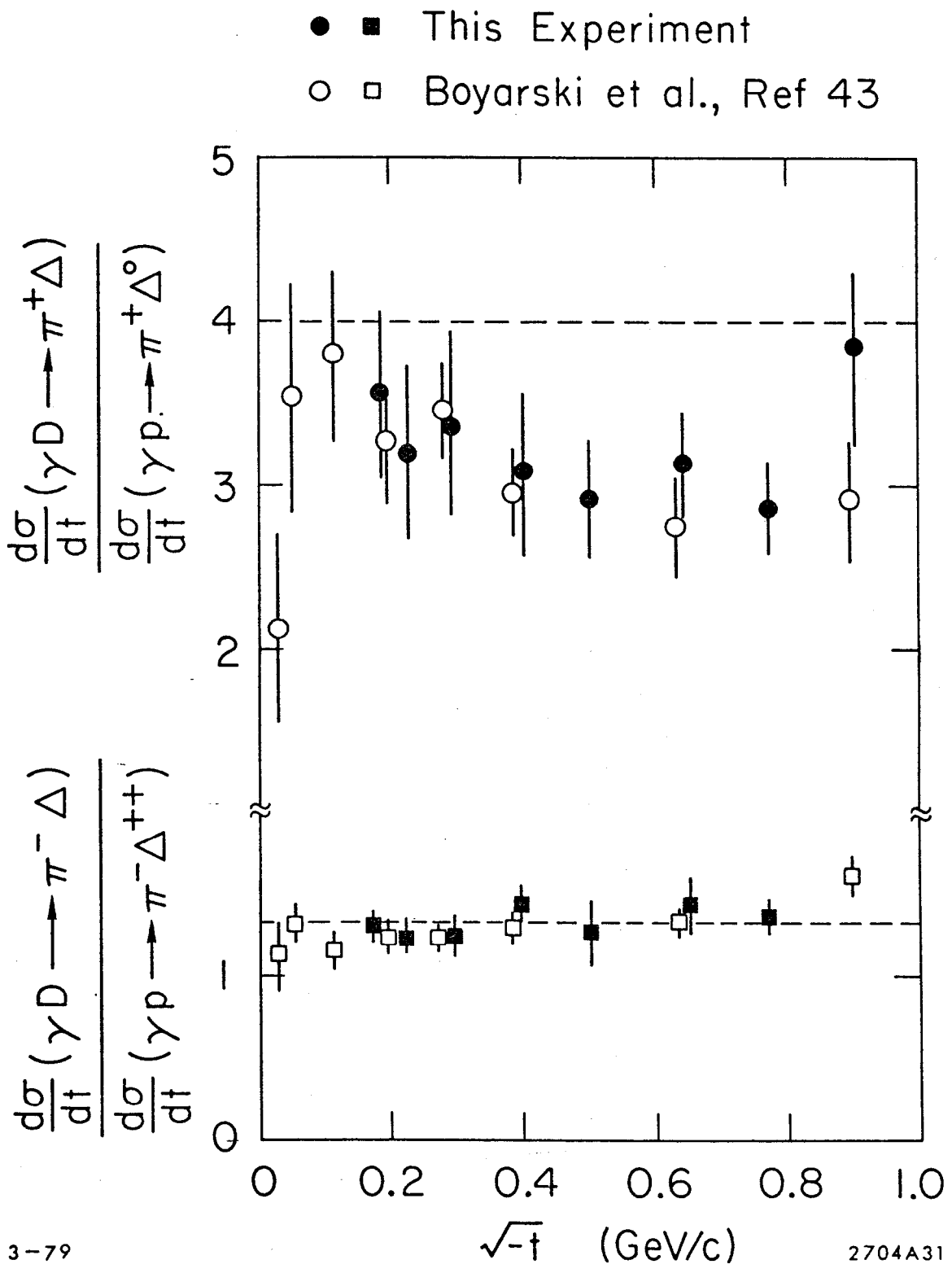
● ■ This Experiment
○ □ Boyarski et al., Ref 43
$\frac{d\sigma}{dt}(\gamma D \to \pi^+ \Delta) \Big/ \frac{d\sigma}{dt}(\gamma p \to \pi^+ \Delta^0)$
$\frac{d\sigma}{dt}(\gamma D \to \pi^- \Delta) \Big/ \frac{d\sigma}{dt}(\gamma p \to \pi^- \Delta^{++})$
5
4
3
2
1
0
0
0.2
0.4
0.6
0.8
1.0
$\sqrt{-t}$ (GeV/c)
3-79
2704A31

Fig. 23

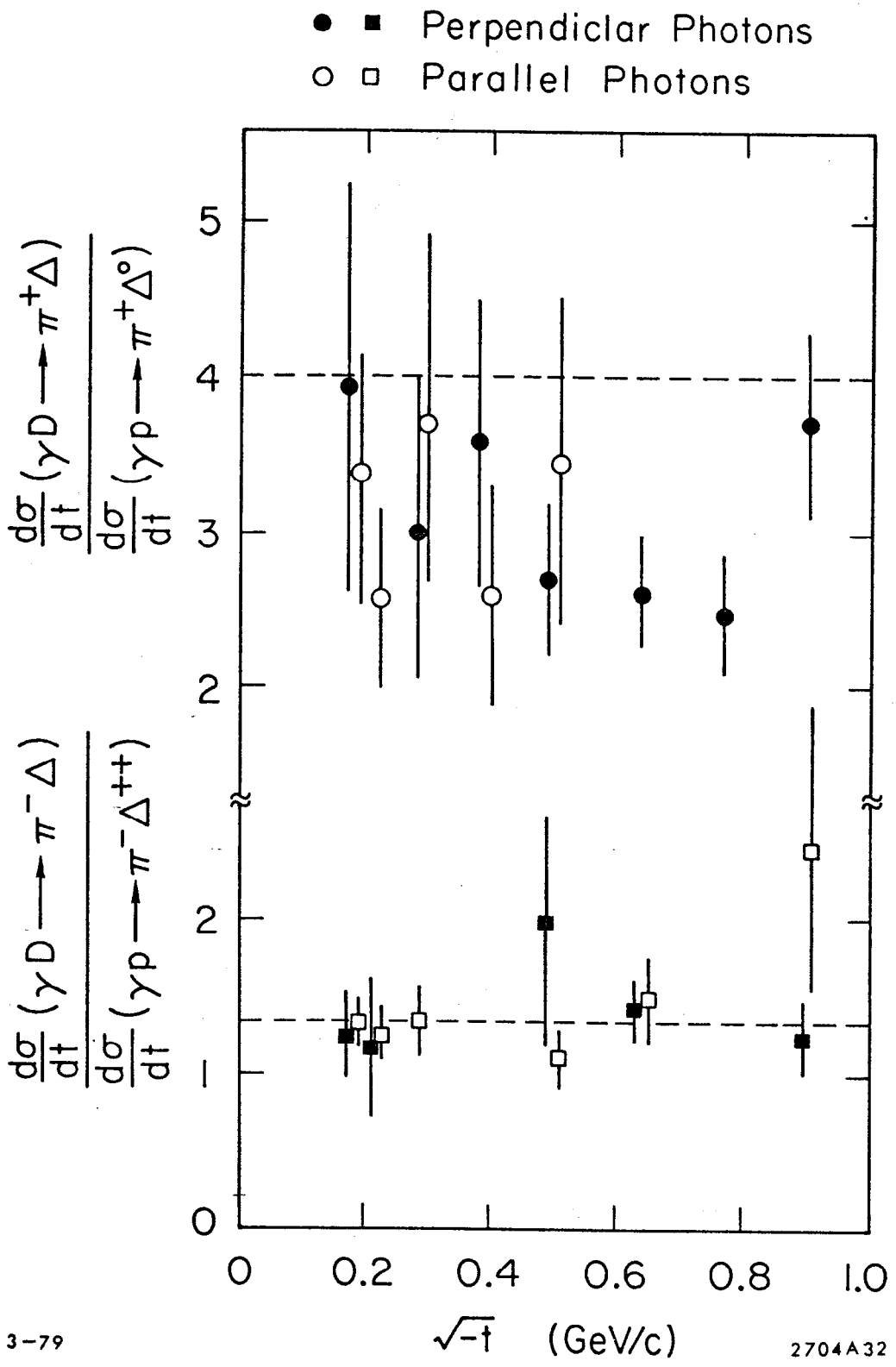
● ■ Perpendiclar Photons
○ □ Parallel Photons
$\frac{d\sigma}{dt}(\gamma D \rightarrow \pi^+\Delta) / \frac{d\sigma}{dt}(\gamma p \rightarrow \pi^+\Delta^0)$
$\frac{d\sigma}{dt}(\gamma D \rightarrow \pi^-\Delta) / \frac{d\sigma}{dt}(\gamma p \rightarrow \pi^-\Delta^{++})$
0
1
2
2
3
4
5
0
0.2
0.4
0.6
0.8
1.0
$\sqrt{-t}$ (GeV/c)
3-79
2704A32

Fig. 24

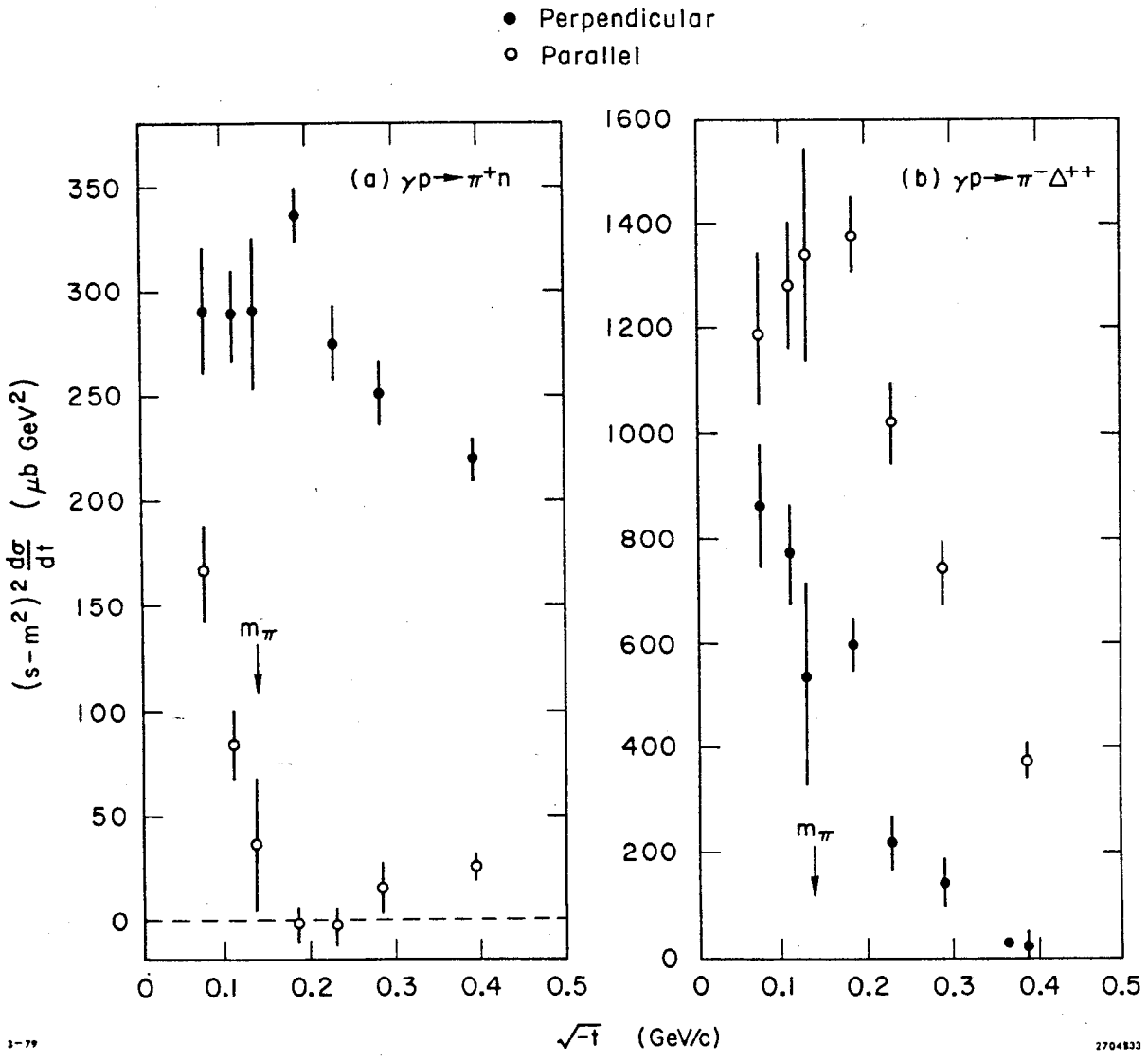
Perpendicular
Parallel
(a) γp→π+n
(b) γp→π−Δ++
$(s-m^2)^2 \frac{d\sigma}{dt}$ (μb GeV²)
$\sqrt{-t}$ (GeV/c)
m_π
m_π
0
50
100
150
200
250
300
350
0
200
400
600
800
1000
1200
1400
1600
0
0.1
0.2
0.3
0.4
0.5
3-79
2704833

Fig. 25

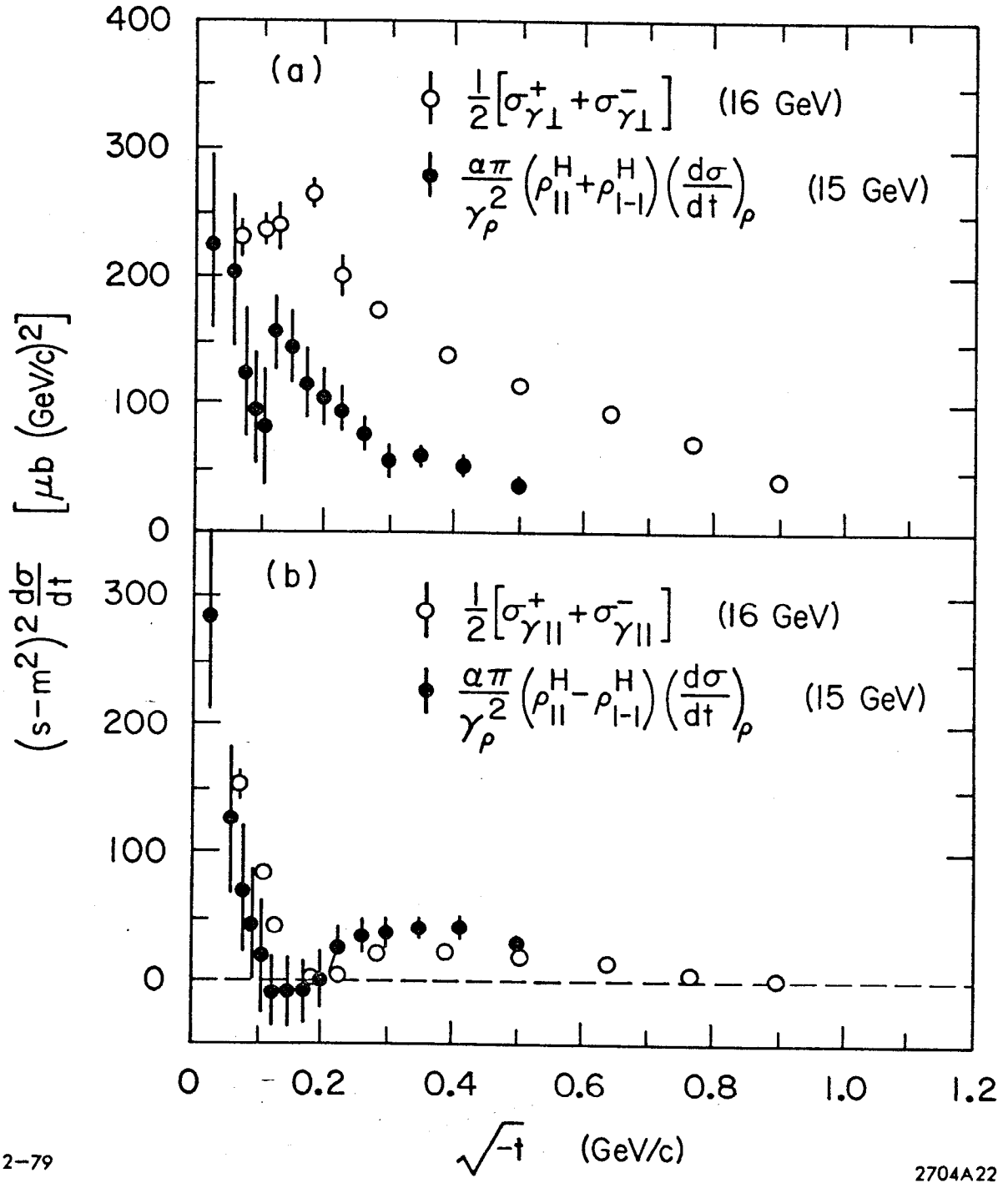
400
300
200
100
0
(a)
$\frac{1}{2}[\sigma^{+}_{\gamma\perp}+\sigma^{-}_{\gamma\perp}]$ (16 GeV)
$\frac{\alpha\pi}{\gamma_\rho^2}\left(\rho^H_{11}+\rho^H_{1-1}\right)\left(\frac{d\sigma}{dt}\right)_\rho$ (15 GeV)
$(s-m^2)^2\frac{d\sigma}{dt}$ [μb (GeV/c)^2]
300
200
100
0
(b)
$\frac{1}{2}[\sigma^{+}_{\gamma 11}+\sigma^{-}_{\gamma 11}]$ (16 GeV)
$\frac{\alpha\pi}{\gamma_\rho^2}\left(\rho^H_{11}-\rho^H_{1-1}\right)\left(\frac{d\sigma}{dt}\right)_\rho$ (15 GeV)
0
0.2
0.4
0.6
0.8
1.0
1.2
$\sqrt{-t}$ (GeV/c)
2-79
2704A22

Fig. 26

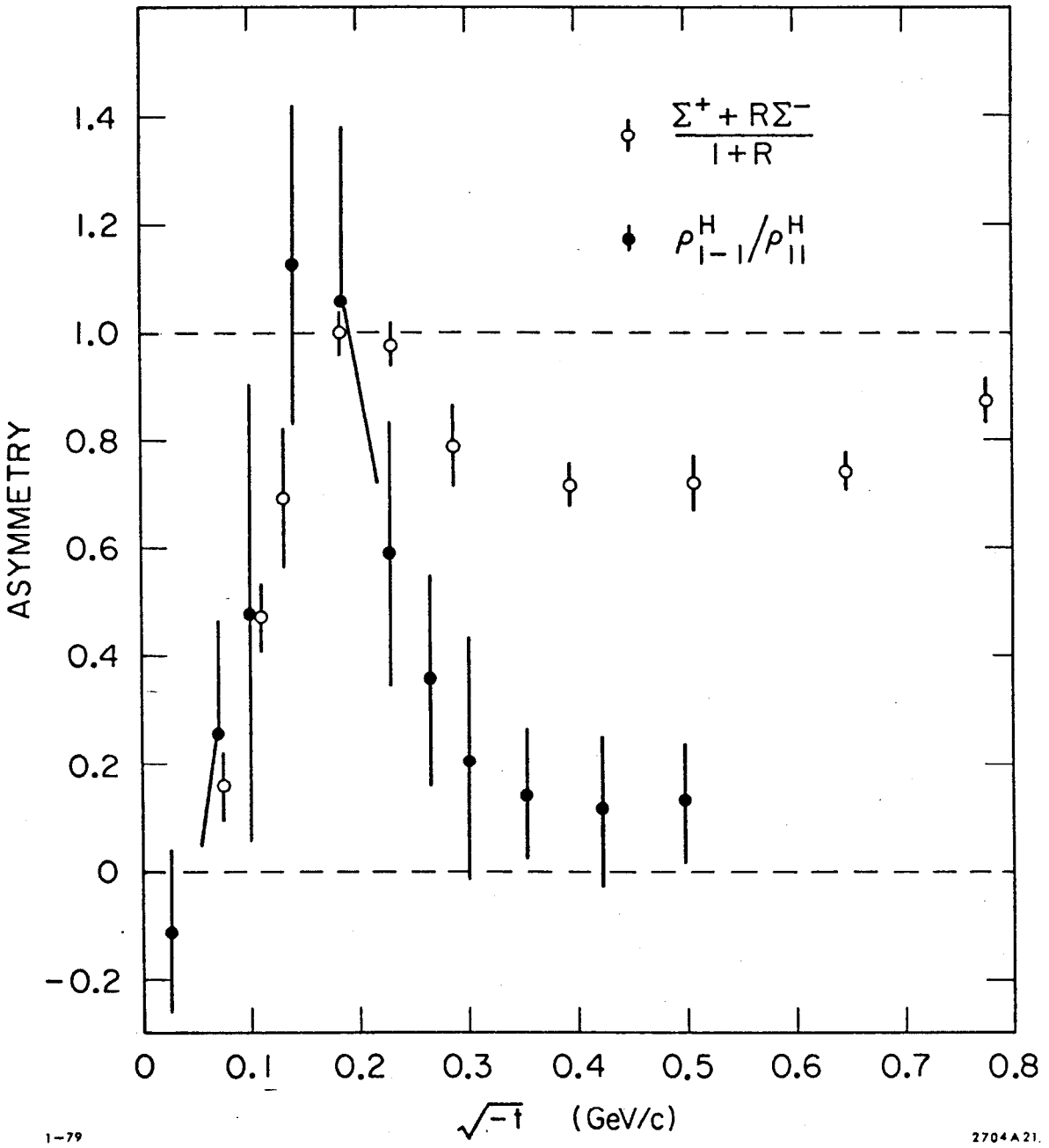
ASYMMETRY
1.4
1.2
1.0
0.8
0.6
0.4
0.2
0
-0.2
0
0.1
0.2
0.3
0.4
0.5
0.6
0.7
0.8
$\frac{\Sigma^+ + R\Sigma^-}{1+R}$
ρ^H_{1-1}/ρ^H_{11}
$\sqrt{-t}$ (GeV/c)
1-79
2704A21.

Fig. 27

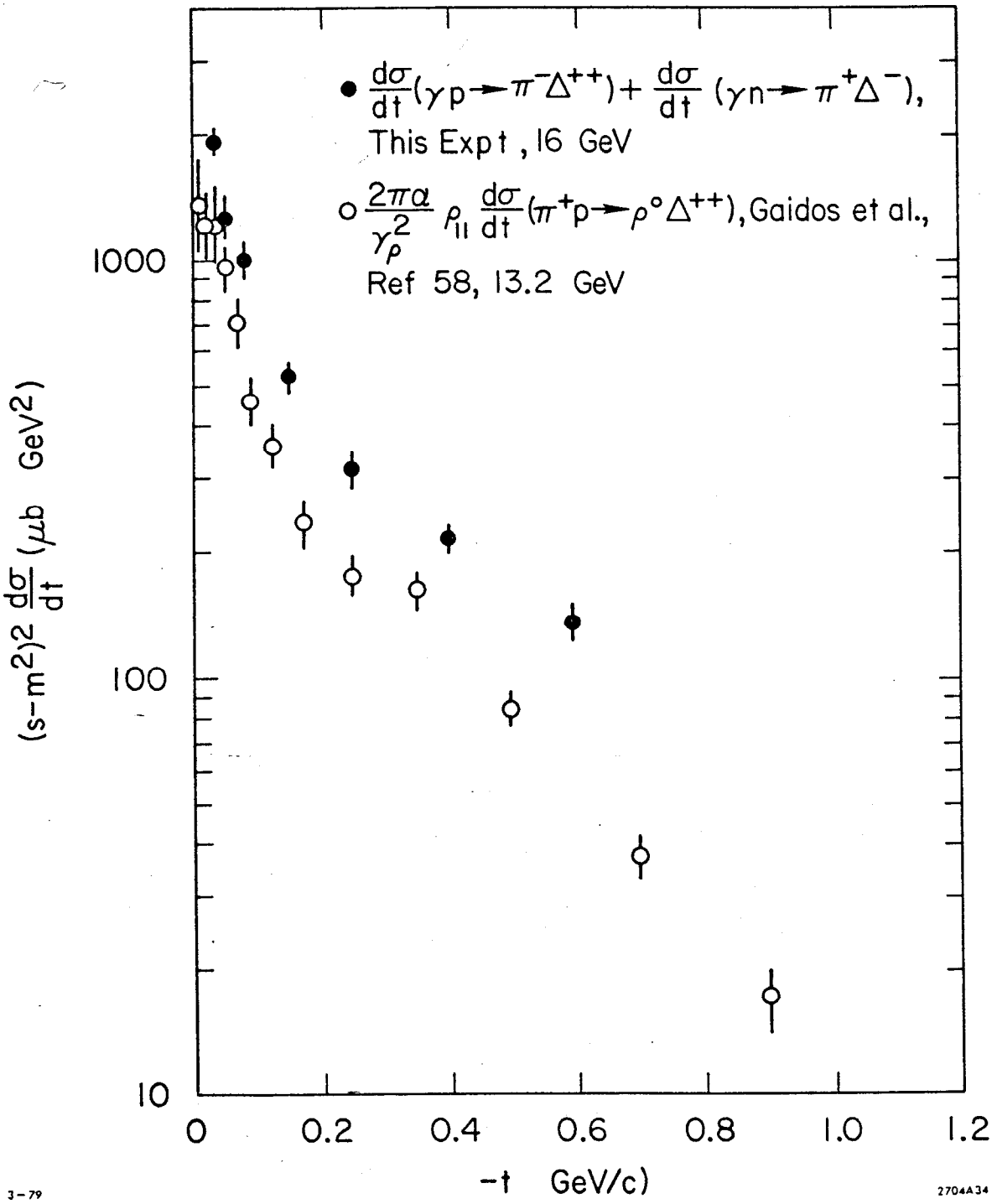
● $\frac{d\sigma}{dt}(\gamma p \to \pi^- \Delta^{++}) + \frac{d\sigma}{dt}(\gamma n \to \pi^+ \Delta^-)$, This Expt, 16 GeV
○ $\frac{2\pi\alpha}{\gamma_\rho^2} \rho_{11} \frac{d\sigma}{dt}(\pi^+ p \to \rho^\circ \Delta^{++})$, Gaidos et al., Ref 58, 13.2 GeV
$(s-m^2)2 \frac{d\sigma}{dt}$ (μb GeV2)
1000
100
10
0
0.2
0.4
0.6
0.8
1.0
1.2
-t GeV/c)
3-79
2704A34

Fig. 28

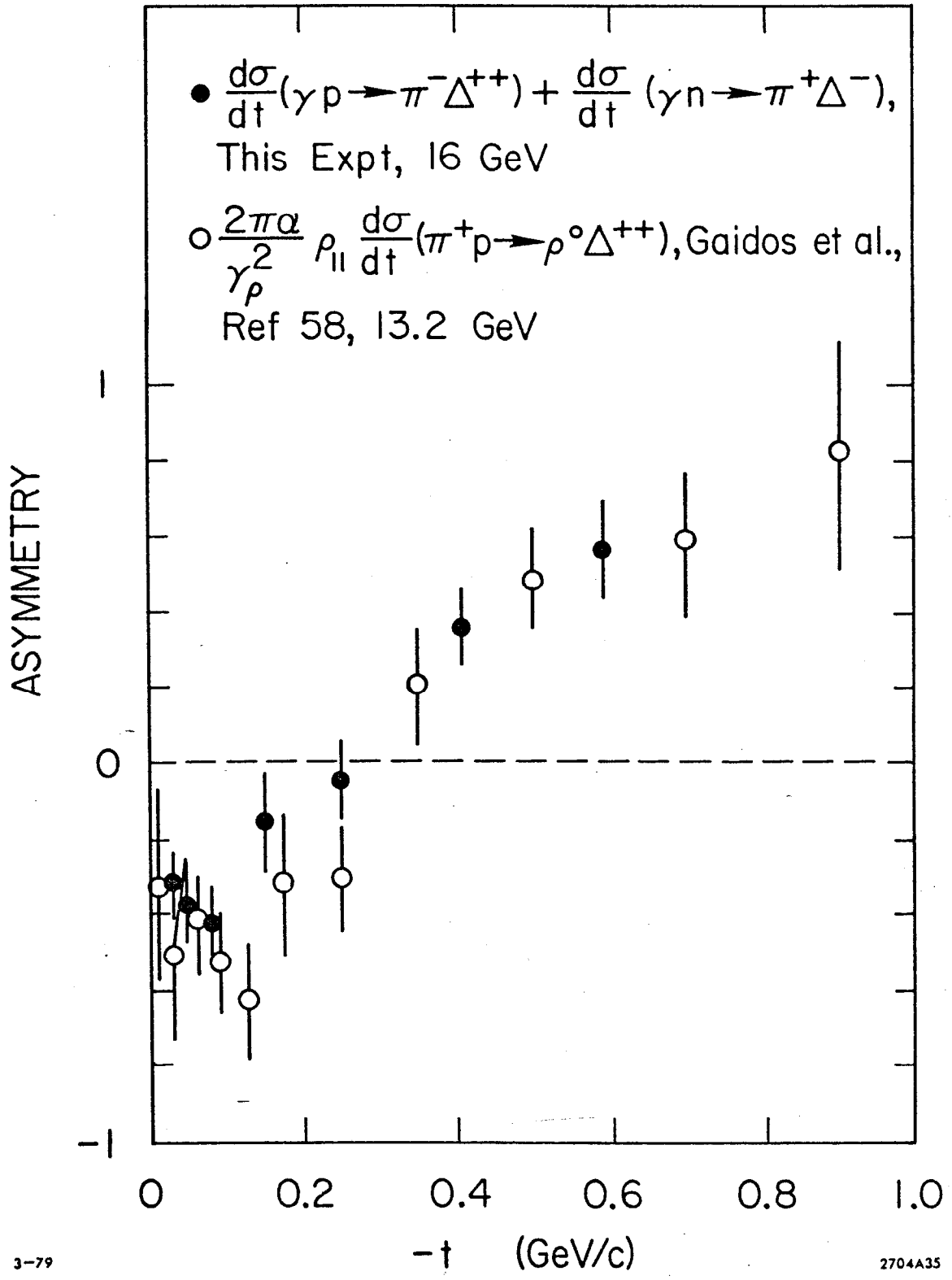
● $\frac{d\sigma}{dt}(\gamma p \to \pi^- \Delta^{++}) + \frac{d\sigma}{dt}(\gamma n \to \pi^+ \Delta^-)$,
This Expt, 16 GeV
○ $\frac{2\pi\alpha}{\gamma_\rho^2} \rho_{11} \frac{d\sigma}{dt}(\pi^+ p \to \rho^0 \Delta^{++})$, Gaidos et al.,
Ref 58, 13.2 GeV
ASYMMETRY
1
0
-1
0
0.2
0.4
0.6
0.8
1.0
-t (GeV/c)
3-79
2704A35

Fig. 29

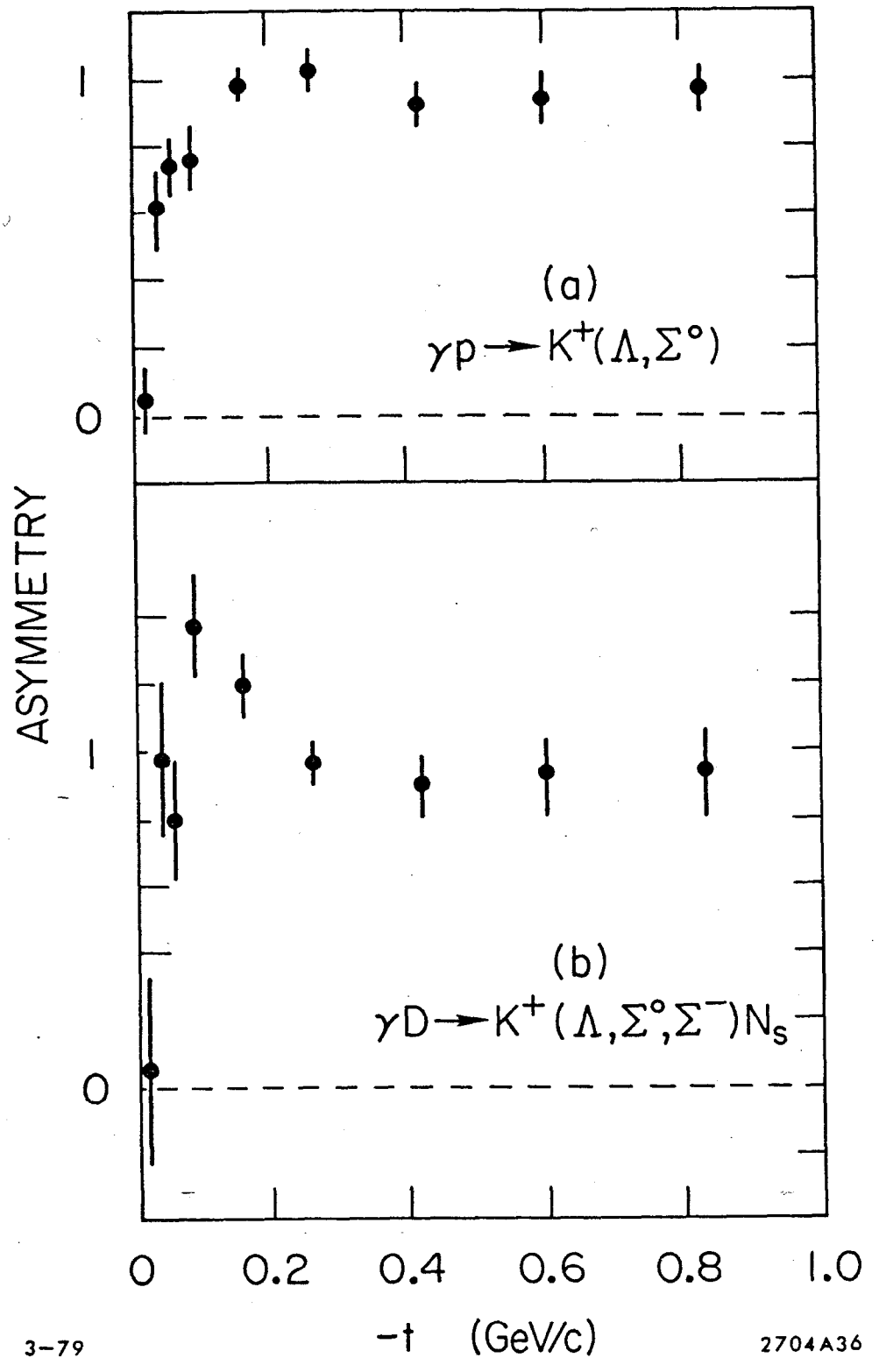
1
0
(a)
γp → K+(Λ,Σ°)
ASYMMETRY
1
0
(b)
γD → K+(Λ,Σ°,Σ⁻)Ns
0
0.2
0.4
0.6
0.8
1.0
-t (GeV/c)
3-79
2704A36

Fig. 30

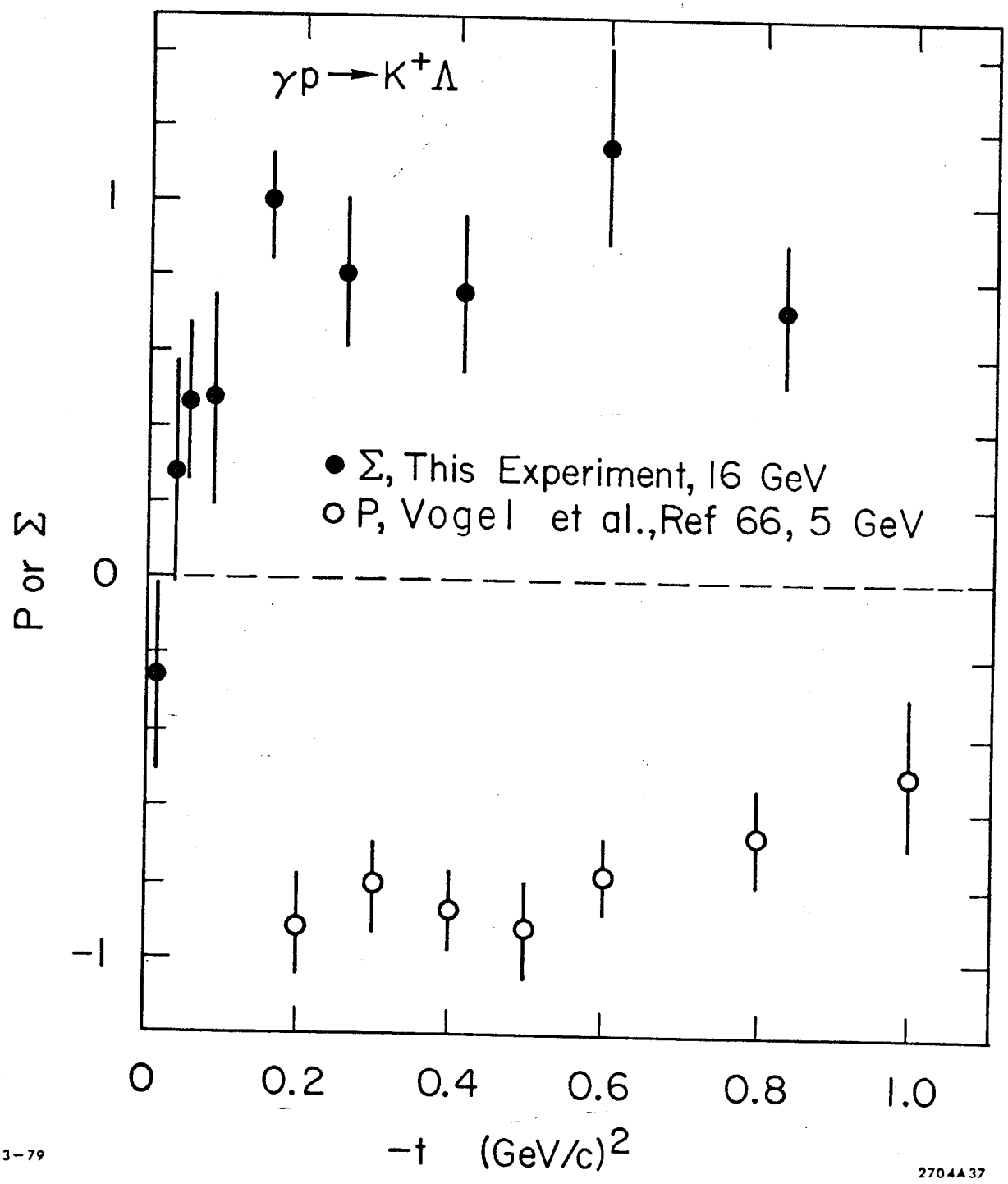
γp → K⁺Λ
● Σ, This Experiment, 16 GeV
○ P, Vogel et al., Ref 66, 5 GeV
P or Σ
1
0
-1
0
0.2
0.4
0.6
0.8
1.0
-t (GeV/c)²
3-79
2704A37

Fig. 31

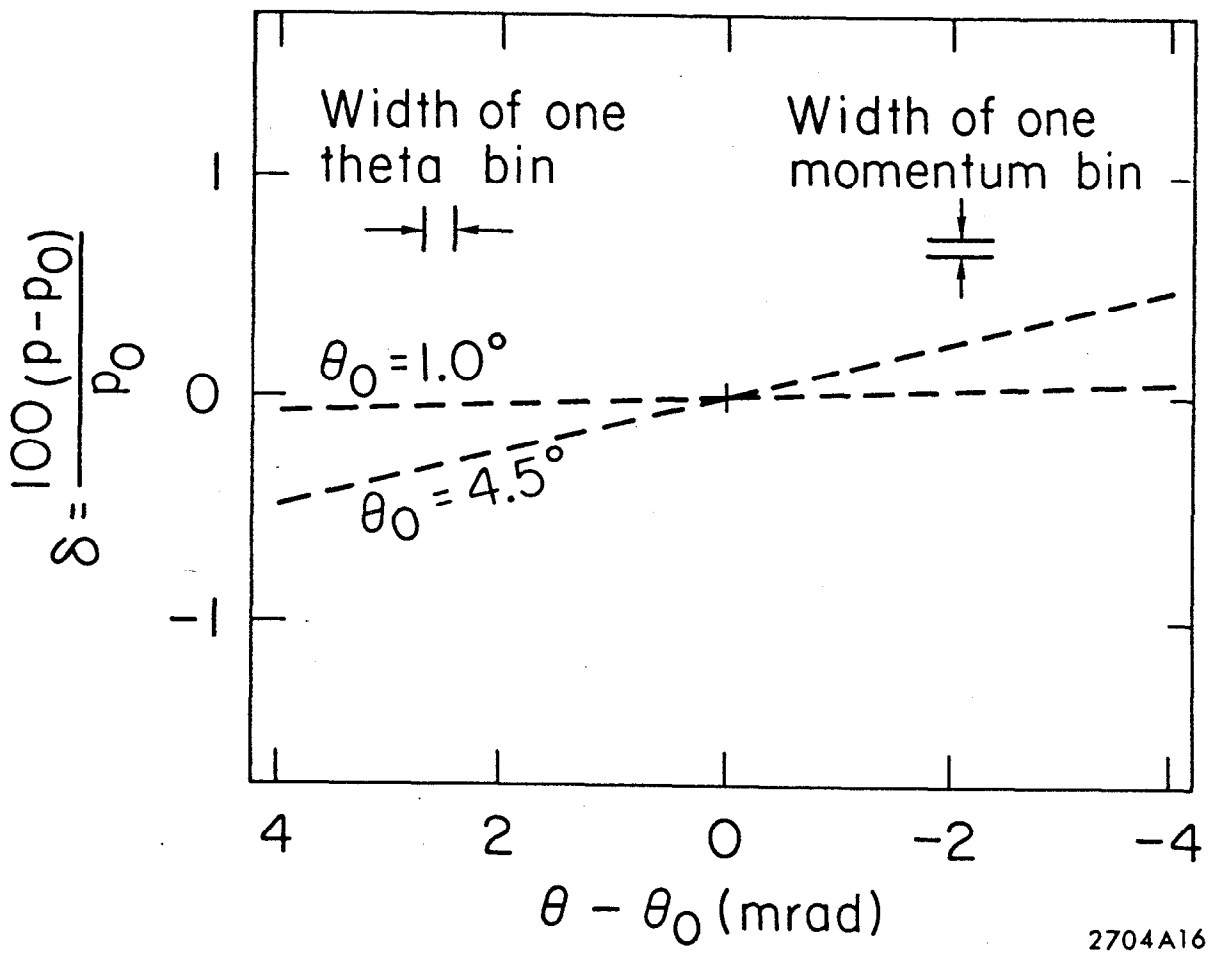
Width of one theta bin
Width of one momentum bin
$\theta_0 = 1.0°$
$\theta_0 = 4.5°$
$\delta = \frac{100(p-p_0)}{p_0}$
1
0
-1
4
2
0
-2
-4
$\theta - \theta_0$ (mrad)
2704A16

Fig. 32

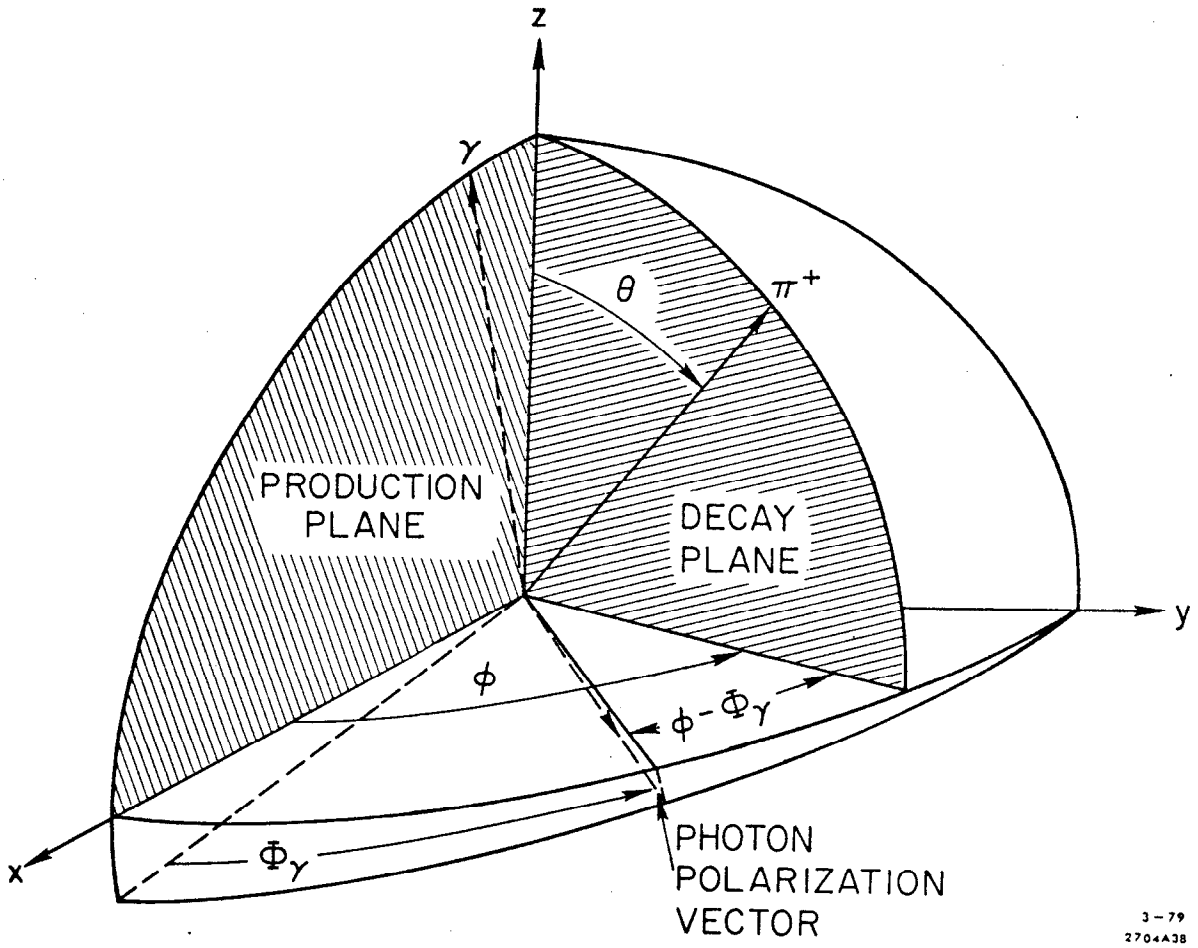
z
γ
θ
π+
PRODUCTION
PLANE
DECAY
PLANE
y
ϕ
ϕ-Φγ
x
Φγ
PHOTON
POLARIZATION
VECTOR
3-79
2704A38

Fig. 33

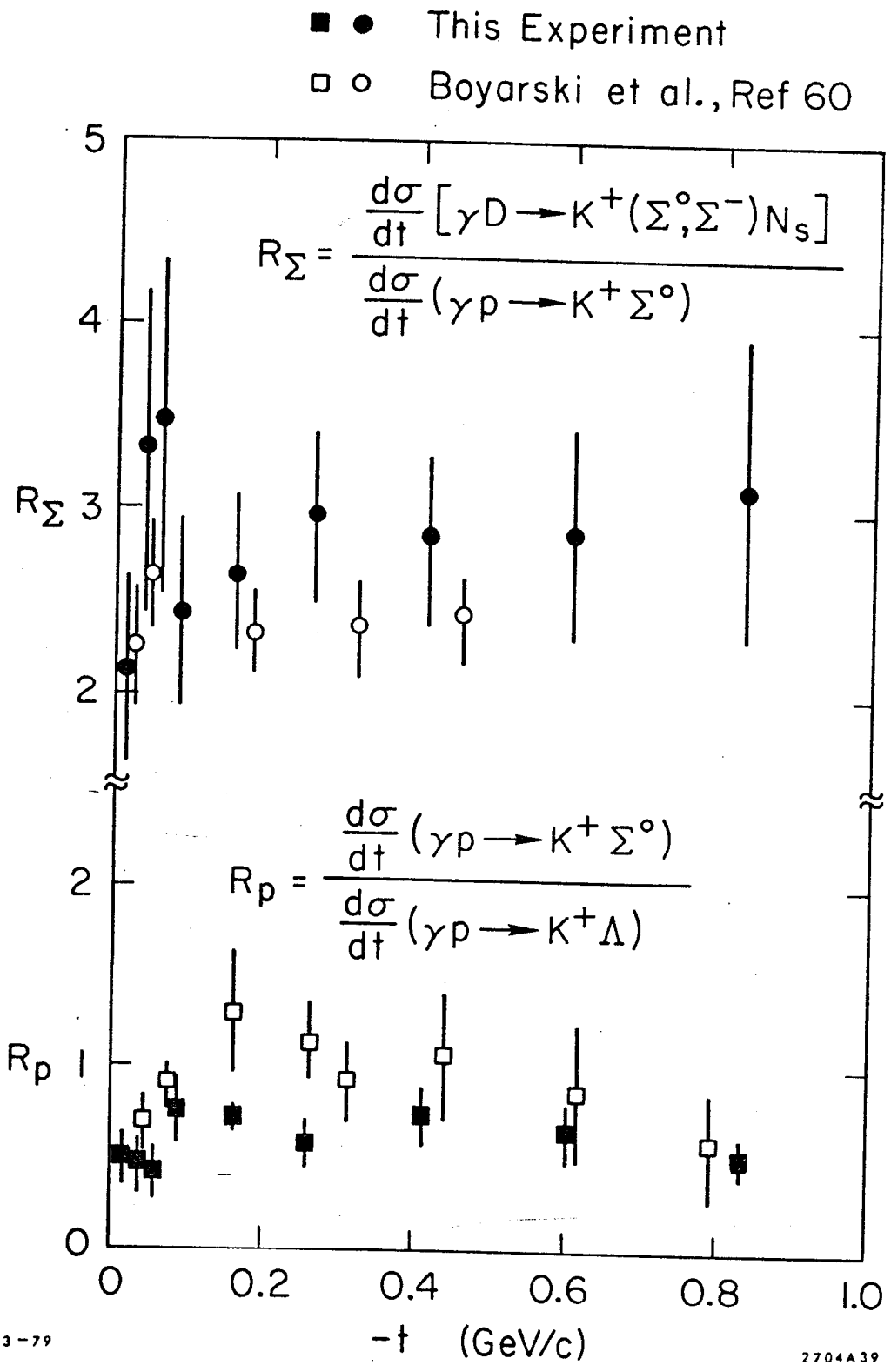
This Experiment
Boyarski et al., Ref 60
$R_\Sigma = \frac{\frac{d\sigma}{dt}[\gamma D \to K^+(\Sigma^\circ,\Sigma^-)N_s]}{\frac{d\sigma}{dt}(\gamma p \to K^+\Sigma^\circ)}$
$R_p = \frac{\frac{d\sigma}{dt}(\gamma p \to K^+\Sigma^\circ)}{\frac{d\sigma}{dt}(\gamma p \to K^+\Lambda)}$
R_Σ
R_p
0
1
2
3
4
5
0
0.2
0.4
0.6
0.8
1.0
$-t$ (GeV/c)
3-79
2704A39

Fig. 34